1-1-2022

Core Size Conversion and Ligand Effects on Gold Nanomolecules Structure and Properties.

Senthilkumar Eswaramoorthy

CORE SIZE CONVERSION AND LIGAND EFFECTS ON GOLD NANOMOLECULES STRUCTURE AND PROPERTIES

A Dissertation
presented in the partial fulfillment of Doctor of Philosophy
in the Department of Chemistry & Biochemistry
The University of Mississippi

by

SENTHIL KUMAR ESWARAMOORTHY

May 2022

ABSTRACT

The size, shape and structure of the materials determines its properties in any scale. When the size of the material reaches nanometer scale, it shows a strikingly different property from the bulk. Monodisperse metal nanoparticles are highly desired due to its unique properties which can be explored for targeted applications. The nanoparticles with size less than 3 nm, atomically precise metal nanoparticles can be achieved, whereas nanoparticles in 3-100 nm range are monodisperse in size but not atomically monodisperse. Thiolate protected gold nanoparticles size less than 3 nm forms highly stable atomically precise compounds with distinct number of gold atoms and thiolate ligands, represented by $Au_n(SR)_m$, which are referred as gold nanomolecules (Au NMs). Au NMs have unique physical and chemical properties which are dependent on "n" and "m". The overall composition and resulting properties of Au NMs are dictated by the type of capping ligand. Currently based on the type of capping ligand, Au NMs are classified into three main categories, aliphatic, aromatic, and bulky thiolate Au NMs. These distinct categories form unique series of Au NMs represented as aliphatic, aromatic, and bulky Au NMs series. However, recent discoveries on various aromatic thiol protected Au NMs reveals that these Au NMs deviate from aromatic series when size become large. Meanwhile, core size conversion brought a unique synthesis route of inter-converting between these three series with comparable sizes. This dissertation focuses on studying the ligand effects on Au NM using core size conversion on new Au NMs with previously studied thiols and previously studied Au NMs with new thiols,

and by closely comparing the structures with same structural arrangements.

Chapter 2 of this dissertation focuses on the first core size conversion of plasmonic Au NMs and its reaction pathway using MALDI-MS, ESI-MS, and UV-visible spectroscopy.

Chapter 3 of this dissertation details the process in which digestive ripening synthesis method yields atomically precise Au NMs. In this work, the unique series achieved using Brust synthesis method is also achieved through digestive ripening method which was confirmed using MALDI-MS, ESI-MS, and UV-visible spectroscopy.

Chapter 4 of this dissertation introduces the crystallographic structure determination of *p*-methyl benzene thiolated $Au_{36}(PMBT)_{24}$ nanomolecule and details the ligand effects on $Au_{36}(SR)_{24}$ structure using all four reported crystal structures.

In Chapter 5, we took a turn and explored a different metal, Palladium. In this chapter, the dissertation focuses on discovery and synthetic protocol development of atomically precise palladium nanoclusters using phenyl ethane thiol.

Chapter 6 of this dissertation explains the vital nature of size exclusion chromatography (SEC) in our works and focuses on the effect of column length in SEC using tert-Butyl thiol protected Au NMs.

Chapter 7 of this dissertation details original research proposal and investigation into the ligand effect by employing core size conversion of $Au_{144}(SR)_{60}$ with three aromatic thiols, where the para position is substituted with methyl, ethyl, and iso-propyl groups respectively.

To the two incredible women in my life

My mom, who puts my needs before hers since the day I was born

&

my wife for her care, support, and love

LIST OF ABBREVIATIONS AND SYMBOLS

Au	gold
THF	tetrahydrofuran
BHT	butylated hydroxytoluene
DCM	dichloromethane
DCTB	trans-2-[3[(4-*t*ertbutyl-phenyl)-2-methyl-2-propenylidene] malononitrile
DFT	density functional theory
$HAuCl_4 \bullet 3H_2O$	chloroauric acid
HOMO	highest-occupied molecular orbital
LUMO	lowest unoccupied molecular orbital
MALDI	matrix assisted laser desorption
ESI	Electrospray Ionization
MS	mass spectrometry
$NaBH_4$	sodium borohydride
nm	nanometer
NM	nanomolecule
Pd	palladium
Pt	platinum
SAMs	self-assembled monolayers

SCH_2CH_2Ph	phenylethanethiol
SEC	size exclusion chromatography
SPh	thiophenol
PMBT	*para*-methylbutanethiol
TBBT	4-*tert*-butylbenzenethiol
SPh-*i*Pr	*iso*propylbenzenethiol
SPh-Et	ethylbenzenethiol
SPh-*t*Bu	4-*tert*-butylbenzenethiol
S-*t*Bu	*tert*-butylthiol
PC2	phenylethanethiol
ToABr	tetraoctylammonium bromide
TOF	time of flight
UV-visible	ultraviolet-visible
ScXRD	single crystal x-ray diffraction

ACKNOWLEDGMENTS

First and foremost, I express my deepest gratitude to my advisor, Dr. Amala Dass for being a thoughtful and supportive mentor. Thank you for providing a good environment for me to learn and helping me to grow as both a scientist and a person.

Next, thank you to my committee members: Dr. Saumen Chakraborty, Dr. Susan Pedigo, Dr. Daniel Mattern, and Dr. David Colby for their advice, support, and encouragement.

I could not have financed my doctoral studies without the assistantship provided by the University of Mississippi, Department of Chemistry & Biochemistry, and the Graduate School and thank them for their financial support. I am also grateful to National Science Foundation for funding our research, also Prof. Charles Hussey, Prof. Greg Tschumper and The College of Liberal Arts for providing instrumentation support.

Thank you to my fellow doctoral students: Dr. Milan Rambukella, Dr. Naga Arjun Sakthivel, Dr. Tanya Jones, Vignesh Raja Ganeshraj, and Kalpani Hirunika Wijesinghe; for their support, guidance, and help throughout my time in Ole Miss.

Thank you to my parents: Eswaramoorthy and Suseela, for everything they did for me which made my life, education, and me as a person possible. Thanks to my mom for her unconditional love and support despite all the difficult circumstances in my life, and my dad for all his valuable advice.

Thank you to my lovely wife Dhanashree. Since the day we met, you have been

brightest light in my life. You make me want to be a better person every single day. Thank you for your love, your support and being there for me every day.

Thank you to all my teachers from school, for their support, mentoring and inspired me into pursuing science in my life.

Thank you to all my professors, and friends from CECRI, Karaikudi during my undergraduate days. Also, the CECRI campus in Karaikudi, India for introducing research into my life and inspiring me towards pursuing PhD.

Special thanks to all the former and present leaders in India, especially leaders from the state of Tamil Nadu for making education possible to a person like me through their policies and vision. Special thanks to Canara Bank and the branch manager for providing me education loan at crucial moment during admission to my undergraduate course.

TABLE OF CONTENTS

LIST OF SCHEMES AND TABLES

SCHEME PAGE

TABLE PAGE

LIST OF FIGURES

FIGURE PAGE

CHAPTER 1

INTRODUCTION

1.1 Gold Nanoparticles

A nanoparticle is defined as a "*nano-object with all three external dimensions in the nanoscale, whose longest and shortest axes do not differ significantly, with a significant difference typically being a factor of at least 3.*" Nanoscale refers to scale between 1 to 100 nm.[1] The science and study of matter at the nanoscale that deals with understanding their size and structure-dependent properties is called Nanoscience. Nanotechnology is the fabrication of these materials for enhanced properties. Gold, a precious metal is considered as one of the most noble metals due to its inert nature. Its atomic number is 79 and the atomic mass is 196.96 amu. The electronic configuration of gold is:

$$Au = [Xe]\ 4f^{14}\ 5d^{10}\ 6s^{1}$$

Metallic gold does not react with most of the chemicals and atmospheric oxygen contributing to its inert nature. It can have six oxidation states from -1 to +5, however +1 and +3 charge states are the common ones. Gold was recognized as a sign of wealth and power from early civilization until last century. Any currency by a country's central bank should be backed by gold, which is called the gold standard, until June 5, 1933, when the United States went off the gold standard. In modern world, gold is used in various advanced

techniques due to its unique physical and chemical properties. The nanosized metal particles attract huge interest in catalysis, optics and drug delivery because of its remarkable difference in physical and chemical properties from their respective bulk metals.[2] The usage of gold nanoparticles leads back to 4th Century AD. The Lycurgus cup with unusual optical

Figure 1.1. Lycurgus cup from 4th century A.D. The glass is stained with gold nanoparticles. (Source: http://www.britishmuseum.org).

effects shown in Figure 1.1 is an extraordinary example of roman cut glass which has colloids of different metal nanoparticles.[3] The Lycurgus cup displays a deep wine-red color in the transmitted light, while it exhibits an opaque pea-green color in reflected light. The Transmission Electron Microscopy (TEM) analysis of the cup showed the presence of gold/silver alloy nanoparticle of about 7-10 nm size. The dichroic effect of the cup is due to these alloy metal nanoparticles as suggested by Brill, the gold nanoparticles are responsible for the red transmission and the silver for green reflection.[3-5] Prime examples of ancient colloids are further seen in the stained glass windows in the cathedral of Notre Dame and in the paint of ceramics from the Italian renaissance.[5] In the 18th century, gold colloids were first recognized by Michael Faraday and Thomas Graham.[5] Many colloid gold nanoparticles

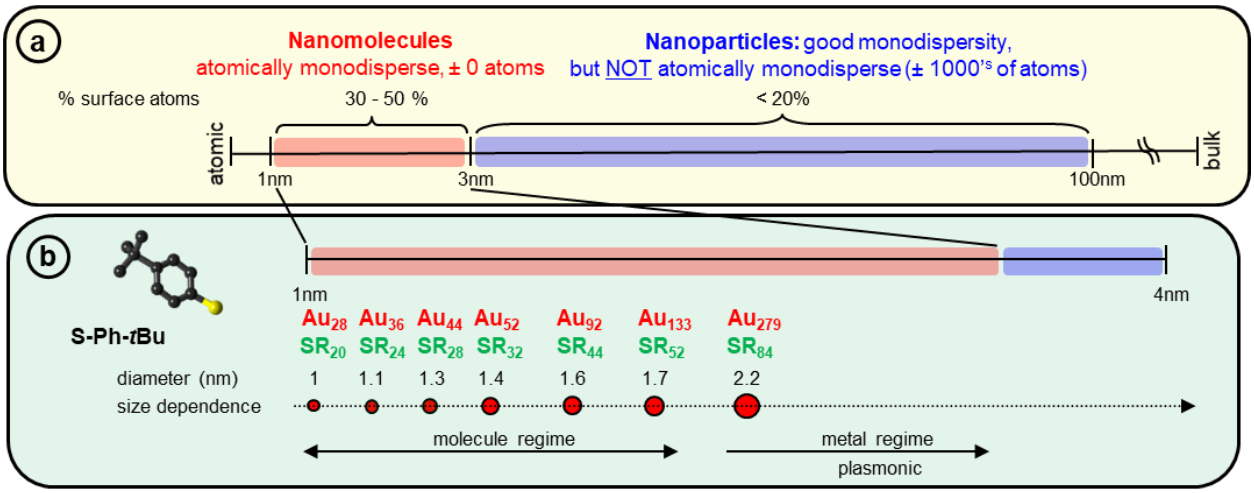

Figure 1.2. Thiolate protected series of Au NMs reported to date in two systems. (a) 1-100 nm size range with 1-3 nm containing nanomolecules (±0 atoms) and 3-100 nm containing nanoparticles where size dispersity has been achieved but still variation of ±1000 atoms exist. (b) TBBT series

are not stable and usually decompose, therefore research since then and up to now has looked at focusing down the size of the colloids into nanoparticles and improving their stability, in order to harness and understand their unique properties. Research to date has been able to create gold nanoparticles which range from 1-100nm.[6] Currently, Gold Nanoparticles (Au NPs) are used in wide range of fields like optics, nanomedicine, catalysis, solar cells, and imaging.

1.1 Gold Nanomolecules

Monodisperse nanoparticles are required to study its physical and chemical characteristics. Typically, size distribution of Au NPs above 3 nm were characterized using transmission electron microscopy (TEM). However, in atomic scale one nanometer (nm) difference provides a difference of hundreds of atoms. Therefore, the size monodispersity is very different from atomic monodispersity. Thiolate protected Au NPs, whose size is less than 3 nm, provide atomically precise (± 0 atoms) Au NPs with distinct number of gold atoms

and thiolated ligands (Figure 1.2). This special class of atomically precise Au NPs, with molecular formulas [$Au_n(SR)_m$] is called gold nanomolecules (Au NMs). Pioneering work by Brust et al. in two phase synthesis of thiolate derivatized gold nanoparticles, initiated the intense interest in thiolate protected Au NPs.[7] The major development reported by Whetten with the help of mass spectrometry proved that atomically precise compounds which termed as molecular like gold nanocrystals, can be isolated and studied.[8-9] A breakthrough report by Jadinsky et al. through determination of the total structure of $Au_{102}(S\text{-}C_6H_4\text{-}COOH)_{44}$ using single crystal X-ray Diffraction (ScXRD)[10] and highly studied $Au_{25}(SCH_2CH_2Ph)_{18}$ structure determination by Murray group,[11] provided clarity and insight into the intricate structural arrangement of metal-ligand self-assembly interface. This atomic level revelation brought a high tide into the field by subsequent report of several crystal structures by various types of thiolated ligands revealing several new kernels.

Extensive research on thiolate protected Au NMs by various groups resulted in wide range of Au NMs protected by different thiols.[12-16] These results reveal that ligand steric and electronics dictate the core structure and composition of the resulting Au NMs. Therefore, each ligand forms a unique series of Au NMs with discrete number of Au atoms and thiolate ligands. For instance, an alkane thiolate protected Au NMs series comprises of $Au_{25}(SR)_{18}$, $Au_{38}(SR)_{24}$, $Au_{67}(SR)_{35}$, $Au_{137}(SR)_{46}$, $Au_{144}(SR)_{60}$, $Au_{329}(SR)_{84}$, $Au_{\sim500}(SR)_{\sim120}$, and $Au_{\sim940\pm20}(SR)_{\sim160\pm4}$.[15, 17-19] Au NMs have several interesting properties such as their stability, dispersion in solution, ability to remain stable in a dried powder state for years, and unique optical properties which are highly applicable in catalysis, sensors, and medicine.[12, 20-30]

1.2 Experimental approach

1.2.1 Synthesis. The two-phase Brust-Schiffrin method that utilizes water and organic (toluene) solvents, is the most commonly used method for the synthesis of thiolate protected Au NMs.[7] The composition of NM, and core size can be manipulated by tuning the gold to thiol ratio, different reducing agents, reaction conditions like temperature, time, stirring rate etc., type of solvent and importantly type of thiolated ligand.

Typically, gold salt (chloroauric acid, $HAuCl_4.3H_2O$) dissolved in distilled water and tetraoctylammonium bromide (ToABr) dissolved in toluene are mixed in a Round Bottom Flask (RBF) with stirring. Here, ToABr helps in phase transferring the gold salt to organic phase followed by removal of aqueous layer (1.1 and 1.2).

$$HAuCl_4(aq) \longrightarrow H^+(aq) + [AuCl_4]^-(aq) \quad (1.1)$$

$$[AuCl_4]^-(aq) + [N(C_8H_{17})4]^+(tol) \longrightarrow [N(C_8H_{17})_4]^+[AuCl_4]^-(tol) \quad (1.2)$$

Then a specified amount of thiol is added to the organic phase with continued stirring. In this step, Au^{3+} was reduced to Au^{1+} in the presence of thiol which then gradually forms $(Au(SR))_n$ polymer (1.3). This reaction is then reduced with sodium borohydride ($NaBH_4$) to form a black colored solution. Here, BH_4^- reduces Au^{1+} to Au^0 resulting in $Au_m(SR)_n$ crude nanoclusters with various size(1.4).

$$[AuCl_4]^-(tol) + 3[HSR]\,(tol) \longrightarrow (Au(SR))_n\,(tol) + RS\text{-}SR(tol) + 4Cl^-(aq) \quad (1.3)$$

$$(Au(SR))_n\,(tol) + RS\text{-}SR(tol) + BH_4^-(aq) \longrightarrow Au_x(SR)_y(tol) + B(OH)_3(aq) + H_2(g) \quad (1.4)$$

The resulting crude mixture is dried under reduced pressure and purified by washing with copious amounts of water and methanol. The crude mixture is then thermochemically etched with excess thiol to obtain thermodynamically stable nanomolecules.[31] The etched products is washed with methanol to remove excess thiols and byproducts. The etched

product are then extracted using suitable solvent such as: toluene, THF, ACN, and DCM. Typically, these Au NMs are dried and stored in refrigerator for long shelf life.

The two-phase Brust-Schiffrin method has also been modified to one-phase where polar solvents, such as tetrahydrofuran (THF) and methanol, are usually used for preparing Au NPs excluding the necessity of phase transfer agent ToABr.[32] In some cases, ToABr is used to narrow the size distribution of resulting product.[33]

1.2.2 Isolation and Purification: Thermochemically etched product contains two or more stable Au NMs. Therefore, further isolation steps are needed to separate those species. We majorly use two techniques: solvent fractionation and size exclusion chromatography.

1.2.2.1 Solvent fractionation: The difference in solubility of Au NMs is used in solvent fractionation to isolate Au NMs. Solubility of the Au NMs differ because of various factors. One of the main factors is size. Smaller size Au NMs is polar in nature and therefore soluble in polar solvents like acetonitrile and acetone. As the size increases, the nature changes to non-polar and is soluble in less polar solvents like toluene, dichloromethane (DCM), and THF. For example, Au_{23}(S-*t*Bu)$_{16}$ and $Au_{25}(SCH_2CH_2Ph)_{18}$ are soluble in acetonitrile while other nanomolecules such as Au_{30}(S-*t*Bu)$_{18}$ and $Au_{144}(SCH_2CH_2Ph)_{60}$, which are generally synthesized in conjunction respectively, are not soluble in acetonitrile. In solvent fractionation, a polydisperse product was dissolved in an organic solvent such as toluene, DCM, or THF. To this solution, a non-solvent like methanol is added in incremental amounts. As the polarity of the solution was gradually increased with addition of non-solvent like methanol or acetonitrile, the larger sizes precipitate first followed by smaller ones. An optimum concentration of the polydisperse mixture was used to achieve better separation. A highly concentrated solution would lead to poor separation, whereas dilute solutions

would require large volumes of acetonitrile or methanol. Typically, 100 mg of a polydisperse product was dissolved in 0.2-1 mL of the solvent. The non-solvent was then gradually added using a micro-pipette in small quantities (typically in multiples of 100 μL). Once the precipitate was observed, the vial was centrifuged to separate the precipitate (insoluble portion) from the supernatant (soluble portion). The fractions were then analyzed by MS to determine their composition.

1.2.2.2 Size Exclusion Chromatography (SEC): SEC is another most used method for separation of Au NMs. SEC separates the particles based on the hydrodynamic volume. The mixture of various sizes particles in mobile phase is eluted through a stationary bed consisting of SEC beads, where smaller-sized compounds travel through the pores in the beads and take a longer path to elute and larger sizes take a shorter path and elute faster through the larger pores or spaces between the beads. For our compounds, we use glass column with fritted disc filled with Bio-beads S-X1 as the stationary phase, and THF stabilized with BHT as the mobile phase. The Bio-Beads are made of neutral, porous styrene divinylbenzene copolymers. It needs to be soaked in mobile phase.[34-35] In a typical SEC preparation, about 100 g of the solid beads were soaked in ~0.5 L THF-BHT in a 1 L beaker topped with a lid to prevent solvent evaporation. The beads were soaked for at least 6 hours, preferably overnight. The beads expand in volume during this time. After sufficient soaking, the slurry of swollen beads was then packed in the column. The slurry was slowly loaded through the top side of the column with the stopcock open and the excess solvent to avoid any air bubbles. The excess THF elutes out as the beads settle and pack in the column. The column was packed with beads until the final level of the bed was ~4 inches from the top. Once the beads were completely packed, the stopcock was closed. It is important to make

sure that the column never runs out of the solvent to avoid drying of the beads. The SEC bed expands in volume when it is idle. Therefore, before loading any samples, the solvent above the bed level was eluted until the bed reaches a constant height. After the settled bed was flat and constant in height, the solvent above the bed was eluted to the level of the bed. The dissolved sample was taken in a 9" pasteur pipette and loaded carefully (drop by drop), spreading it across the surface as a thin layer. Then fresh mobile phase was added to allow the loaded the sample to enter the bed. The shape of the band was maintained flat by adding the solvent uniformly. The overloading of product would cause bleeding and reduce the separation. The samples are collected based on the band formed during elution and analyzed using mass spectrometry. This method can be repeated in many cases to accomplish the desired purity.[36]

1.3 Ligand exchange and core size conversion

Ligand exchange is a conversion method in which a pure Au NM is treated with an incoming ligand with elevated temperature. If the incoming ligand has similar steric and electronic property as the original ligand, the incoming ligand replaces the original ligand while maintaining the original core size. If the incoming ligand has different steric and electronic property, replacement of the original ligand with incoming ligand makes the gold core unstable and converts to the nearby stable size. The second conversion is known as core size conversion or transformation.[37-42] The core size conversion can be monitored using mass spectrometry like MALDI-MS & ESI-MS, and through UV-visible spectroscopy. Core size conversion can also be used to convert easily attainable pure Au NM in one ligand to a difficult to isolate Au NM in a different ligand of comparable size. Ligand exchange was first used in $Au_{25}(SR)_{18}$ along with the reported importance of ESI-MS.[43] The small change in mass

cannot be observed through any other normal electron microscopy or MALDI-MS. The high-resolution ESI-MS was required to monitor and manipulate the ligand exchange process.[43] The introduction of aromatic thiols brings a new set of Au NMs. Then, core size conversion plays a vital role by transforming aliphatic thiol protected Au NMs to aromatic thiol protected Au NMs of different number of Au atoms. In core size conversion, the reaction starts with normal ligand exchange. After certain exchanges, the Au core became unstable, and the Au core starts to convert. Then the Au core goes into stable Au NMs protected completely by new incoming ligand.[39-42]

1.4 Structure

The general structure of a gold thiolate NM consists of several layers: the innermost layer is an Au core, with surrounding Au shell(s) and an outer Au shell protected by the sulfur end of the ligand. The outer layer of the nanostructure is composed of staple motifs of (SR-

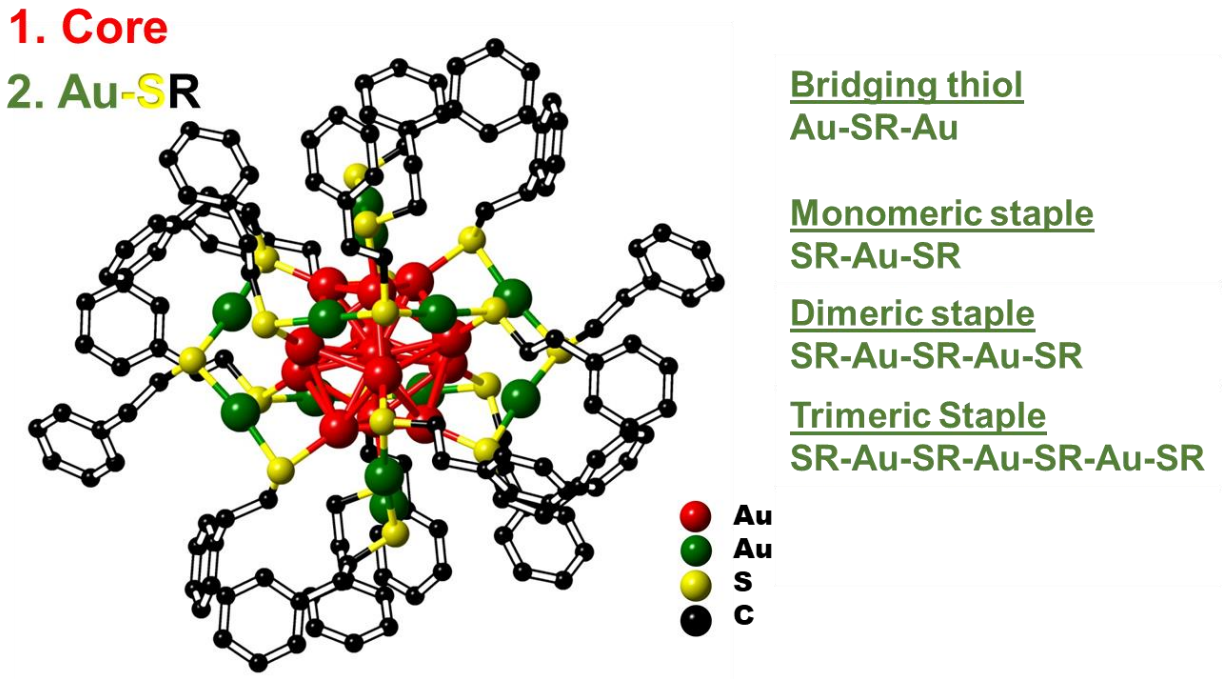

Figure 1.3. Crystal structure of $Au_{25}(SCH_2CH_2Ph)_{18}$. Showing the core and staple arrangement of the structure.

$Au\text{-}SR)_n$ which protect and cap the structure. There are a variety of staples motifs which can be arranged in several ways on the nanostructure. Common arrangements observed included: monomeric staple which is a motif consisting of SR-Au-SR, a dimeric which is SR-Au-SR-Au-SR, and trimeric SR-Au-SR-Au-SR-Au-SR. Several structures also have bridging thiols where the ligand is directly attached to the core (or outermost shell). Figure 1.3 shows the crystal structure model of $Au_{25}(SCH_2CH_2Ph)_{18}$ as an example; the core of this structure (red) consists of a Au_{13} icosahedral core, surrounded by 12 Au atoms in staple formation, making up a total of six dimeric staples surrounding the core.

1.5 Characterization Techniques

The purified Au NMs would be then analyzed by several analytical techniques to obtain information regarding their mass, composition, structure, optical and electronic properties. The stability and amenability of Au NMs eases characterizing using some kind of analytical techniques like MALDI-MS. The unambiguous data obtained from these analytical techniques gives complete understanding of the structure and properties of Au NMs.

1.5.1 Mass Spectrometry: Molecular weight, from which the atomic composition of the molecules can be obtained, is characterized using mass spectrometry. The introduction of mass spectrometry brought multitudes of advancement in the fields of biology and chemistry. Mass spectrometry provides mass spectrum which is a plot of ion abundance versus mass-to-charge ratio (m/z). In 1996, Prof. Whettens' pioneering work on characterizing gold nanoclusters using Laser desorption ionization mass spectrometry (LDI-MS) made mass spectrometry reliable an analytical tool for characterizing metal nanoclusters.[9]

MALDI-MS and ESI-MS are the two most commonly used mass spectrometry tools utilized for Au NMs characterization to date. MALDI-TOF-MS (matrix assisted laser desorption ionization-time of flight mass spectrometer) is used in order to make compositional assignments, determine purity and monodispersity of NMs.[44-45] ESI-MS is a softer ionization technique with little to no fragmentation and higher sensitivity which makes it a key component for compositional analysis based on the mass to charge ratio and isotopic distributions.[44, 46]

1.5.1.1MALDI-MS: In 1987, Kochi Tanaka and coworkers used combined cobalt nanoparticles in glycerol as a matrix to analyze mass spectrometry of larger biomolecules (~34 kDa). This method reduced the fragmentation from normal LDI-MS.[47] In 2008, Dass and coworkers have extensively studied the Au NMs in MALDI-MS using different matrices including sinapinic acid (SA), 4′-hydroxyazobenzene-2-carboxylic acid (HABA), universal MALDI Matrix and trans-2-[3-(4-tert-butylphenyl)-2-methyl-2-propenylidene] malononitrile (DCTB).[48] In this work, they have identified that MALDI-MS methodology based on DCTB matrix, facilitates the determination of complete molecular ion determination without fragmentation. Since then, DCTB matrix became the go to matrix in the field. As the sizes increase, MS analysis becomes challenging due to the resolution limit of the TOF tube. Thus, when compared to the smaller Au NMs (Au_{25}), $Au_{144}(SR)_{60}$ shows broad MALDI-MS signal. Both instrument resolution at high mass and laser induced fragmentation result in peak broadening. Thus, an alternative soft ionization technique is required to overcome the laser induced fragmentation and detect the intact molecular ions for large gold nanoparticles analysis.

1.5.1.2 ESI-MS: ESI-MS is a softer ionization technique compared to MALDI-MS and

produces intact molecular ions without fragmentation in most cases. Initially, the atomic composition of various glutathione protected gold clusters were determined using ESI-MS by Tsukuda and coworkers. [49-52] Then isotopically resolved ESI-MS data of $Au_{25}(SC_2H_4Ph)_{18}$ cluster that exactly matched the simulated spectra, brought out the importance of ESI-MS in the field.[43] Many recent reports have used ESI-MS for the compositional assignment of Au NMs.

ESI involves three major steps from samples in solution to gas phase ions entering the mass spectra.

i. Formation of tiny, charged droplets at electrospray capillary due to high voltage applied at the capillary.

ii. Solvent evaporation due to elevated source temperature and stream of dry N_2 gas pressure.

iii. Charged gas phase ions ejection from the charged droplet into the mass spectra. The Waters Synapt XS instrument in our lab has a quadrupole time-of-flight mass analyzer (QTOF); the charged gas phase ion enters the mass analyzer providing high resolution mass spectrometry data.

The advantage of the ESI process is the generation of multiply charged ions. It allows the analysis of large molecules and improves the sensitivity. However, multiply charge ions observed in the ESI does not reflect the actual charge state of the gold nanoparticles in the solution. It depends on the charge accumulation in the droplet and charge modification by the electrochemical process.

1.5.2 UV-visible Spectroscopy: Next to mass spectrometry, UV-visible spectroscopy is commonly used to characterize Au NMs. Au NMs < 2 nm exhibit molecular-like optical

absorption feature due to the HOMO-LUMO gap in its molecular orbitals. On the other hand, when the size becomes larger the HOMO-LUMO gap becomes smaller, at one point the gap closes up and eventually becomes a single band. Therefore, larger Au NMs exhibit surface plasmon resonance, which is the collective oscillation of the conduction band electrons in response to the incident radiation. Gold nanoparticles in this size range exhibit a surface plasmon resonance at 500-550 nm. UV-visible experiments are generally carried out in toluene, THF, or DCM. Generally, the 300-1100 nm wavelength region is examined for the electronic properties of nanomolecules.

1.5.3 Low Temperature UV-visible spectroscopy. Normal UV-visible generate preliminary electronic transition features. However, fine electronic transitions can be observed in low temperature UV-visible spectroscopy studies. This is accomplished using a specialized cryostat which is used in place of a traditional UV stage. Normally, the sample dissolved in a suitable solvent (typically 2-methyltetrahydrofuran) has been cooled using a cryostat to liquid nitrogen temperature of 77 K. At 77 K the molecules within the samples have negligible rotational and vibrational transitions and only electronic transitions are being facilitated. Therefore, absorbance peaks and valleys are amplified and more resolved.

1.5.4 Single Crystal X-ray Diffraction. Mass spectrometry allows formulating the Au NMs and its composition, while atomic arrangement remains unsolved. To understand the atomic arrangement, we need the total structural arrangement data. Single crystal X-ray diffraction (ScXRD) has been used to determine the total structure and is crucial in the determination of the atomic structures of Au NMs. When X-ray interacts with the crystal, it will diffract into directions. The angles and intensities of these diffracted X-rays will be measured to produce a 3D image of the density of electrons, which reflect the average

positions of atoms in the crystal. Essential information on physical and electronic properties can also be obtained through ScXRD.

The process of obtaining a ScXRD data includes growing crystals, crystal screening, data collection, refinement, and structure fitting. Among these steps growing a robust single crystal suitable for X-ray diffraction is the most challenging step.

i. Crystallization setup: Several crystallization techniques are available depending on the molecular size and its crystallization property. In our lab, we use three types of crystallization technique. First, solvent diffusion method. In this method the Au NMs are dissolved in a suitable solvent like toluene or DCM to which a non-solvent like acetonitrile or ethanol is vapor diffused over time in a closed system. Second, layering method. In this method, the Au NMs are dissolved in suitable solvent which is layered with non-solvent in a closed system where the non-solvent can diffuse through the liquid phase. Third, evaporation method. In this method, Au NMs dissolved in a suitable solvent are allowed to evaporate slowly in a partial open system. Depending on the conditions, crystals may grow or precipitate out. If precipitated, depending on the nature of the precipitation, other crystallization conditions and solvents will be attempted.

ii. Crystal screening: The crystal setups are usually kept for a week depending on how fast the crystal or precipitate is forming. Then the setup is viewed under a microscope. A good crystal should be large enough, pure in composition, and should be of high quality (without imperfections, multi-crystals, or twinning). The selection of good crystal is crucial.

iii. Crystal mounting and data collection: Selected crystal is attached to the tip of a MiTeGen MicroMount. Then the crystal is mounted in a stream of cold nitrogen at 100 K and

centered in the X-ray beam manually with the aid of a video camera. After initial scans, the data collection is started with suitable exposure time and angles.

iv. Data refinement and fitting: The collected data are indexed and refined using CrysAlisPro. Here, diffraction patterns obtained from different orientations of the crystal are converted into a three-dimensional electron density model using a method called Fourier transform. Olex2 software package is used for final data fitting.

CHAPTER 2

CORE SIZE CONVERSION OF $Au_{329}(SCH_2CH_2Ph)_{84}$ TO $Au_{279}(SPh\text{-}tBu)_{84}$ NANOMOLECULES

Part of the text and figures in this chapter reprinted (adapted) with permission from*: *Core size conversion of $Au_{329}(SCH_2CH_2Ph)_{84}$ to $Au_{279}(SPh\text{-}tBu)_{84}$ Senthil Kumar Eswaramoorthy, Naga Arjun Sakthivel and Amala Dass* J. Phys. Chem. C,* ***2019**, 123 (14), pp 9634–9639, Copyright 2019 American Chemical Society.*

Author Contributions

Senthil Kumar Eswaramoorthy developed the synthetic protocol, isolation, executed the core-size conversion reaction, and characterization techniques which includes ESI-MS, MALDI-MS, and UV-visible spectroscopy. Senthil Kumar Eswaramoorthy and Naga Arjun Sakthivel analyzed the data and validated the reaction pathway. Amala Dass directed the project and manuscript. All the authors contributed to the manuscript preparation.

2.1 Abstract

Here, we report the core-size conversion of $Au_{329}(SCH_2CH_2Ph)_{84}$ to $Au_{279}(SPh\text{-}tBu)_{84}$ plasmonic nanomolecules. The mass spectrometric studies have revealed unprecedented reaction pathway for the Au_{329} to Au_{279} core-size conversion reaction via three steps. First, ligand exchange with the 4-*tert*-butylbenzenethiolate occurs, followed by simultaneous ligand exchange and core-size conversion progressing with loss of one Au atom after another and finally, reaches completion with full ligand exchange on Au_{279}. Typically, a core-size

conversion occurs in nanomolecules which have molecular like nature with different sizes having different electronic and structural properties. In this case for the first time, both the reactant and the product possess plasmonic behavior and bulk face-centered cubic (FCC) structures. Also, this is the first report to study the core-size transformation involving a difference of 50 metal atom but identical 84 ligand count.

2.2 Introduction

Gold NMs, Synthesis of thiolate protected stable molecules of gold with molecular and metallic properties are highly pursued for various practical applications.[9, 33, 53-54] These molecules of gold, also known as gold nanomolecules (Au NMs) can be synthesized via bottom-up, direct synthetic protocols followed by post-synthetic treatment or top-down approach involving core size conversion of one stable Au NM to another.[53] As discussed earlier in introduction, the direct synthesis of Au NMs results in a polydisperse product, which produces a mixture of stable sizes upon thermochemical treatment (or etching) requiring purification to obtain pure Au NMs.[8] Meanwhile, ligand exchange or place exchange reactions on Au NMs have been shown to functionalize Au NMs with new ligand shell or to make new sizes via core-size conversion and tune the properties.[55-62] The core-size conversion is dictated by the ligand being employed in the reaction and each ligand has a unique series of discrete stable sizes with distinct structure and property.[14, 53]

Samples with high purity are desired for various structural and property studies and application development. Core-size conversion of Au NMs by ligand exchange with different ligands have proven to be a unique way to make pure Au NMs exclusively in high yields.[63] It is also referred to as ligand exchange induced size/structural transformation (LEIST).[64] It

has been shown to circumvent the need for demanding purification processes in obtaining pure Au NMs in high yields, for example: Au_{30}, Au_{36}, and Au_{133}.[39, 65-68] Sequential etching of a crude samples with different types of ligands has been shown to produce pure, stable Au NMs. Sequential etching differs from core-size transformation in that the ligands employed in the sequential etching process are of same class that support the Au NM size of interest without inducing core-size conversion while destabilizing other sizes , thus yielding the desired Au NMs in high purity. For example: pure Au_{36} has been obtained in high yield by sequential etching of a polydisperse phenylethanethiolate (PC2) protected gold nanocluster crude mixture with thiophenol and 4-tert-butylbenzenethiol (TBBT).[67]

Significant progress has been made towards understanding the transformational and controlled ligand exchange chemistry in Au NMs with Au < 50 atoms.[53, 62, 69-71] Transformation from one stable size to another provides access to an entirely new set of properties than the precursor Au NMs whereas controlled ligand exchange retains the core-structure but tunes the electronic property. For example, $Au_{38}(SC_2H_4Ph)_{24}$ with thiophenol forms Au_{36} and Au_{38} under thermodynamic and kinetically controlled reactions, respectively.[72] The thermodynamic product[73] (Au_{36}) has entirely different atomic and electronic structure with higher band gap than the precursor whereas the kinetic product[72] (Au_{38}) has similar atomic structure and optical features to the starting NM. In some cases, interconversion between two stable sizes has been observed as well.[65, 74] Recently, new branches of core-conversion reactions such as oxidation induced core-size conversion[75] and fusion of Au_{25} to Au_{38} without any co-reactant[76] have been demonstrated.

To date, only little information is known on the transformational chemistry of Au NMs with Au > ~100 atoms and plasmonic nanocrystals. Au_{99}, Au_{102}, Au_{103}, and Au_{133} are the four

larger Au NMs that have been synthesized via core-conversion method.[38-39, 68, 77-78] However, the core-conversion on the plasmonic regime has not been studied in detail. In that plasmonic nanocrystal regime, smallest thiolate protected metallic gold nanocrystal, Faradaurate $Au_{279}(TBBT)_{84}$ has been recently reported.[33, 79-81] Au_{279} has been obtained by direct synthesis[33] and sequential etching[81] of a polydisperse phenylethanethiolate protected gold nanocluster crude mixture with phenylethanethiol followed by 4-*tert*-butylbenzenylthiol and core-conversion with TBBT.

As discussed earlier, each ligand type forms a unique series. The aliphatic phenylethanethiol (PC2) thiolate protected Au NMs series have been studied over two decades, but these aliphatic systems are difficult to crystallize.[9, 82-83] The introduction of rigid and bulky thiolated ligands such as TBBT favors the single crystal growth.[84] In recent times, aromatic-TBBT protected Au NMs series are widely studied and all the sizes in the TBBT series have been crystallographically resolved.[14] Au_{279} is the largest crystal structure of thiolate protected Au NMs reported to date.[33] The core size conversion of highly stable, molecule-like Au NMs in aliphatic thiolate series with TBBT provides stable sizes in TBBT series (Au_{25} to Au_{28}, Au_{38} to Au_{36} and Au_{144} to Au_{133}).[64] However, the core-conversion beyond 34 kDa especially on the plasmonic regime has not been studied in detail. In this work we have investigated the core-size conversion reaction of $Au_{329}(SC_2H_4Ph)_{84}$, the next stable size in aliphatic thiolate protected series of Au NMs[17, 54] to $Au_{279}(TBBT)_{84}$ by electrospray ionization (ESI) and matrix assisted laser desorption ionization (MALDI) mass spectrometry and absorption spectroscopy.

2.3 Results and Discussion

The Au_{329} plasmonic Au NMs are synthesized using two phase Brust method and isolated using SEC. The detailed synthesis is explained in experimental section.

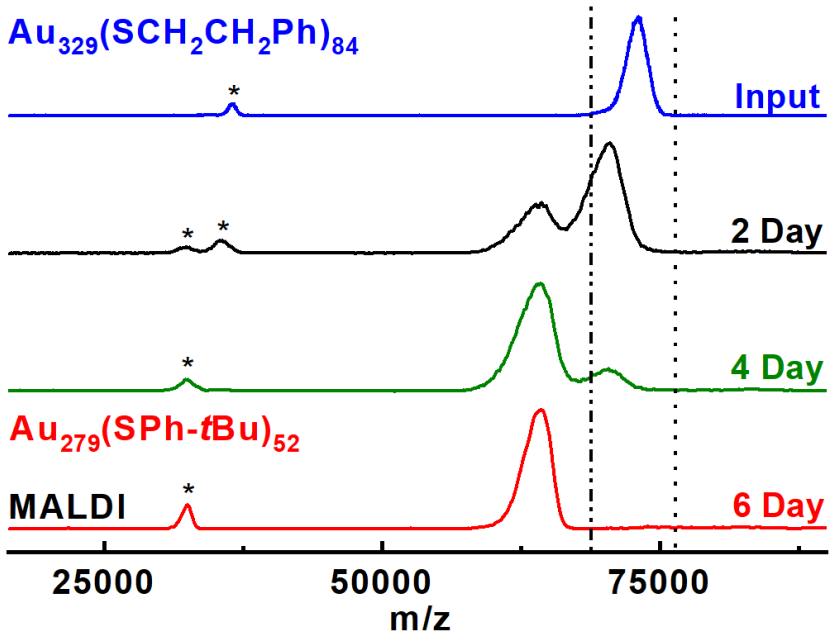

Figure 2.1. MALDI mass spectra of the starting material $Au_{329}(SCH_2CH_2Ph)_{84}$ and its transformation to $Au_{279}(SPh\text{-}tBu)_{84}$ on reacting with TBBT at 80 ^{0}C over 6 days. The dot and dash-dot-dot vertical lines corresponds to the molecular mass of Au_{329} and Au_{279}, respectively. * Indicates the 2+ charge state of respective nanomolecules.

2.3.1 Core size conversion. Figure 2.1 reveals the reaction progress through by MALDI-MS, where Au_{329} (input) is converted into Au_{279} after six days of reaction with TBBT at 80 °C. The dot and dash-dot-dot vertical lines corresponds to the molecular mass of Au_{329} and Au_{279}. Due to fragmentation under laser beam, only mass distribution of the Au NMS was seen in MALDI-MS. The multiple charge state peaks especially 2+ can be observed in MALDI-MS spectra, but they are less intense than the molecular ion peak mass due to fragmentation under the laser beam. The 2+ charge state peaks (indicated using *) are shown in Figure 2.1. The MALDI-MS of Au_{329} reveals the 1+ and 2+ peaks at ~73 kDa and ~36.5 kDa, respectively

(Figure 2.1). After 2 days of reaction, two new peaks were observed at ~64.5 kDa and ~32.5 kDa corresponding to 1+ and 2+ charge states of Au_{279} respectively, indicating the onset of Au_{329} to Au_{279} core-size conversion. Also, the peak maxima of Au_{329} have moved from ~73 kDa to ~70 kDa due to the core-size conversion. When the reaction reaches 4 days, sample reveals that the ~64.5 kDa peak becoming prominent and ~70 kDa peak intensity becoming less prominent as the reaction proceeds (Figure 2.1). The complete core-size conversion to

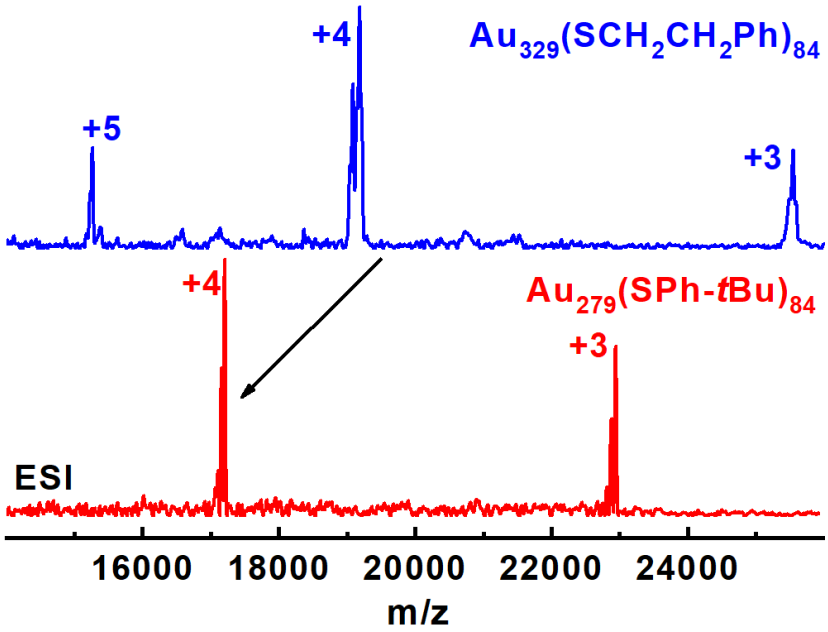

Figure 2.2. ESI-MS of $Au_{329}(SCH_2CH_2Ph)_{84}$ transforming to $Au_{279}(SPh\text{-}tBu)_{84}$ upon reacting with TBBT at 80 ^{0}C for 6 Days.

Au_{279} was observed after 6 days of reaction with only (1+ and 2+) peaks corresponding to Au_{279} observed in the MALDI-MS spectra (Figure 2.1).

ESI-MS was employed to further study the core-size conversion reaction in detail. Figure 2.2 shows the ESI mass spectra of the starting material (Au_{329}) and the final product (Au_{279}). Au_{329} has a molecular weight of 76,329 Da and it was observed in 3+, 4+, and 5+ charge state peaks at 25,546 Da (3 Cs adducts), 19,182 Da (4 Cs adducts), and 15,267 Da respectively (Figure 2.2). The final product $Au_{279,}$ has a molecular weight of 68,836 Da and it

ionized in 3+ and 4+ charge states with peaks at 22,944 Da and 17,208 Da, respectively. The core-size conversion reaction was completed after 6 days, and it was evidenced by both ESI and MALDI mass spectra.

2.3.2 Revealing 3 stages of conversion through ESI-MS. The $Au_{329}(PC_2S)_{84}$ to $Au_{279}(TBBT)_{84}$ reaction proceeds in three stages, first ligand exchange with TBBT occurs, followed by simultaneous core-size conversion and ligand exchange reaction, and finally reaction reaches completion with complete ligand exchange by TBBT ligands. Figure 2.3 reveals the ESI-MS data of the 3+ charge state in 22 – 28 kDa m/z range for a 2-day reaction sample. Intriguingly, the thiolate ligands on the monolayer count remains 84 throughout. It is worth noting that, mass spectrometry of larger nanomolecules is difficult and as the ligand exchange and/or core-size conversion reactions are performed on large nanomolecules,

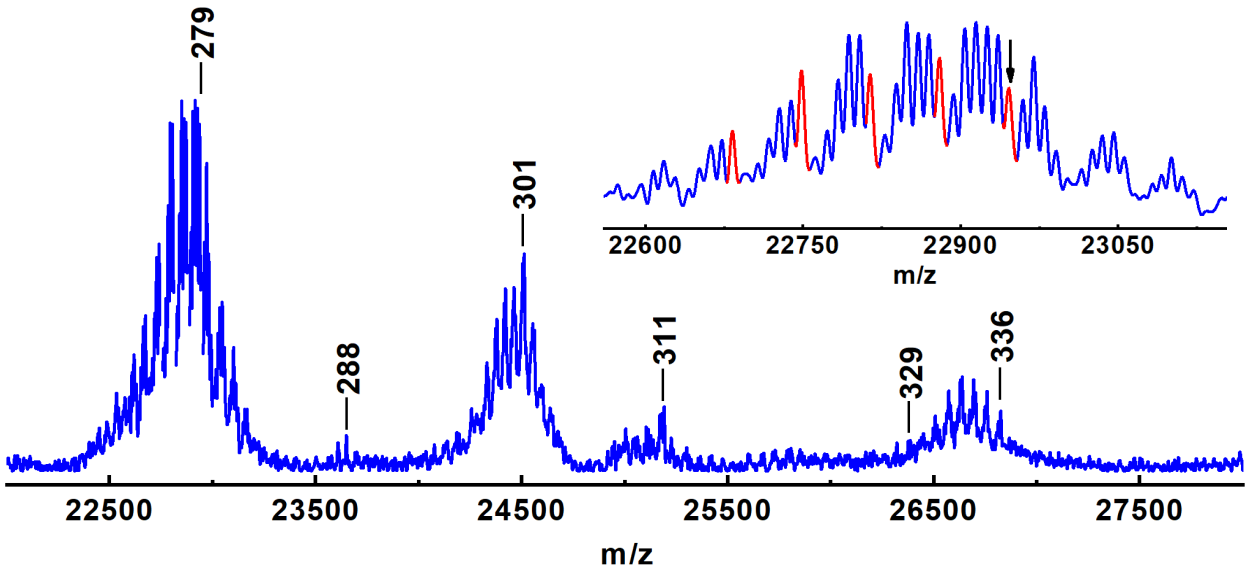

Figure 2.3. ESI-MS spectra of a 3+ peak in 2 days reaction sample showing the occurrence of ligand exchange and core-size conversion simultaneously. The peak assignment of 288, 301, 311, 329, 336 Au atoms has 84 TBBT ligands and 3 Cs^+ adducts with it. Inset is in 22.5 – 23.1 kDa range to reveal the Au_{279} formation (indicated by red peak with an arrow). Full spectrum is provided in the Figure S1.1.

analyzing the reaction progress becomes increasingly difficult. The Cs+ ions are used to facilitate better ionization of the sample. The mass difference between PC_2S (137.22 Da) and TBBT ligands (165.27 Da) is 28.06 Da. Therefore, a 3+ charge state peak corresponding to the ligand exchange reaction would have an envelope of peaks with mass difference of 9.3 Da. Additionally, changes in the number of gold atoms during core-size conversion and varying Cs^+ adduct formation poses another challenge in analyzing the data. The compositions for the intermediate samples were assigned based on the multiple charge state peaks and in some cases, there are close overlap between two possible combinations and the probable assignments have been included in this report.

Figure 2.3 reports the ESI-MS data for 2-day sample in the 3+ charge state region of 22 – 28 kDa and inset shows the 22.5- 23.1 kDa range to reveal the core-size conversion and ligand exchange reaction proceeding simultaneously. In the first stage, $Au_{329}(PC_2S)_{84}$ undergoes ligand exchange to form $Au_{329}(TBBT)_{84}$ with few un-exchanged PC_2S ligands. The $Au_{329}(TBBT)_{84}$ composition is metastable, and the reaction proceeds to core-conversion phase leading to another metastable size after well-known (329,84) composition up to $Au_{336}(TBBT)_{84}$ with increments of one Au atom, i.e., 329, 330, 331, …, 336 (Figure 2.3). The second stage starts at second day where MALDI-MS data for 2-day sample (Figure 2.1) also corroborates the formation of Au_{279} core and Figure 2.3 inset shows envelope of peaks and the fully exchanged $Au_{279}(TBBT)_{84}^{3+}$ at 22,945 Da (red peak indicated by an arrow). The inset has about 8 envelopes of peaks and their exact mass are listed in Table S1.1. The peaks indicated in red to the left of $Au_{279}(TBBT)_{84}^{3+}$ have a m/z difference of 66 Da corresponding to one Au atom and its composition is $Au_{278}(TBBT)_{84}^{3+}$. Similarly, the adjacent mass difference between the red peaks is 66 Da corresponding to one Au atom and their

compositions are $Au_{277}(TBBT)_{84}^{3+}$, $Au_{276}(TBBT)_{84}^{3+}$, and $Au_{275}(TBBT)_{84}^{3+}$. The envelope of blue peaks adjacent to red peaks corresponds to unexchanged PC_2S ligands with ~9 Da difference.

In final stage, the core-size conversion to stable $Au_{279}(TBBT)_{84}$ occurs (Figure 2.4). After 4 days of reaction only a few unexchanged PC_2S ligands are observed near the molecular peak (Figure 2.4, olive spectra). The $Au_{279}(TBBT)_{84}$ then resolves to be the prominent stable compound and $Au_{278}(TBBT)_{84}^{3+}$ and $Au_{277}(TBBT)_{84}^{3+}$ peaks were also observed but not as significant as 2 or 4-day samples. The Au_{278}, Au_{277} and Au_{276} are intermediate which are stable for a certain period and eventually they converge towards Au_{279} as the reaction progresses. Similar phenomena with one Au atom difference during core-size conversion of larger nanomolecules has been observed as a kinetic product in the transformation Au_{144} of Au_{133} where $Au_{132}(TBBT)_{52}$ was present during intermediate samples and goes down in intensity

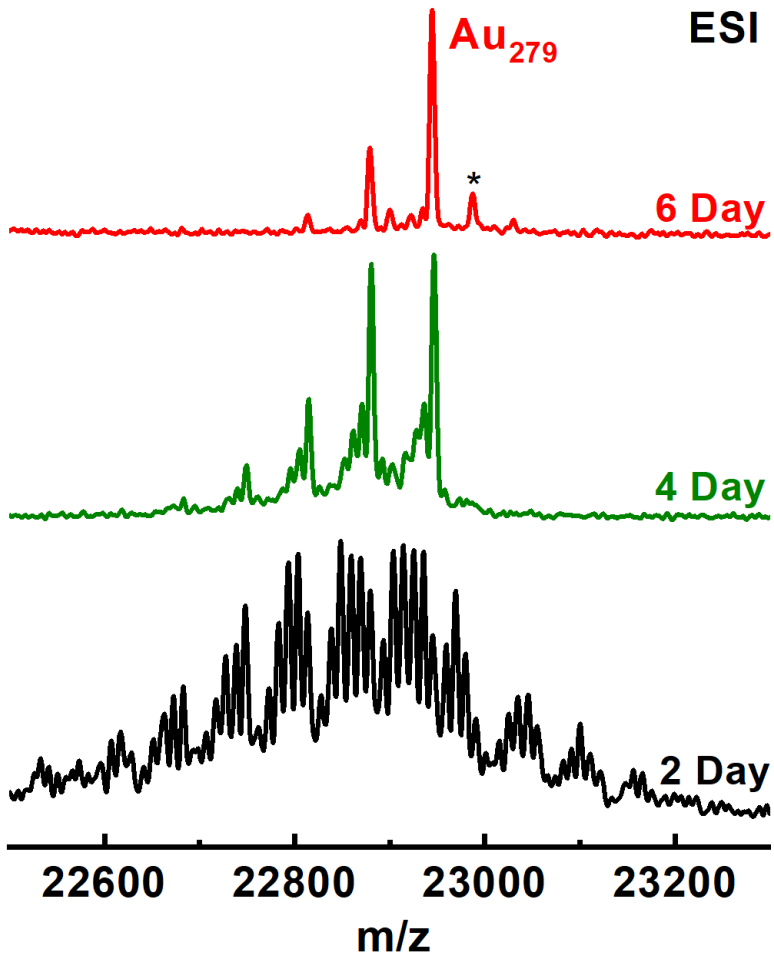

Figure 2.4. Electrospray ionization mass zoom in spectra of the intermediates, showing the ligand exchange and conversion.

with time and negligible towards the end.[39]

2.3.3 Optical Spectroscopy. The molecule-like nanomolecular core-size conversion involves striking changes in optical properties between the starting material and product.[53] Absorption spectroscopy was performed to study how the optical property of plasmonic nanomolecules would be affected by the core-size conversion reaction. The optical property of the starting material (Au_{329}) and the product (Au_{279}) are compared in Figure 2.5. The blue curve in Figure 2.5 corresponds to Au_{329}. The UV-visible absorption spectrum of Au_{329} has a plasmonic band centered ~495 nm and upon transformation to Au_{279} by reacting with TBBT, the product also exhibits a SPR band, however, it is red shifted to ~510 nm. It worth nothing that, despite the loss of 50 Au atoms, the molecule is still plasmonic and the manifestation of SPR on 279 has been attributed to the presence of phenyl rings.[79]

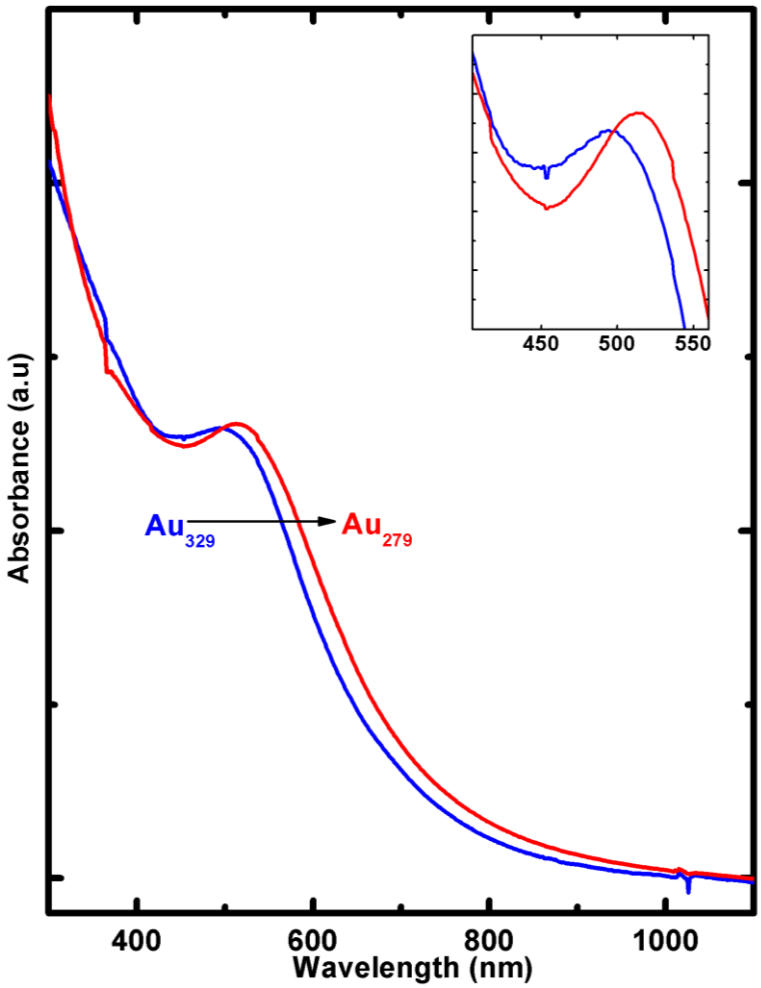

Figure 2.5. UV-visible absorption spectrum of final material $Au_{279}(SPh\text{-}tBu)_{84}$ nanomolecules in toluene in comparison with the starting material $Au_{329}(SCH2CH2Ph)_{84}$

2.4 Experimental

2.4.1 Materials. Tetrachloroauric (III) acid ($HAuCl_4{\cdot}3H_2O$,>99% metal basis, Aldrich), Sodium borohydride ($NaBH_4$, 99%), 4-tert-butylbenzenethiol (TCI, 99%), phenylethylmercaptan, (Sigma-Aldrich), cesium acetate (Acros, 99%), anhydrous ethyl alcohol (Acros, 99.5%), and trans-2-[3[(4-tertbutyl-phenyl)-2-methyl-2-propenylidene] malononitrile (DCTB matrix) (Fluka ≥ 99%). HPLC grade solvents such as tetrahydrofuran, toluene, methanol, butylated hydroxytoluene stabilized tetrahydrofuran were obtained from Fisher Scientific. All the materials were used as received.

2.4.2 Synthesis. The core-conversion of $Au_{329}(SCH_2CH_2Ph)_{84}$ to $Au_{279}(SPh\text{-}t\text{Bu})_{84}$ was performed in two primary steps: namely Au_{329} synthesis and core-conversion of Au_{329} to Au_{279}. First, $Au_{329}(SCH_2CH_2Ph)_{84}$ was synthesized by slightly modifying the previously reported method. $Au_{329}(SCH_2CH_2Ph)_{84}$ preparation was carried out in three steps. First, crude nanoparticles were synthesized which contain polydisperse gold nanoparticles with metastable sizes. Then thermochemical treatment was done on the crude sample to narrow down the size and to remove the metastable clusters. Then, $Au_{329}(SCH_2CH_2Ph)_{84}$ was isolated using size exclusion chromatography. Finally, $Au_{329}(SCH_2CH_2Ph)_{84}$ was subjected to ligand exchange with TBBT, and it undergoes core-size conversion to form $Au_{279}(SPh\text{-}t\text{Bu})_{84}$.

Step 1: Au_{329} synthesis. $HAuCl_4.3H_2O$ (0.1 g) was dissolved in distilled water (10 ml) and TOABr (0.15 g) was dissolved in toluene (10 ml) separately. They were mixed together in a 100 ml round bottom flask under stirring (500 rpm). The mixture was stirred for 30 min. The organic layer was separated and placed in an ice bath for 30 min. Then, 70 µL of phenylethanethiol (Au:thiol = 1:2) was added and the reaction was allowed to stir for 1 hr.

The reaction mixture was then reduced by rapidly adding 0.1 g NaBH4 (Au:$NaBH_4$ = 1:10) dissolved in 5 ml of ice-cold water. The solution changes to black color indicating the formation of nanoparticles. The stirring was continued for about 24 hr. The organic phase was then separated, and rotary evaporated to remove the solvent. The crude product was washed with methanol and water mixture (3-4 times) to remove excess thiol and byproducts. The crude product was dissolved in toluene and etched with excess phenylethanethiol (60 mg crude product, 0.5 ml toluene and 0.5 ml of thiol) for ~3 days at 80 °C. Then, the etched product was rotary evaporated to remove the solvent and washed with methanol to remove excess thiol. Finally, $Au_{329}(SCH_2CH_2Ph)_{84}$ was isolated by size exclusion chromatography.

Step 2: In this step, $Au_{329}(SCH_2CH_2Ph)_{84}$ dissolved in toluene was subjected to ligand exchange with tert-butylbenzene thiol for 6 days at 80 °C. In this reaction, for 1 mg of starting NM 10 µL of toluene and 10 µL of thiol was used. The transformation of $Au_{329}(SCH_2CH_2Ph)_{84}$ to $Au_{279}(SPh\text{-}tBu)_{84}$ was monitored by MALDI and ESI mass spectrometry.

2.4.3 Instrumentation. The MALDI spectra were acquired from Voyager DE PRO MALDI-TOF-MS instrument with DCTB matrix. Electrospray ionization mass spectra (ESI-MS) were collected from Waters Synapt Q-TOF HDMS with THF as the solvent. Baseline correction for Au_{329} ESI-MS spectra was done by polynomial fitting (Figure 2.2). The cesium acetate was used to facilitate the ionization of nanomolecules with multiple charge states. The UV-visible absorption spectra were measured using a Shimadzu UV-1601 spectrophotometer.

2.5 Conclusions

In summary, we have studied the core-size conversion of Au_{329} to Au_{279} by using MALDI and ESI mass spectrometry, and UV-visible absorption spectroscopy. The core-size conversion takes place in three steps, first ligand exchange, then ligand exchange and core-size conversion occur simultaneously and finally reaction completion with complete ligand exchange by exogenous ligands. The mass spectrometric results have revealed the unprecedented reaction pathway involving ligand exchange and core-size conversion with loss of one gold atom after another, retaining a constant 84 ligand monolayer count. The optical absorption studies have shown that both the starting material and the product are plasmonic as reported.[79]

CHAPTER 3

DIGESTIVE RIPENING YIELDS ATOMICALLY PRECISE GOLD NANOMOLECULES

Part of the text and figures in this chapter are reprinted (adapted) with permission from: Eswaramoorthy, S. K.; Dass, A., Digestive ripening yields atomically precise Au nanomolecules. New J. Chem.* ***2021,* *45 (43), 20241-20248; Copyright 2021, New Journal of Chemistry*

Author Contributions

Senthil Kumar Eswaramoorthy developed the synthetic protocol, conducted mass spectrometric, UV-visible absorption, and wrote the manuscript. Amala Dass assisted in experimental design, data analysis, and edited the manuscript. Both authors made substantial, direct, and intellectual contribution to the work in the manuscript preparation and discussion.

3.1 Abstract

Digestive Ripening (DR) is a synthetic method where a polydisperse colloid of metal nanoparticles upon refluxing with free ligand in high boiling point solvent gives size monodisperse nanoparticles. Brust synthesis is known to form atomically monodisperse thiolate protected gold nanoparticles also known as gold nanomolecules (Au NMs). Unlike Brust method which gives smaller 1-3 nm atomically precise nanomolecules, DR has been used only for the synthesis of large >5 nm nanoparticles with good size monodispersity. In thiolate protected gold nanoparticle Brust synthesis, first the yellow-colored phase

transferred Au(III) solution is converted to colorless Au(I) mixture by adding thiol in certain molar ratio which forms Au-SR. The mixture is then reduced using reducing agent to form black colored Au NMs. Whereas in DR, while using the same primary chemicals, the two steps were reversed: the mixture was reduced before the addition of thiol. Here we show that in DR adding thiol after 2 minutes of reduction gives larger 5 nm particles as reported, whereas adding thiol in 30 seconds after reduction results in smaller < 2 nm particles. By pursuing this reaction time and formation of smaller nanoparticles, in this work for the first time we report, DR yields atomically precise $Au_{25}(SR)_{18}$ and $Au_{144}(SR)_{60}$ NMs. This is reported using two aliphatic thiols: hexanethiol and dodecanethiol as the protecting ligand. DR was also repeated using an aromatic thiol, 4-tert-butyl benzene thiol (TBBT) which yields $Au_{279}(SR)_{84}$ NMs consistent with the Brust method. Thereby establishing both DR and Brust method leads to the formation of atomically precise Au NMs, regardless of the order of thiol addition and reaction steps.

3.2 Introduction

The nanosized metal particles attract huge interest in catalysis, optics, and drug delivery because of its remarkable difference in physical and chemical properties from the respective bulk metals.[2] The nanosized metal particles usage dates back to 4th Century AD, the Lycurgus cup.[3] It has unusual optical effects due to the presence of gold and silver nanoparticles. The size of the particle determines its properties. The catalytic property of noble metals is enhanced when their size is reduced to the nanoscale.[85-86] Currently, the synthesis of highly monodisperse metal nanoparticles (NPs) is an attracting field. The size-controlled synthesis of NPs is achieved by manipulating the synthetic conditions. [87-88]

The research of monolayer thiol protected gold nanoparticles (Au NPs) has developed significantly after the introduction of the Brust[7] method. It is a two-phase synthesis (water/toluene) which was later tuned to form atomically monodisperse nanoparticles, also called gold nanomolecules (Au NMs).[8-11] The first major development in the field was tuning the method forming monodisperse Au nanoclusters evidenced by mass spectrometric studies reported by R.L Whetten et al.[9] The next major development, was the crystal structure determination of Au_{102}(p-MBA)$_{44}$ and $Au_{25}(SCH_2CH_2Ph)_{18}$ proving the atomically monodisperse nature beyond any doubt.[10-11] Later, many other crystal structures have been reported, especially using bulky ligands such as 4-*tert*-butylbenzene thiol (TBBT)[33, 40, 68] and *tert*-butyl thiol.[89-91] Various sizes of NMs protected by different thiolate ligands were obtained by introducing some modifications in the Brust method. But, the basic 3 steps are the same in every Brust method, (i) phase transfer, (ii) addition of thiol, and (iii) reduction using a reducing agent.[7-11, 92] In most cases, the basic steps forming the crude mixture involve an etching process to obtain stable sizes. [93]

Ostwald ripening, a diffusion-controlled crystal growth process used for the formation of nanoparticle was proposed in the early to mid-20th Century. In a supersaturated solution, a small change like concentration fluctuation produces a nucleus of a new solid phase which leads to the formation of the nuclei until the degree of supersaturation becomes minimum.[94] Then coalescence occurs in a way that the particles which have a size larger than critical size will incorporate smaller size particles and grow. The theory of Ostwald ripening was introduced in the work of Lifshitz and Slyozof[95] and further advanced by the work of Wagner,[96] together called LSW theory.

Digestive ripening (DR) which is also known as inverse Ostwald ripening, involves

the etching or dissolution of large NPs into smaller, more stable NPs in the presence of excess capping ligands at a high temperature.[97-99] DR is one of the commonly used method for synthesizing various sizes of nanoparticles with size monodispersity in different transition metals.[99-101] Various factors affecting the monodispersity and property of the product nanoparticle have been widely studied for this method.[99-105] DR method is also used to synthesize monolayer thiol protected Au NPs. But the synthesis of atomically monodisperse nanoparticles using the DR method is not yet achieved. In this report we demonstrate in DR using Transmission Electron Microscopy (TEM), adding thiol after 2 minutes of reduction gives larger 5 nm particles as reported, whereas adding thiol in 30 seconds after reduction results in smaller < 2 nm particles. Thereby, we report (i) atomic precision can be achieved in DR by reducing timing (time difference) between reduction of mixture and addition of thiol. (ii) DR yields atomically precise $Au_{25}(SR)_{18}$ and $Au_{144}(SR)_{60}$ NMs. This is reported using two aliphatic thiols: hexanethiol and dodecanethiol as the protecting ligand consistent with reported Au NMs from Brust method.[11, 48, 106] DR was also repeated using an aromatic thiol, TBBT, which yields $Au_{279}(SR)_{84}$ NMs.[33] It is consistent with the reported Au NMs from Brust method. Mass spectrometric analysis confirms the atomic precision. (iii) The switching of phase transfer agent to ToABr in DR brings all the same chemicals (reactants) used for DR and Brust method, but the steps are different. Especially step two and three mentioned earlier in the Brust method were reversed in DR, but both pathways lead to the formation of atomically precise Au NMs.

3.3 Results and Discussion

The step-by-step synthetic procedure comparison of Brust and DR methods is shown

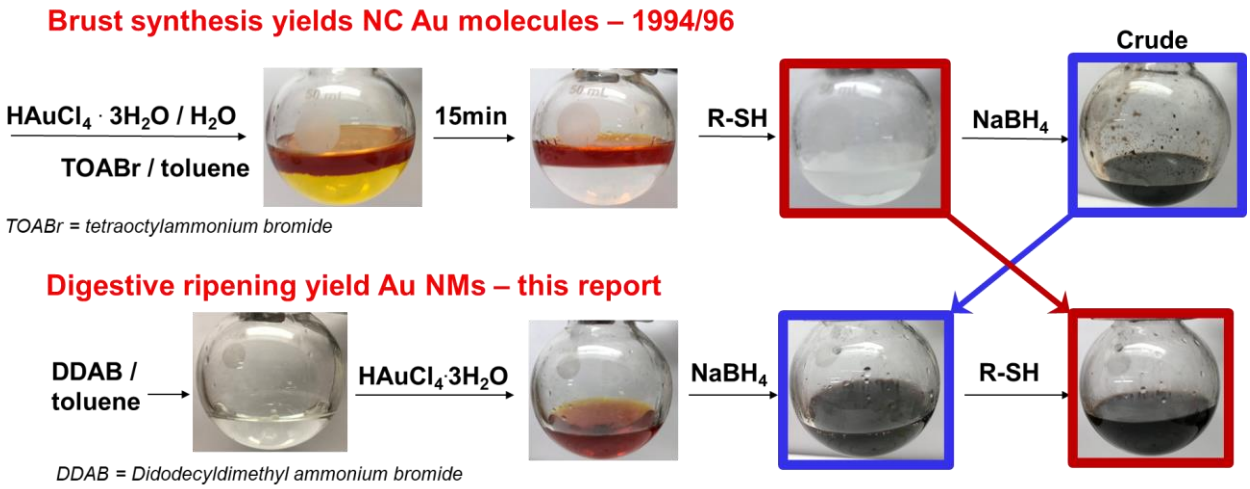

Scheme 3.1. Synthetic procedure of Brust synthesis method yielding Nanocrystal gold molecules which was reported in 1994 and 1996 directly compared with Digestive Ripening yielding gold nanomolecules reported in this work.

in Scheme 3.1. The important difference appears at a distinctive step (highlighted using blue and red box), where the reduction of the mixture and addition of thiol are exchanged. The comparative color change happening in the reactants at each step was evident in the scheme. Brust synthesis method was already known to form atomically precise Au NMs whereas DR is known to form size monodisperse Au NPs (not atomically monodisperse). Here, DR also leads to the formation of atomically precise Au NMs, using the reported synthetic protocol, which provides the unprecedented results explained below.

3.3.1 Formation of atomically precise small nanoparticles in DR. The DR synthesis was done as mentioned in Scheme 3.1. Briefly, the Au salt was dissolved in toluene using a phase transfer agent, followed by reduction, and then the addition of capping ligand to the mixture. See the experimental section for more details. Normally in DR after reduction of the mixture the reaction is continued to completion before adding thiol. In Brust method the thiol was already present while reducing the mixture. Here, in DR to obtain smaller gold nanoparticles, we noticed that the timing between the reduction of mixture and addition of

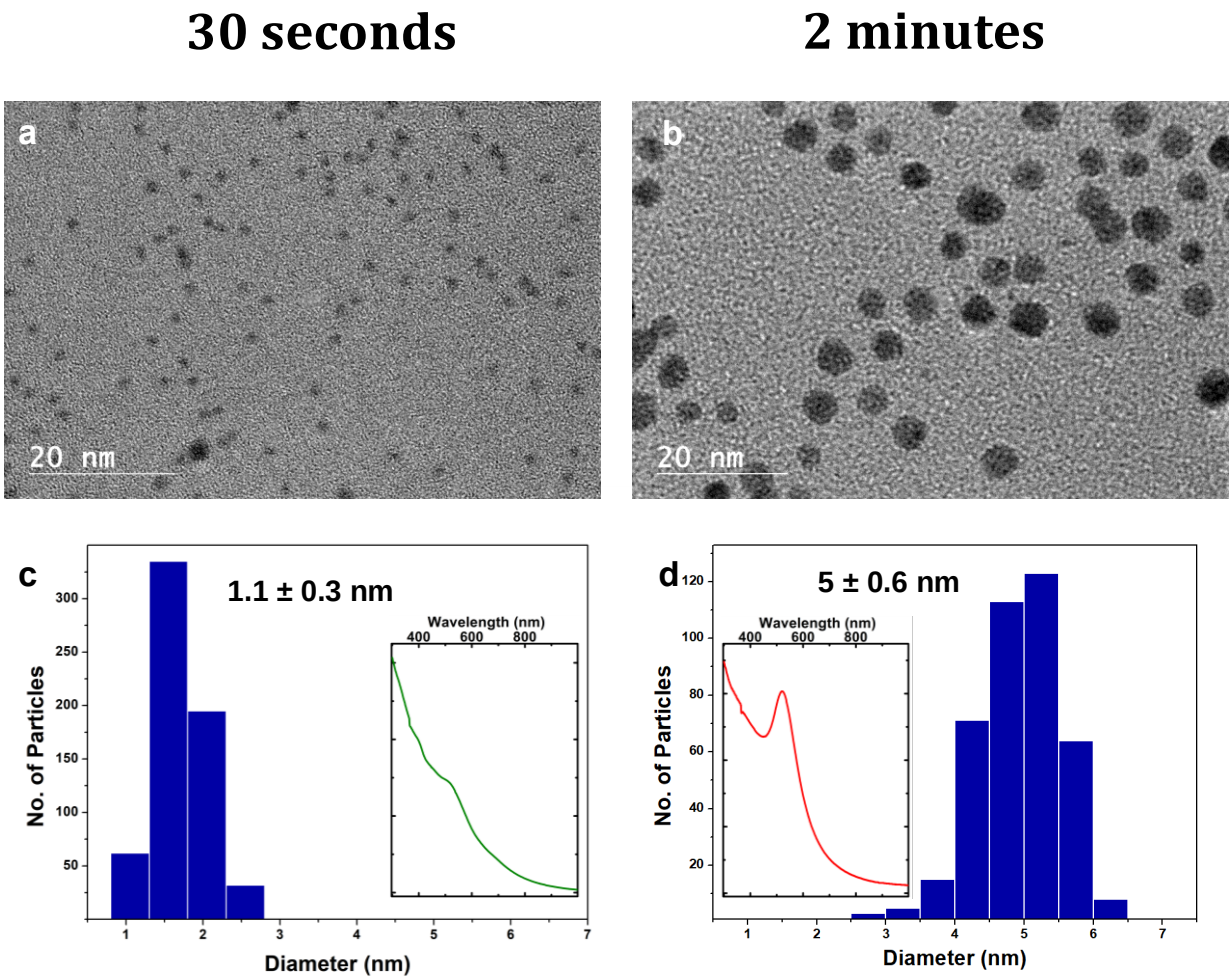

Figure 3.1. Addition of thiol after 30 seconds of reduction, a) TEM image and c) size distribution plot of its product (UV-visible spectra in the inset). Addition of thiol after 2 minutes of reduction b) TEM image and d) size distribution plot of its product (UV-visible spectra in the inset).

thiol is crucial. Therefore, addition of thiol was done in two-time differences, soon after the reduction (30 seconds) and after some time (2 minutes). Transmission Electron Microscopy (TEM) image (Figure 3.1a) of 30-seconds DR product shows particles less than 5 nm in size and its size distribution analysis done by measuring the size of 600 particles provides 1.1 ± 0.3 nm (Figure 3.1c). the size distribution was measured using standard deviation. TEM image of 2-minute DR product (Figure 3.1b) shows comparatively larger monodisperse

spheres and its size distribution based on 400 particles provides 5 ± 0.6 nm (Figure 3.1d). The particle size drastically dropped from 5 nm (Figure 3.1d) to 1.1 nm when reducing the timing from 2 minutes to 30 seconds. UV-visible spectra of 2 minutes product shown in the inset of Figure 3.1d has a prominent plasmonic band centered at ~500 nm whereas the plasmonic feature diminished to a small band in 30 seconds sample (Figure 3.1c inset). This UV-visible spectrum comparison further confirms the drastic drop in size of resulting product by reducing the timing. The addition of capping agent (thiol) soon after reducing the mixture (30 seconds) stops the aggregation of Au into a larger nanoparticle and leads to the formation of particle in Au nanomolecule regime (1 to 2 nm).[15, 107] Further refluxing of the mixture brings all the metastable Au nanoclusters into more stable atomic precise Au NMs.

3.3.2 DR yields Au NMs with aliphatic thiols. The DR product was then analyzed in Matrix Assisted Laser Desorption Time of Flight (MALDI-MS) mass spectrometry using the DCTB matrix.[48] The low and high laser intensity MALDI-MS data exhibits various sizes in the product. In high laser intensity, the nanoclusters tend to fragment, but higher laser fluence is needed to ionize all the sizes present in the product. The high laser data of hexanethiol protected Au NMs product in Figure 3.2a illustrates the presence of two kinds of size distribution in the product, namely at 7 and 30 kDa. The broad 30 kDa peak represents that it has two sizes in it. The higher laser pulse also tends to remove the loosely bound surface ligands. Therefore, the mass is only the core mass which consists of gold atoms only. The laser influence in MALDI-MS tends to give characteristic fragmentation of $Au_4(SR)_4$ for small NMs.[72] The exact mass with high accuracy can be determined with Electrospray Ionization Mass Spectrometry (ESI-MS). The ESI-MS spectrum in Figure 3.2b predominantly shows three sizes of nanoclusters, namely $Au_{25}(SR)_{18}$, $Au_{137}(SR)_{56}$, and $Au_{144}(SR)_{60}$. The $Au_{25}(SR)_{18}$

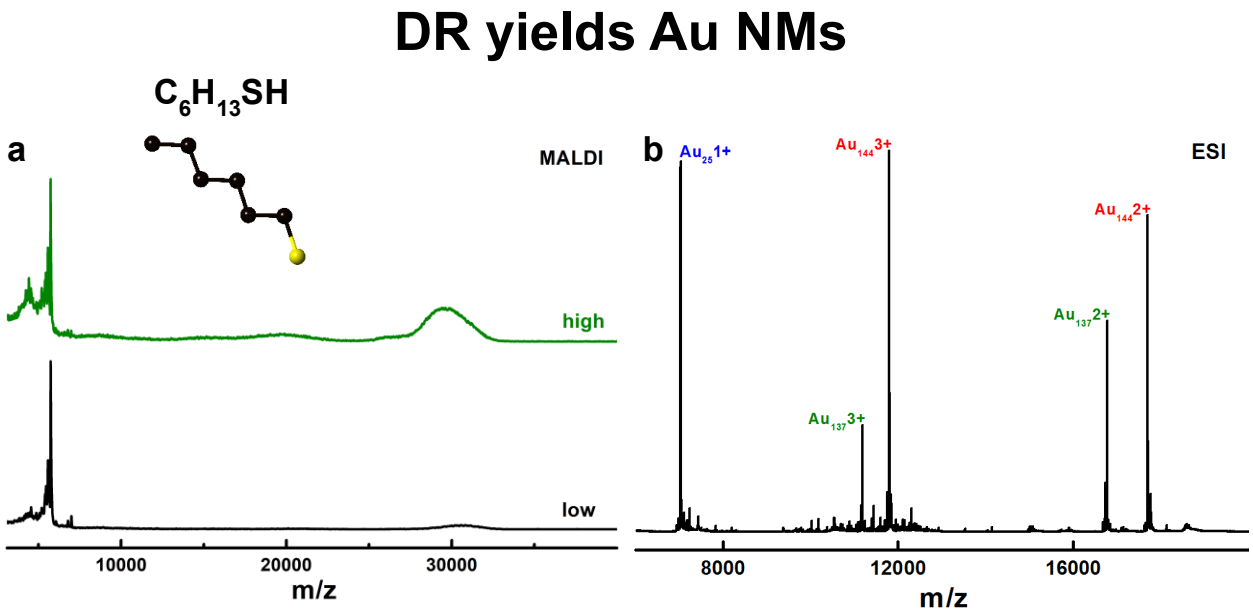

Figure 3.2. Mass spectrum of the digestive ripening synthesis product showing atomically precise nanomolecules protected by hexanethiol. (a) MALDI-MS data of digestive ripening synthesis product showing high (green) and low (black) laser. (b) ESI-MS data of the same product showing the presence of $Au_{144}(SR)_{60}$, $Au_{137}(SR)_{54}$ and $Au_{25}(SR)_{18}$ species.

corresponds to the 7 kDa and $Au_{137}(SR)_{56}$, and $Au_{144}(SR)_{60}$ corresponds to the 30 kDa species in MALDI-MS (Figure 3.2a). In Figure 3.2b, 17,698 Da and 11,799 Da peaks are observed, representing 2+ and 3+ charge peaks of $Au_{144}(SR)_{60}$ which has a molecular weight of 35,397 Da. Similarly, 2+ and 3+ charge state of $Au_{137}(SR)_{56}$ peaks are observed at 16,774 Da and 11,183 Da. The 1+ charge state of $Au_{25}(SR)_{18}$, 7,034 Da is also observed in Figure 3.2b. The same synthesis protocol is repeated in another aliphatic thiol, dodecanethiol. The same three sizes are observed in dodecanethiol as shown in Figure S3.1. Figure S3.1a shows the MALDI-MS spectra of dodecanethiol protected nanoclusters synthesized using the DR method. The high laser data reveals the formation of two sizes, one around 7 kDa and a broad peak at 32 kDa. The low laser data on Figure S3.1a shows the peak of $Au_{25}(SR)_{18}$, the adjacent peak is characteristic MALDI fragmentation showing loss of $Au_4(SR)_4$. ESI-MS data on Figure S3.1b

showing a 1+ charge state of $Au_{25}(SR)_{18}$ confirms the same. The broad peak in 32 kDa of MALDI-MS has two species which is confirmed by its respective ESI-MS spectra in Figure S3.1b. The two species are $Au_{144}(SR)_{60}$ (3+ and 4+ charge state peaks marked in Figure S3.1b) and $Au_{137}(SR)_{56}$ (3+ charge state peak marked in Figure S3.1b). From the extensive research in thiolate protected nanoclusters, the linear chain aliphatic thiol makes a unique series ($Au_{25}(SR)_{18}$, $Au_{38}(SR)_{24}$, $Au_{137}(SR)_{56}$, $Au_{144}(SR)_{60}$) from the Brust method of synthesis.[15, 107-108] The same series containing $Au_{25}(SR)_{18}$, $Au_{137}(SR)_{56}$ and $Au_{144}(SR)_{60}$ is observed in this work using the DR method.

Figure S3.2 shows the optical property of the Au NMs protected by hexanethiol and dodecanethiol. The $Au_{144}(SR)_{60}$ and $Au_{137}(SR)_{54}$ do not have prominent optical features in the UV-visible region.[106, 109] But as in Figure S3.3, both spectra exhibit a small plasmonic resonance feature at ~500 nm. It indicates the presence of larger species in the plasmonic range in small amounts.

3.3.3 DR yielding Au NMs using non-linear chain thiol (TBBT). The same synthesis protocol was used but with a different thiol as a capping agent, 4-tert-butylbenzenethiol (TBBT). Unlike linear chain thiols, the sulfur atom is attached to a phenyl ring in TBBT. Additionally, it has a tertiary group attached to the para position of the phenyl ring. This gives different electronic, steric and π- π ligand interaction properties to the product NMs.[13] As a result, it gives a whole different series of gold NMs.[13-14] This series is called an aromatic series as sulfur is directly attached to the phenyl ring whereas the linear chain series is called an aliphatic series. The difference is well explained in our previous work.[13] Figure 3.3a is the MALDI-MS spectrum data of TBBT protected gold NMs, shows a peak ~62.5 kDa at low laser influence (black) corresponding to $Au_{279}(SR)_{84}$ species. High laser influence shows the same

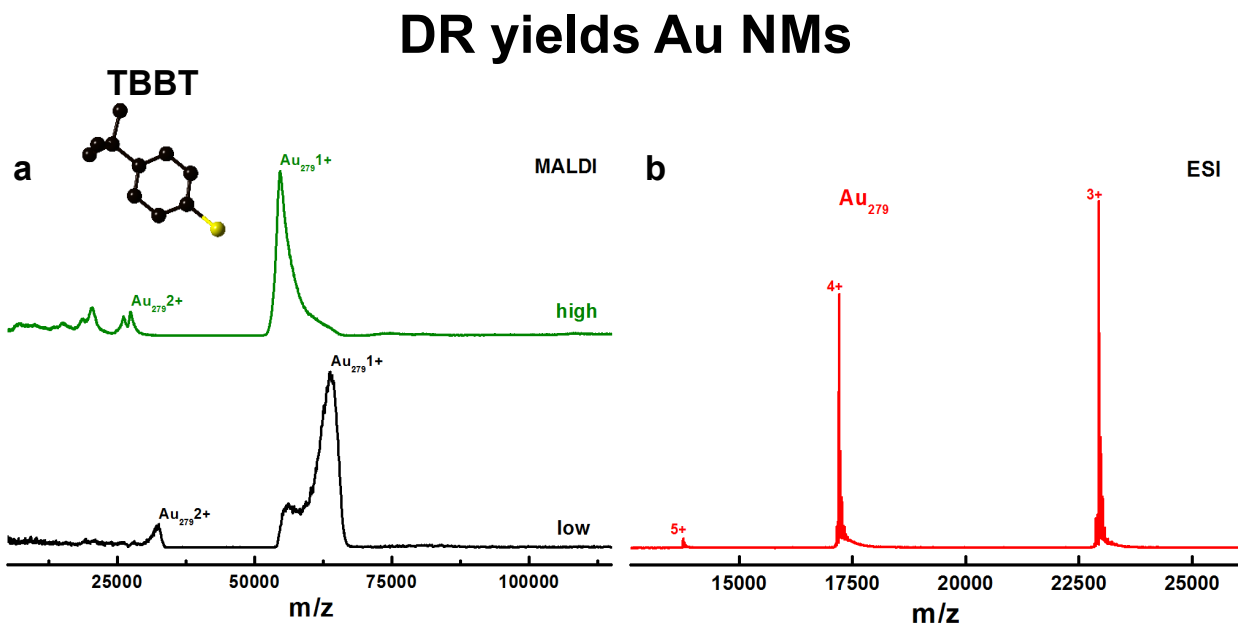

Figure 3.3. Mass spectrum confirming the repeatability of the digestive ripening yielding atomically precise gold nanomolecules with rigid secondary ligand (TBBT) where S is directly attached to phenyl ring. (a) High (green) and low (black) laser intensity MALDI-MS of the digestive ripened product. (b) ESI-MS of the digestive ripened product showing 3+, 4+ and 5+ of $Au_{279}(SR)_{84}$.

species but only gold core mass ~55 kDa, due to the removal of surface ligands. ESI spectrum in Figure 3.3b shows 3+ (22,945 Da), 4+ (17,209 Da) and 5+ (13,767 Da) of $Au_{279}(SR)_{84}$ species.

3.3.4 Isolation of pure Au NMS using Size Exclusion Chromatography (SEC). DR gives a mixture of Au NMs sizes. SEC is one of the best methods available for isolation of Au NMs based on the size.[34-35] Here, SEC is used to isolate pure Au NMs from final DR product containing mixture of sizes. The size separated and purified DR samples can then be compared with previously reported Brust method using similar purification techniques. [10-11, 33, 48, 89-91, 106, 109-110] Figure S3.3b and S3.4b shows the SEC column during the last stage of separation. Both images (Figure S3.3b and S3.4b) have two nicely separated bands, first at the bottom, a black band with 30 kDa species having majorly $Au_{144}(SR)_{60}$ and a second,

reddish brown band on the top is pure $Au_{25}(SR)_{18}$. SEC isolated MALDI-MS data of hexanethiol protected Au NMs shown in Figure S3.5a, and corresponding ESI-MS data shown in Figure S3.5b, top red spectra showing only 30 kDa peak in MALDI and 3+ peak of $Au_{144}(SR)_{60}$ and $Au_{137}(SR)_{54}$ confirms the isolation of 30 kDa species. Similarly, bottom black spectra showing $Au_{25}(SR)_{18}$ peak in MALDI-MS data and 1+ peak of $Au_{25}(SR)_{18}$ in ESI-MS data confirms the isolation of $Au_{25}(SR)_{18}$. UV-visible spectrum (Figure S3.3a, red) of the isolated $Au_{144}(SR)_{60}$ exhibits no distinctly observed peaks but minor peaks at ~510 nm and ~700 nm. It is consistent with the previously reported works and confirms the purity.[106, 110] Similarly, UV-visible spectrum of $Au_{25}(SR)_{18}$ (Figure S3.3a, black) showing well defined peaks at 400, 450, and 670 nm and slight shoulder peaks at ~575 and ~815 nm as previously reported.[51, 107-108]

Likewise, Figure S3.6 exhibits the isolation of 30 kDa and 8 kDa species of dodecanethiol protected Au NMs using MALDI-MS and ESI-MS. Figure S3.4a confirms the purity of isolation through UV-visible spectra.[106, 108, 110] These results using two different ligands (hexanethiol and dodecanethiol) confirm that DR synthesis produces atomically monodisperse nanomolecules that match with previously reported Brust synthesis.[106, 108, 110]

3.3.5 Mass Spectrometry result comparison of two methods. two-phase Brust is the commonly used synthesis method for atomically precise Au NMs. The dodecanethiol protected NMs are synthesized using Brust method as mentioned in the experiment section. The comparison of the MALDI mass spectrum between two syntheses as in Fig. S3.7 shows that they both have 2 distinct peaks at 7 and 32 kDa. Their corresponding ESI-MS data comparison shown in Figure 3.4, depicts the 3+ charge state of $Au_{144}(SR)_{60}$ (13,482 Da) and $Au_{137}(SR)_{54}$ (12,754 Da). Figure 3.4 also shows 1+ charge state of $Au_{25}(SR)_{18}$ (8,549 Da) in

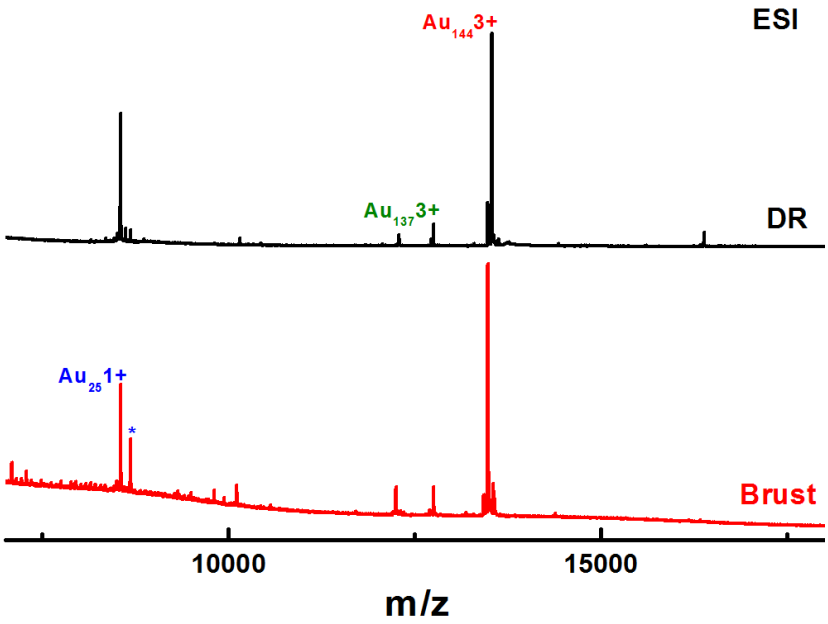

Figure 3.4. ESI Mass spectrum comparison of dodecanethiol protected atomically precise nanoparticle synthesized using Digestive Ripening (top) and Brust (bottom) method. (* is Cs^+ adduct.)

both methods. This confirms that final product in both methods have three Au NMs, namely $Au_{144}(SR)_{60}$, $Au_{137}(SR)_{54}$ and $Au_{25}(SR)_{18}$.[11, 43, 48] Therefore these results suggest that *DR and Brust leads to same product despite their pathway*. The SEC purified DR synthesis product shown in Figure S3.3 to S3.6 is consistent with the purest form of these sizes has already been reported and studied in Brust method.[10-11, 33, 48, 89-91, 106, 109-110] Various conditions with different molar ratios are used to synthesis various sizes of same thiolate protected cores. [15, 19] This forms the unique series of gold and thiolate protected NMs. The synthesis method used in this paper also gave three sizes which form a part of the unique series.[13] The recent publication of $Au_{\sim2000}(SR)_{\sim290}$ provided the largest nanoclusters using Brust method as ~3.8 nm[19] which is smaller than the normal sizes reported in the DR method.[97, 99-101]

3.3.6 The step-by-step comparison of the synthetic procedure of Brust and DR method shown in Scheme 3.1. The important difference between the two methods is

highlighted (red and blue box with arrows). Scheme 3.1 highlights the change in the color of the products inside each reaction flask.

The formation of these nanoclusters is based on a hypothesis from the Brust method,[7-8, 111-112] which was developed based on the color change at every step. Similar Brust-like synthesis in the formation of thiolate protected Ag nanocrystals is also reported.[113] In the reported hypothesis, ToABr was used as a phase transfer agent to transfer the Au^{3+} gold salt to organic phase. Here the color is reddish orange (2nd image in top of Scheme 1) representing 3+ charge state, Au^{3+}. Then the introduction of thiol reduces the 3+ charge state to 1+ forming an $Au_n(SR)_m$ complex, representing the gradual color change from reddish orange to colorless (3rd image in top of Scheme 1). Followed by reduction using sodium borohydride produced stable nanoparticles, with an Au(0) core, as indicated by the black color (Scheme 3.1 rightmost image on top), with a neutral charge state in the core Au atoms. The thermochemical treatment of this obtained crude product converts all the meta-stable products into highly stable ones. As mentioned in Scheme 1, the major change in DR from Brust is inter-changed steps between the reduction of the mixture (blue highlighted) and the addition of thiol (red highlighted). Experimental data backed up by above mass spectrometry results shows that regardless of the change in thiol addition and borohydride reduction steps, both DR and Brust synthesis give the same products. However, the DR procedure contradicts the above mentioned hypothesis as there is no involvement of thiol at the reduction step whereas the hypothesis involves formation of $Au_n(SR)_m$ polymer before reduction.

On the other hand, Tong and coworkers reported mechanistic studies on the Brust method, where they argue that even though thiol was added before reduction, Au-S bond is

not formed until the reduction step. They also argue that instead of formation of $Au_n(SR)_m$ complex, Au forms a complex with ToABr.[114-118] Meanwhile, some one-phase Brust synthesis does not include phase transfer agent in its synthesis process which could not be explained by Tong and coworkers mechanistic study.[16, 119]

3.3.7 Difference between 2 methods. As mentioned earlier, synthesis of nanoclusters using the Brust method was highly monodisperse as confirmed by mass spectrometry and single-crystal XRD, also by their optical properties.[12, 120] Whereas the DR are used only for synthesizing nanoparticles which are not atomically monodisperse (only size monodisperse).[100, 102-103] However, the above results from three different thiols confirm that through DR, atomically precision is achievable. A keen observation suggests that the precursors used in both methods are the same with one difference, DR uses didodecyldimethylammonium bromide (DDAB) as a phase transfer agent whereas the Brust method uses Tetraoctyl Ammonium Bromide (ToABr). Another difference is that the crude product was etched at 80 °C in Brust synthesis, but in DR the product was refluxed (~115 °C). Temperature is known to affect the formation of Au NMs.[121] Here, the Brust synthesis and DR are optimized to obtain the reported Au NMS. A prolonged refluxing results in decomposition of products.[121]

To eliminate the influence of ta different phase transfer agent**,** the DR method was repeated the same with a change of phase transfer agent to ToABr. The results are shown in Figure S3.9 using hexanethiol protected Au NMs. The MALDI spectrum in Figure S3.9a reveals the presence of a broad peak around 30 kDa with a small peak around 7 kDa and some high mass peaks, like the same hexanethiol protected Au NMs synthesized using DDAB shown in Figure 3.2a. The 30 kDa peaks exactly match with the MALDI spectrum in Figure

3.1a explaining the presence of $Au_{137}(SR)_{54}$ and $Au_{144}(SR)_{60}$ species, also 7 kDa species corresponding to $Au_{25}(SR)_{18}$ like Figure 3.2a. These $Au_{144}(SR)_{60}$ and $Au_{137}(SR)_{54}$ species are confirmed by ESI-MS spectra in Figure S3.9b, where 2+ and 3+ of both $Au_{144}(SR)_{60}$ and $Au_{137}(SR)_{54}$ were observed. These observations proved that the change in the phase transfer agent in DR has no impact on the formation of the Au NMs. ToABr affects a little in the relative amounts of the various sizes of Au NMs, but eventually, it leads to the formation of same Au NMs. Therefore, by keeping all chemicals same, both DR and Brust synthesis give the same products, regardless of the change in thiol addition and borohydride reduction steps.

3.4 Experimental

3.4.1 Materials. Hydrogen tetrachloroaurate(III) trihydrate ($HAuCl_4.3H_2O$) (Alfa Aesar, 99.99%), Tetraoctylammonium bromide (ToABr) (Aldrich, 98%), Didodecyldimethylammonium bromide (DDAB)(Acros, 99%), Sodium borohydride (NaBH4, 99%), 4-tert-butylbenzenethiol (TBBT)(TCI, 99%), 1-Dodecanethiol (Acros, 98%), 1-Hexanethiol (Aldrich), Cesium acetate (Acros, 99%), and trans-2-[3[(4-tertbutyl-phenyl)-2-methyl-2 propenylidene]malononitrile (DCTB matrix) (Fluka ≥ 99%). HPLC grade solvents such as tetrahydrofuran, toluene, and methanol were obtained from Fisher Scientific. All the materials were used as received.

3.4.2 Synthesis. The synthesis was done based on previous report.[100] The synthesis method comprises 2 parts. First, the didodecyldimethylammonium bromide (DDAB) (110 mg) was dissolved in toluene. Then $HAuCl_4.3H_2O$ (40 mg) was added to the above solution and transferred to a Round Bottom Flask (RBF). Typically, $HAuCl_4.3H_2O$ does not dissolve in toluene, but using DDAB as a phase transfer agent, it can be dissolved in toluene. The

solution was stirred for 15 minutes to get thorough mixing. The mixture was then reduced by $NaBH_4$ (18 mg) in water, which was indicated by the solution turning black. After 30 seconds, hexanethiol (0.43 mL) (Au:thiol = 1:30) was added rapidly, and the solution was stirred for 1 hour. The same thiol ratio maintained in reaction with other two thiols. Second, the RBF was connected to a refluxing condenser and refluxed for 18 hours. Finally, the refluxing was stopped, and the temperature was allowed to reach room temperature. The solution was rotary evaporated to remove the excess solvent. The resulting product was washed with methanol and water mixture (3-4 times) to remove excess thiol and by-products. The same method was repeated by only changing the phase transfer agent to ToABr for comparison with the Brust method.

The Brust synthesis was carried by small changes in Brust[7] two-phase synthesis. First, ToABr (0.14 g) was dissolved in toluene (7.5 ml) in an RBF. Then $HAuCl_4.3H_2O$ (0.1 g) was dissolved in distilled water (10 ml) and added to the toluene solution. The mixture was stirred for 30 minutes. The colour of the organic phase changed to bright orange, indicating phase transfer was complete. Water was discarded. The whole setup was transferred to an ice bath and stirring continued for 30 minutes. 120 µL of 1-dodecanethiol (Au: thiol = 1:2) was added and stirring continued for 30 minutes. The solution turned white. The mixture was reduced by $NaBH_4$ (0.1 mg) in 5 ml ice-cold water; immediately the colour changed to black. The solution was further stirred for 3 hours. Then the solvent was removed from the product and washed with the water-methanol mixture for 3 times, and the resulting crude product was separated. The crude product was redistributed in toluene (1 ml) with an excess amount of 1-dodecanethiol and etched at 80 °C for 2 days. The resulting product was washed with the water-methanol mixture, and the final product was obtained.

3.4.3 Instrumentation. Matrix assisted laser desorption time-of-flight (MALDI-TOF) mass spectrometry was used to acquire mass spectra with DCTB matrix on a Voyager DE PRO mass spectrometry. Compositional analysis was performed with electrospray ionization mass spectra (ESI-MS), collected from Waters Synapt HDMS using THF as the solvent.

3.5 Conclusions

In conclusion, this study reveals that digestive ripening can yield atomically precise Au NMs. The atomic precision is achieved by reducing the time difference between reduction of the mixture and addition of thiol. The consistency of this process was confirmed using three different thiols. Two aliphatic thiols give $Au_{25}(SR)_{18}$, $Au_{137}(SR)_{54}$, and $Au_{144}(SR)_{60}$, a series of Au NMs with a distinct number of gold and thiolate ligands. Structurally rigid third ligand TBBT, where the sulfur atom is directly attached to the phenyl ring, gives $Au_{279}(SR)_{84}$, an entirely different series of Au NMs. The comparison of the digestive ripening results with the Brust method infers that despite major changes in the procedure, both methods lead to the formation of Au NMs. The aliphatic and aromatic series of Au NMs identified in the Brust method is also seen in the DR method. These new findings opened a new path from the long-believed mechanism of the Brust method. This paves a way for future work on a study of the underlying mechanism for the formation of Au NMs, which should satisfy both pathways. The DR result using ToABr eliminates the influence of any difference in the chemicals and reiterates that Brust and DR yield the same Au NMs despite the difference in their pathways.

CHAPTER 4

X-RAY CRYSTAL STRUCTURE OF $Au_{36}(SPh\text{-}pCH_3)_{24}$ NANOMOLECULE AND EFFECT OF LIGANDS ON THE $Au_{36}(SR)_{24}$ STRUCTURE

Author Contributions

Senthil Kumar Eswaramoorthy and Vigneshraja Ganeshraj developed the synthetic protocol and conducted mass spectrometric analysis. Vigneshraja crystalized and solved structure. Senthil Kumar finalized the structure, conducted structure comparison, and wrote the manuscript. Amala Dass assisted in experimental design, data analysis, and edited the manuscript.

4.1 Abstract

Thiolate protected gold nanomolecules (Au NMs) are known for thier robust nature, high stability, and wide application. In Au NMs, based on ligand stereochemistry and electronics, each ligand forms a unique series with discrete sizes. 4-tert-Butylbenzenethiol (TBBT) protected Au NMs has a long well-established series notably $Au_{133}(SR)_{52}$ and $Au_{279}(SR)_{84}$ in larger size. Whereas in para-methylbenzenethiol (PMBT), $Au_{246}(SPh\text{-}pCH_3)_{80}$ and $Au_{130}(SPh\text{-}pCH_3)_{50}$ were reported with crystal structures. After the reported structure of $Au_{36}(SR)_{24}$ protected by aromatic ligands like TBBT, thiophenol, and by a non-aromatic cyclopentanethiol, it is crucial to know what forms in PMBT in the similar size range, through

which the effect of ligand in this size range can be studied? To answer the question, we report the crystal structure of $Au_{36}(SPh\text{-}pCH_3)_{24}$ NM, having 28 core Au atoms with four interpenetrating cuboctahedra in an FCC arrangement similar to previously reported $Au_{36}(SR)_{24}$ structure. The composition is independently verified using mass spectrometry, also the optical spectroscopy confirms the molecular nature. The structure is compared with three previously reported structures by overlaying all four structures on top of each other. This reveals a trend confirmed by the individual atomic bond distance comparison of same four structures.

4.2 Introduction

Au NMs are ultrasmall (<2 nm) nanoparticles with specific number of gold atoms and thiolate protected ligands.[9, 20, 122] Their unique optical and electrochemical properties leads to a vast range of applications in optics[12, 20-21], nanomedicine[22], sensors[23], gene delivery[24], therapeutics[25-26], targeted drug delivery[27-28], electro-catalysis[29] and solar cells[30]. Recent developments in high resolution mass spectrometry help in characterizing Au NMs precisely with isotopic resolution. Total structure determination of Au NMs using single crystal X-ray diffraction (ScXRD) has revolutionized the field, by providing an utmost compositional clarity and absolute three dimensional structural arrangements of metal and ligand atoms.[10-11] It also reveals that the structure has a central and/or core of Au(0) atoms with a compact geometry, surrounded by bridging thiols and monomeric (-SR-Au-SR-) and/or dimeric (-SR-Au-SR-Au-SR-) staples.[10-11]

Extensive research on thiolate protected Au NMs by various groups resulted in wide range of Au NMs protected by different thiols.[12-13-26] These Au NMs have a unique property,

showing molecular behavior in small size and transforming to metallic behavior when growing bigger. This evolution in size can be probed by their optical and electrochemical properties.[20, 110, 123] Small molecular like behavior Au NMs show a discrete electronic transition, whereas large metallic behavior exhibits optical plasmon band around 500-530 nm.[73, 110, 119, 124] The ligand steric and electronics dictate the core structure and composition of the resulting Au NMs. For instance, in aliphatic thiolated Au NMs like ultra-small $Au_{25}(SCH_2CH_2Ph)_{18}$[125] and $Au_{38}(SCH_2CH_2Ph)_{24}$[126] are the most stable species in the 1-1.4 nm size range. Whereas in bulky thiolated Au NMs, like $Au_{30}(S\text{-}tBu)_{18}$ and $Au_{30}S(S\text{-}tBu)_{18}$ comes in the similar 1-1.4 nm size range. [89-90, 119] The core size conversion between the Au NMs [37, 39, 41, 65-66] and extensive study of ligand effects points out that the bulkiness of the ligands has a major effect on the NM composition along with their capability as electron donor and π-π interaction.[13] The ligand effect become more nuanced when it comes to aromatic ligands as 4-tert-butylbenzenethiol (TBBT) and para-methylbenzenethiol (PMBT) form completely different series of Au NMs, despite their only difference being the substitution in para position. In above 100 Au atoms range, it is well-established that TBBT forms $Au_{133}(SR)_{52}$, $Au_{191}(SR)_{66}$ and $Au_{279}(SR)_{84}$ whereas PMBT forms $Au_{130}(SR)_{50}$ and $Au_{246}(SR)_{80}$, confirmed using crystal structures.[33, 84, 127-129] Also, TBBT forms $Au_{102}(SR)_{44}$ and PMBT forms $Au_{99}(SR)_{42}$, confirmed using Electrospray Ionization Mass Spectrometry (ESI-MS) near 100 Au atoms range.[38, 130]

Structure determination using SCXRD of $Au_{36}(SR)_{24}$ with 4-tert-butylbenzene thiolate revealed an intriguing core with 28 Au atom in a FCC arrangement.[40] This intriguing structure become more interesting after discovery of $Au_{36}(SC_5H_9)_{24}$ and $Au_{36}(SPh)_{24}$.[73, 131] Despite their differences the non-aromatic cyclopentane thiol (C_5H_9S), simple aromatic

thiophenol (SPh) and tert-butyl-substituted aromatic TBBT all form similar structures with 28 Au atom cores in an FCC arrangement, covered by 4 dimeric staples and 12 bridging thiols. This contrasts with the trend where the slight difference between TBBT and PMBT forms a complete different Au NM composition for sizes above 100 Au atoms. Therefore, it is important to know whether PMBT forms $Au_{36}(SR)_{24}$ or a different composition. If it forms the same $Au_{36}(SR)_{24}$ composition, how does the structure compare to the previously reported $Au_{36}(SR)_{24}$ structures? To answer these questions, we successfully synthesized, isolated, crystalized and solved the crystal structure of $Au_{36}(SPh\text{-}pCH_3)_{24}$ NM and we compared all four reported $Au_{36}(SR)_{24}$ structures, including $Au_{36}(SPh\text{-}pCH_3)_{24}$, by overlaying the four structures on top of each other and by comparing individual Au-Au bond distances of the four structures. The position of the $-CH_3$ group also plays an important role in formation of resultant compound. When the position of the $-CH_3$ group is the ortho position it forms Au_{40}(o-MBT)$_{24}$ NM.[132] The Au_{40}(o-MBT)$_{24}$ structure comprises Au_{25} kernel protected by six monomeric and three trimeric staples, which is completely different from the $Au_{36}(SR)_{24}$ NM structure. It is important to note that alloys $Au_{36-x}Cu_x$(*m*-MBT)$_{24}$[133] and $Au_{36-x}Ag_x(SPh\text{-}t\text{Bu})_{24}$ [134-135] also have similar structures to $Au_{36}(SR)_{24}$. The alkynyl protected $Au_{36}(PhC{\equiv}C)_{24}$ has FCC type Au_{28} kernel similar to $Au_{36}(SR)_{24}$ NMs, but with shorter Au-Au bond lengths.[136] Whereas the reported $Au_{36}(SCH_2Ph\text{-}t\text{Bu})_8Cl_{20}$[137] structure is entirely different comprised of Au_{14} kernel covered by a pair of pentameric ($Au_5(SCl_5)$) and hexameric ($Au_6(S_3Cl_4)$) staples. The thiolate protected $Au_{36}(SR)_{24}$ NMs have comparable optical absorption bands, whereas change in ligand, like chlorine, alkyne or selenolates, results in different optical behavior,[40, 73, 131, 136-139] showing they have different optical and HOMO-LUMO energy gaps.

Herein, we report the crystal structure of $Au_{36}(SPh\text{-}pCH_3)_{24}$. The synthesis is monitored using MALDI-MS. The final composition and purity are confirmed using MALDI-MS and ESI-MS. The distortion between four reported $Au_{36}(SR)_{24}$ structures is studied by overlaying the four structures on top of each other and by comparing individual Au-Au bond distances of the four structures.

4.4 Results and Discussion

$Au_{36}(SPh\text{-}pCH_3)_{24}$ was synthesized and purified as mentioned in experimental section in large quantities. Briefly, $HAuCl_4$ was phase transferred to toluene phase using ToABr and then reacted with PMBT thiol. After letting it react for 30 minutes, the whole mixture was reduced using $NaBH_4$ forming crude product. The crude product was then etched, and SEC-purified to attain pure $Au_{36}(SPh\text{-}pCH_3)_{24}$ NMs.

4.4.1 Mass Spectrometry. The whole synthesis process was monitored using MALDI-MS. The MALDI-MS data of the crude product (Figure S4.1a) has a broad peak explained by the presence of many meta-stable species. The etched product has mostly $Au_{36}(SPh\text{-}pCH_3)_{24}$ with some higher sizes. SEC on etched products gave good separation where visible bands are seen during elution (Figure S4.1b); the top green band corresponds to the pure $Au_{36}(SPh\text{-}pCH_3)_{24}$. Final pure $Au_{36}(SPh\text{-}pCH_3)_{24}$ composition and purity were verified by combination of MALDI-MS and ESI-MS. Figure 4.1b shows MALDI-MS with sharp peak at 9924 Da corresponding to $Au_{36}(SR)_{23}$ mass. Our previous report shows that fragmentation of $Au_{36}(SR)_{24}$ sample is inevitable in MALDI-MS and specifically it fragments to form $Au_{36}(SR)_{23}$. The next intense peak at 8644 Da corresponds to $Au_{32}(SR)_{19}$ with well-known $Au_4(SR)_4$ fragmentation. ESI-MS data shown in Figure 4.1a contains two major peaks at 10180 Da and

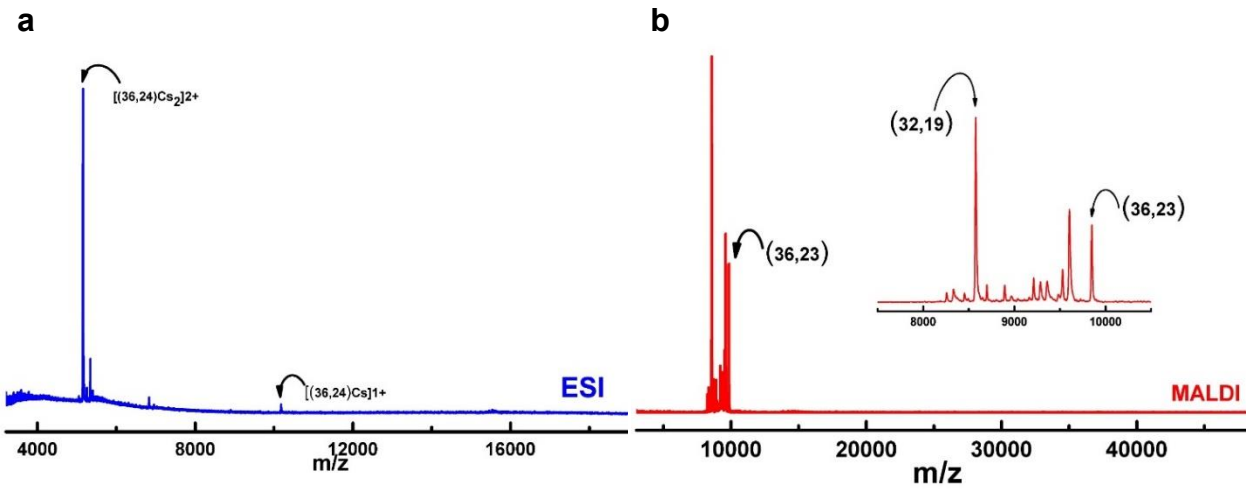

Figure 4.1. Mass spectra of isolated $Au_{36}(SPh\text{-}pCH_3)_{24}$ Nanomolecule (a) ESI-MS of the isolated pure $Au_{36}(SPh\text{-}pCH_3)_{24}$ NM showing the 1+ and 2+ of the Cs adduct peak, because $Au_{36}(SPh\text{-}pCH_3)_{24}$ NM is neutral therefore Cs is needed to enhance the ionization of the NM. (b) MALDI-MS of the same NM showing the fragmented peaks due to laser intensity.

5157 Da corresponding to 1+ with one Cs adducts and 2+ with two Cs adduct of $Au_{36}(SPh\text{-}pCH_3)_{24}$ respectively. MALDI-MS and ESI-MS reiterates the purity and composition of $Au_{36}(SPh\text{-}pCH_3)_{24}$.

4.4.2 Optical Spectroscopy. UV-visible spectra (Figure 4.2) at normal room temperature shows two distinct features at ~565 nm and ~377 nm. Low temperature UV-visible data is measured in 2-methyltetrahydrofuran solvent to find the electronic transition by reducing the rotational and vibrational energies and reveals the fine features of the absorption spectrum. In 78 K low temperature UV-visible data, the feature at ~565 nm become more prominent but contains no shifts or splits, whereas the feature at ~377 nm in room temperature splits into five distinct features at 320, 348, 377, 410 and 430 nm respectively at 78 K (Figure S4.2). The influence of the rigid Au_{28} kernel is expressed in the visible region feature (~565 nm), which shows no splitting in low temperature spectrum. In contrast, the UV region feature (~377 nm) is influenced by the more flexible third layer

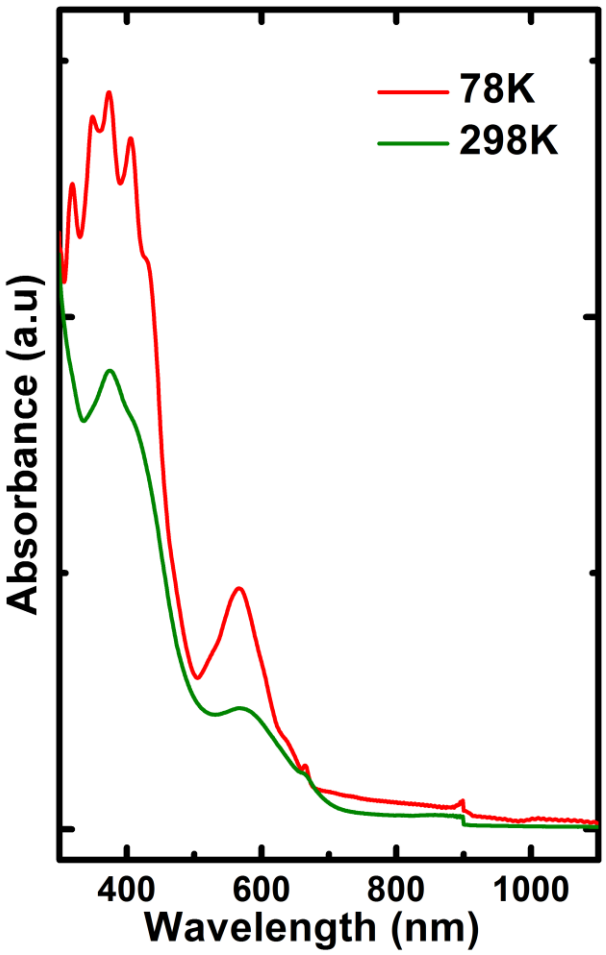

Figure 4.2. UV-visible absorption spectra of $Au_{36}(SPh\text{-}pCH_3)_{24}$.

containing dimeric staples and bridging ligands which results in five fine features by reducing its rotational and vibrational motions when reducing the temperature to 78 K.

4.4.3 Crystal structure. The $Au_{36}(SPh\text{-}pCH_3)_{24}$ crystal structure was solved in *P*-1 space group with R1=0.0818. Figure 4.3 shows the overall structure of $Au_{36}(SPh\text{-}pCH_3)_{24}$. The structure consists of four central atoms which are arranged in tetragonal fashion (Figure 4.3a), surrounded by 24 Au atoms. They combined to form an Au_{28} core in an FCC arrangement (Figure 4.3b). The 28-atom core made up of 4 interpenetrating cuboctahedra merges at four tetrahedron central atoms. Note that the four central Au atoms only have Au-Au bonds with the surrounding 24 Au atoms. This Au_{28} kernel is enclosed by 12 bridging PMBT thiolate groups. The Au_{28} kernel is also surrounded by four dimeric staples (-SR-Au-SR-Au-SR-) arranged in an orthogonal fashion (Figure 4.3c). The Au_{28} core rotated at 90 degrees horizontally (Figure S4.3 top) and vertically (Figure S4.3 bottom) shown with attached 4 dimeric staples on right side of the Figure S4.3, clearly explains the arrangement of the entire structure.

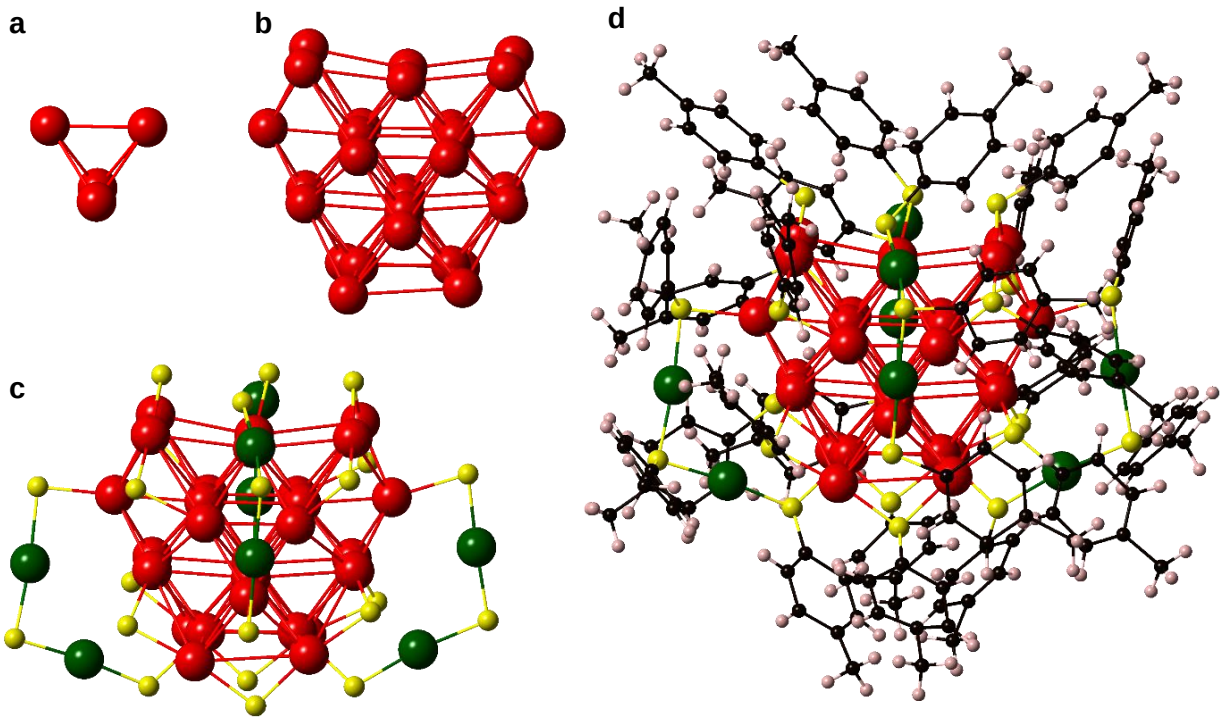

Figure 4.3. Crystal structure of $Au_{36}(SPh\text{-}pCH_3)_{24}$: (a) Au_4 tetrahedron central atoms; (b) Au_{28} truncated FCC core; (c) Core with 4 dimeric staples and 8 bridging ligands; (d) Total structure of $Au_{36}(SPh\text{-}pCH_3)_{24}$.

4.4.4 Ligand effect on $Au_{36}(SR)_{24}$ structure. Previously, three $Au_{36}(SR)_{24}$ crystal structures are reported having the same FCC type core structure with four dimeric staples.[40, 73, 131] Those other three crystal structures incorporated the ligands cyclopentane thiol (SC_5H_9), thiophenol (SPh), and TBBT(SPh-*t*Bu). Including the current $Au_{36}(SPh\text{-}pCH_3)_{24}$ crystal structure, in total four crystal structures having the same structure are known, with the only difference bringing the protecting thiolated ligands. All four crystal structures have the same type of D_{2d} symmetry with the Au_{28} core arranged in four interpenetrating cuboctahedra fashion. If we overlay all four structures together, we find that all 36 positions in all four structures do not come exactly on top of each other, in other words, do not fit perfectly. But a trend is identified in comparing these four structures. It is shown in Figure

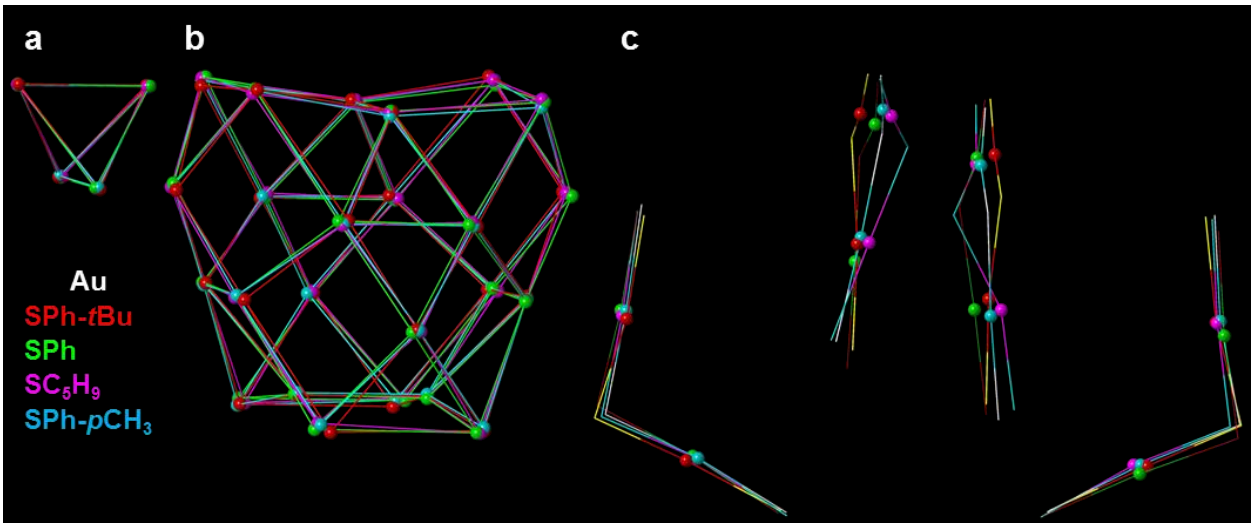

Figure 4.4. Overlay of $Au_{36}(SR)_{24}$ crystal structures protected with four different thiolated ligands (SPh-*t*Bu, SPh, SC_5H_9, SPh-*p*CH_3) showing different thiolate protected Au atoms in different color for comparison : (a) Overlay of Au_4 tetrahedron central atoms of four crystal structures which matches very well with minute difference; (b) Overlay of Au_{28} truncated FCC core without 4 central atoms where most of the positions not match well each other; (c) Overlay of dimeric staples of the all 4 crystal structures where distortions becomes more prominent.

4.4, where Au atoms of all four structures are overlayed together. The Au_4 tetrahedron central atoms (Figure 4.4a) overlay explains that the central four atoms almost come on top of each other. Then, the second shell, which has 24 Au atoms, (Figure 4.4b) overlay, showing that the perfect match in 4 central atoms cannot be extrapolated towards the second shell. The second shell shows a visible (Figure 4.4b) difference in atomic positions of all 24 Au atoms. Therefore, it is evident from Figure 4.4b that the mismatching which was not seen in central atoms clearly emerged in second shell. Note that all 24 atoms in the second shell have one Au-S bond. If we move towards the outer shell which has four dimeric staples, the differences become more prominent (Figure 4.4c) and matching becomes less. Note that the staples are only bonded to core Au atoms through sulfur.

The bond distance comparison of Au-Au and Au-S bonds of all 4 structures corroborates the trend. The individual Au-Au bond distance comparison of four central atoms (Figure S4.4a) shows that bond distance is between 2.9 and 3.0 Å, with the biggest difference being 0.1 Å. Meanwhile, Au-Au bond distance comparison of 24 core atoms (Figure S4.4b) shows that biggest bond distance difference is 0.2 Å, and the comparison of core-staple Au bond distances (Figure S4.4c) shows the biggest difference is 0.4 Å. The Au-S bond distance comparison shown in Figure S4.5 explains that the distances between Au and staple sulfur show more deviations than between Au and bridging sulfur, especially cyclopentane, which shows more deviations in some atomic positions.

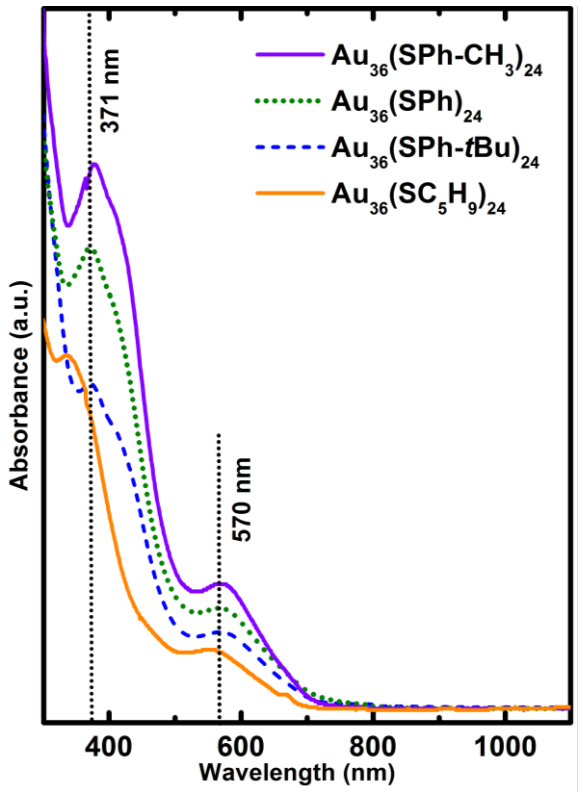

Figure 4.5. Comparison of the UV-vis-NIR absorption spectra of 4 $Au_{36}(SR)_{24}$ NMs. (SR=SPh-*p*CH_3(violet), SPh(Green), SPh-*t*Bu(Blue) and SC_5H_9 (Orange))

Therefore, it is evident that central four atoms without any Au-S have small to no distortions, followed by Au_{24} second shell, with each atom having one Au-S bond, having

some distortions and finally staple Au atoms attached to two sulfur atoms having the most distortions of all. The comparison of the optical spectra of the four $Au_{36}(SR)_{24}$ NMs shown in Figure 4.5 shows that all four NMs have 2 features, one in visible and another in UV region. There is subtle difference in the green visible region providing a feature in between ~560 to ~570 nm. This feature is influenced by the Au_{28} kernel which has little impact from ligands. The UV region peak shows small deviations between the three NMs with aromatic ligands; however, the non-aromatic *cyclopentanethiol peak blue shifts from the rest*. The peak at ~375 nm for the three aromatic NMs blue shifted 30 nm to ~345 nm in the case of cyclopentanethiol, exposing the electronic property difference that arose from the non-aromatic ring.

4.3 Experimental

4.3.1 Materials. Hydrogen tetrachloroaurate(III) ($HAuCl_4.3H_2O$), sodium boroydride ($NaBH_4$, 99%), *p*-toluene thiol (TCI America, 99%), cesium acetate (Acros, 99%), tertaoctylammonium bromide (TOABr) (Acros) and trans-2-[3[(4-tertbutyl-phenyl)-2-methyl-2-propenylidene]-malononitrile (DCTB matrix) (Fluka, ≥99%) were used. High performance liquid chromatography grade solvents such as toluene, methanol, methylene chloride (DCM), acetonitrile, 2-methyltetrahydrofuran and butylated hydroxytoluene-stabilized tetrahydrofuran (THF-BHT) were obtained from Fisher Scientific. All the materials were used as received. Biorad BioBeads S-X1 were packed in an 18-inch column and used for size exclusion chromatography (SEC).

4.3.2 Synthesis. $Au_{36}(SPh\text{-}pCH_3)_{24}$ was synthesized in three steps. It is the modified synthetic protocol of our previous report.[54] (i) Synthesis of crude mixture which gave

polydisperse mixture of nanomolecules, (ii) Thermochemical treatment of the crude mixture and (iii) Isolation and purification of the product. The mass of the crude and etched products was monitored using MALDI-MS with DCTB matrix.

Step 1: *Crude synthesis*. 0.8 mmol of $HAuCl_4.3H_2O$ was dissolved in 10 ml of H_2O and mixed with 0.9 mmol of ToABr in toluene for 15 min at 1200 rpm. Then 5 mmol of para methyl benzene thiol (PMBT) was added to the reaction mixture and allowed to react for 30 min. It formed a turbid white solution. Finally, 10 mmol of $NaBH_4$ in 4 ml of H_2O was added and reaction was continued for about 15 min which resulted in the reduction of gold with intense black color. It was then rotary evaporated to remove the solvent and a black residue was obtained. This residue was washed with methanol and water mixture multiple times (3X) to remove the excess thiol present in the crude mixture. The crude mixture was then extracted using DCM leaving the decomposed particles behind.

Step 2: *Thermochemical treatment (Etching)*. The synthesized polydisperse crude mixture was etched with excess thiol (PMBT) at 80 ˚C for 2 hours. Higher mass species underwent core size conversion to form $Au_{36}(SPh\text{-}pCH_3)_{24}$ and other stable species.

Step 3: *Purification*. The thermochemically treated product was washed with methanol to remove the excess thiol present in it. Then the product was separated using size exclusion chromatography (SEC) to obtain pure $Au_{36}(SPh\text{-}pCH_3)_{24}$.[35]

4.3.3 Crystallization and ScXRD analysis. 0.5 mg of the purified product of $Au_{36}(SPh\text{-}pCH_3)_{24}$ from SEC was taken and dissolved in 0.5 mL of toluene. Vapor Diffusion was carried out with toluene as solvent and acetonitrile as non-solvent. After ~5-7 days, crystal growth in several sites at the bottom of the vial was identified. A suitable crystal was kept at 150 K on a D8 goniostat equipped with a Bruker PHOTON-II detector in Beamline

11.3.1 at the Advanced Light Source (Lawrence Berkley National Laboratory) using synchrotron radiation tuned to λ= 0.7749A°. For data collection, 2-s frames were measured in shutterless mode at 0.5° intervals of ω. The data frames were collected using the program APEX3 and processed using the SAINT routine within APEX3. The data were corrected for absorption and beam corrections were based on the multi-scan technique as implemented in SADABS. In Olex2,[140] the structure was solved with the olex2.solve[141] structure solution program using Charge Flipping and refined with the olex2.refine[142] refinement package using Gauss-Newton minimization.

4.3.5 Instrumentation. Matrix assisted laser desorption time-of-flight (MALDI-TOF) mass spectra were acquired using DCTB matrix[44] on a Voyager DE PRO mass spectrometer. Compositional analysis was performed with electrospray ionization mass spectra (ESI-MS) collected from Waters Synapt HDMS using THF as the solvent. The UV-visible absorption spectra were measured using a Shimadzu UV-1601 spectrophotometer. Temperature-dependent UV−vis-NIR absorption measurements were collected with an UV−visible−NIR Cary 5000 and JANIS VNF100 low-temperature cryostat using 2-methyltetrahydrofuran as the solvent, and a Lakeshore Cyotronics temperature controller was used for temperature-dependent absorption measurements

4.5 Conclusions

In summary, we have synthesized and isolated stable $Au_{36}(SPh\text{-}pCH_3)_{24}$ and its crystal structure is revealed using single crystal X-ray crystallography. Similar to previously reported $Au_{36}(SR)_{24}$ structures, $Au_{36}(SPh\text{-}pCH_3)_{24}$ has FCC type Au_{28} core structure with four dimeric staples. The composition of the NM is confirmed using ESI-MS and MALDI-MS. In

addition to known features at ~565 and ~377 nm, low temperature UV-visible spectroscopy brings out five fine features in the UV range. The overlay of crystal structures and comparison of individual atomic Au-Au and Au-S bond distances of the known four $Au_{36}(SR)_{24}$ NMs, reveals that mismatching is minimum at the center of the and increases while moving to the surface.

CHAPTER 5

ATOMICALLY PRECISE PALLADIUM NANOCLUSTERS WITH 21 AND 38 PALLADIUM ATOMS PROTECTED BY PHENYL ETHANE THIOL

Author Contributions

Senthil Kumar Eswaramoorthy developed the synthetic protocol, conducted mass spectrometric and UV-visible absorption measurements, and wrote the manuscript. Amala Dass assisted in experimental design and data analysis and edited the manuscript. Both authors made substantial, direct, and intellectual contribution to the work in the manuscript preparation and discussion.

5.1 Abstract

Monolayer thiolate protected nanoclusters (MPCs) are extensively studied due to their distinctive properties. The achievement of atomic precision in MPCs, especially in gold MPCs through mass spectrometry, leads to detailed and accurate study of thier properties. The total structure determination through ScXRD of gold and silver MPCs revolutionized the field by providing structural arrangement in atomic level. Synthesizing MPCs with other metals like palladium (Pd) to study and compare properties is tedious and complex. In one

end, larger size monodisperse Pd nanoparticles (NPs) were synthesized and studied for various catalytic properties. Meanwhile, on the other end, a small molecule tiara-like Pd-thiolate complex was reported. But the atomic precise Pd MPCs in the middle and their detailed studies are not yet explored. Here, we report synthesis and identification of atomically precise phenylethanethiol protected $Pd_{21}(SCH_2CH_2Ph)_{18}$ and $Pd_{38}(SCH_2CH_2Ph)_{21}S_2$ Pd nanoclusters. The size distribution is confirmed using MALDI-MS, and ESI-MS confirms the composition through isotopically resolved peaks. X-ray photoelectron spectroscopy (XPS) spectra elucidate the cluster formation.

5.2 Introduction

Monolayer thiolate protected nanoclusters (MPCs) composed of metal cores with sizes ranging from tens to thousands of atoms have been extensively studied in recent years due to their distinguishing optical, electronic, and catalytic properties.[20, 122-123] In thiolate protected metal nanoclusters atomic precision is achieved through thermochemical etching especially in gold nanoclusters.[8-9, 20, 143] These ultra-small metal nanoclusters have distinct properties compared to larger nanoparticles due to quantum size effects which lead to a wide range of applications in catalysis, sensing, energy and solar cells.[30, 144-147]

In early stages, high resolution electron microscopy (HREM) was used to study gold nanoparticles (Au NPs), but smaller clusters suffered from beam damage. However, the introduction of mass spectrometry in characterizing Au NPs changed the course of the field. In the beginning, Laser Desorption Ionization Mass Spectrometry (LDI-MS) combined with HREM elucidated the discovery of quantitatively separable gold nanocrystals.[8-9, 20, 123, 143, 148-150] Then, Matrix Assisted LDI-MS with time of flight (MALDI-TOF-MS) gave better mass

spectra with minimal fragmentation.[151-153] Later by choosing the suitable matrix and by using threshold laser intensity, fragment free molecular peaks were achieved in MALDI-MS.[48]

The introduction of electrospray ionization mass spectrometry (ESI-MS)[154-155] on MPCs results in ionization of intact cores with no fragmentation.[156] Especially for gold MPCs, the soft ionization technique ESI-MS, provided the MPC compositions with atomic precision.[43] Initially, atomic composition of various glutathione-protected gold clusters was determined using ESI-MS by Tsukuda and co-workers.[49-52] Then highly popular $Au_{25}(SC_2H_4Ph)_{18}$ was determined with the help of polyethylene glycol (PEG) by the Murray group.[156] Finally, isotopically resolved ESI-MS of the same $Au_{25}(SC_2H_4Ph)_{18}$ cluster exactly matched the simulated spectra, confirming the atomic precision beyond any doubt.[43] Later, the total structure of $Au_{25}(SC_2H_4Ph)_{18,}$ determined using single crystal X-ray diffraction (ScXRD) provided the exact number of gold atoms and thiolate ligands, as previously determined using ESI-MS.[11]

In noble metal MPCs, gold MPCs were the most studied and well-established systems, followed by silver MPCs. [157-163] Recently, a few studies on copper MPCs were reported.[164-165] The study of other metals, particularly with thiolate protected clusters, is minimal. Palladium (Pd) metal is known for its high catalytic activity in both homogeneous and heterogeneous catalysis.[166-167] The 2010 Noble Prize in chemistry awarded for Pd catalyzed cross couplings in organic synthesis, shows the importance of Pd in catalysis.[168] The Suzuki coupling, one of the coupling reactions for which The Noble Prize was awarded, uses Pd salts or organopalladium complexes. Meanwhile, 11-mercaptoundecanoic acid-covered Pd NPs can be reused for several times for the same Suzuki coupling reaction.[169]

Lawrence F. Dahl and Evgueni G. Mednikov explored in detail the formation of Pd nanoclusters with carbonyl/phosphine ligands ($Pd_n(CO)_x(PR_3)_y$).[170-171] There are about 19 distinct Pd core geometries, having core Pd atoms ranging from 10 to 165, that have been isolated and their total structures were determined using ScXRD. The Pd forms a highly condensed carbonyl/phosphine ligand nanocluster that exhibits unprecedented geometrical diversity of icosahedral or closed cubic/ hexagonal closed packing-based metal core geometries. The largest cluster has a platinum centered four shell 165 atom Pd-Pt cluster [$(\mu_{12}\text{-Pt})Pd_{164-x}Pt_x(CO)_{72}(PPh_3)_{20}$ ($x \sim 7$)] protected by 72 carbonyl and 20 phosphine ligands with pseudo icosahedron geometry.[171] It is important to note that these Pd nanoclusters are only stable in inert conditions. While the relatively weak metal-metal and metal-CO bonds lead to a large number of $Pd_n(CO)_x(PR_3)_y$ clusters with structural diversity,[170] the weaker bonds result in unstable compounds and are therefore not well studied when compared with thiolated Au nanoclusters.

On the other hand, Pd nanoparticles protected by thiolated ligands form a good candidate for various catalysis. The thiolate protected Pd NPs showed excellent catalytic activity in the Heck reaction.[168] In a study of catalytic hydrogenation, an n-alkanethiol self-assembled monolayer (SAM) coating on Pd surface improved the selectivity of 1-epoxybutane formation from 1-epoxy-3-butene from 11 to 94%.[172]

An understanding of thiolate protected Pd NPs is needed to explore more important features. But it has a prerequisite, a correct description of chemical composition and surface structural arrangement of these Pd NPs. In one end, Pd NPs characterized using Transmission Electron Microscopy (TEM) were reported. The TEM data provided only size distribution, where 1 nm difference is equal to difference of atoms in hundreds. In the other

end, tiara-like Pd complexes with formula ($Pd_n(SR)_{2n}$) where n= 2 to 20, were reported with atomic precision, and some were reported with ScXRD structures. But these are not Pd nanoclusters having metal core and surface ligands. Various water and organic soluble small Pd NPs have been studied like Rongchao Jin et al.'s work on $Pd_{13-17}(SR)_{18-22}$ (R=Ph-tBu),[173] Martin M.F. Choi and collaborators' work on a series of water soluble N-acetyl-L-cysteine protected ultrasmall Pd NPs,[174] and Tatsuya Tsukuda et al.'s work on a range of $Pd_n(SR)_m$ clusters ($5 \leq n \leq 60$) with $m \sim 0.6n$,[175] reported using MALDI-MS characterization.[173-175] However, due to its hard ionization, MALDI-MS could only provide an approximate composition of metal atoms and protecting ligands.[151-153, 173-175] Therefore, to fulfill the prerequisite and eventually allow the tweaking of the properties of thiolate protected Pd NPs, atomically precise Pd MPCs need to be synthesized and identified first. ESI-MS is one of the main tools to identify the atomic precision which leads to the determination of chemical composition.

In this work, we report atomically precise palladium nanoclusters with 21 and 38 Pd atoms protected by phenylethanethiol confirmed using isotopically resolved ESI-MS. MALDI-MS confirms their size distribution and UV-visible spectra confirm their molecular nature.

5.3 Results and Discussion

The Pd nanoclusters are synthesized using modified method of two phase Brust synthesis.[7] The step by step synthesis process is explained in the experimental section.

5.3.1 Mass spectrometry. In general, the identification of nanoclusters (NCs) other than Au NCs with mass spectrometry is a challenge. However, building on the experience gained by our group to obtain mass spectrometry data on difficult larger Au NCs, we were

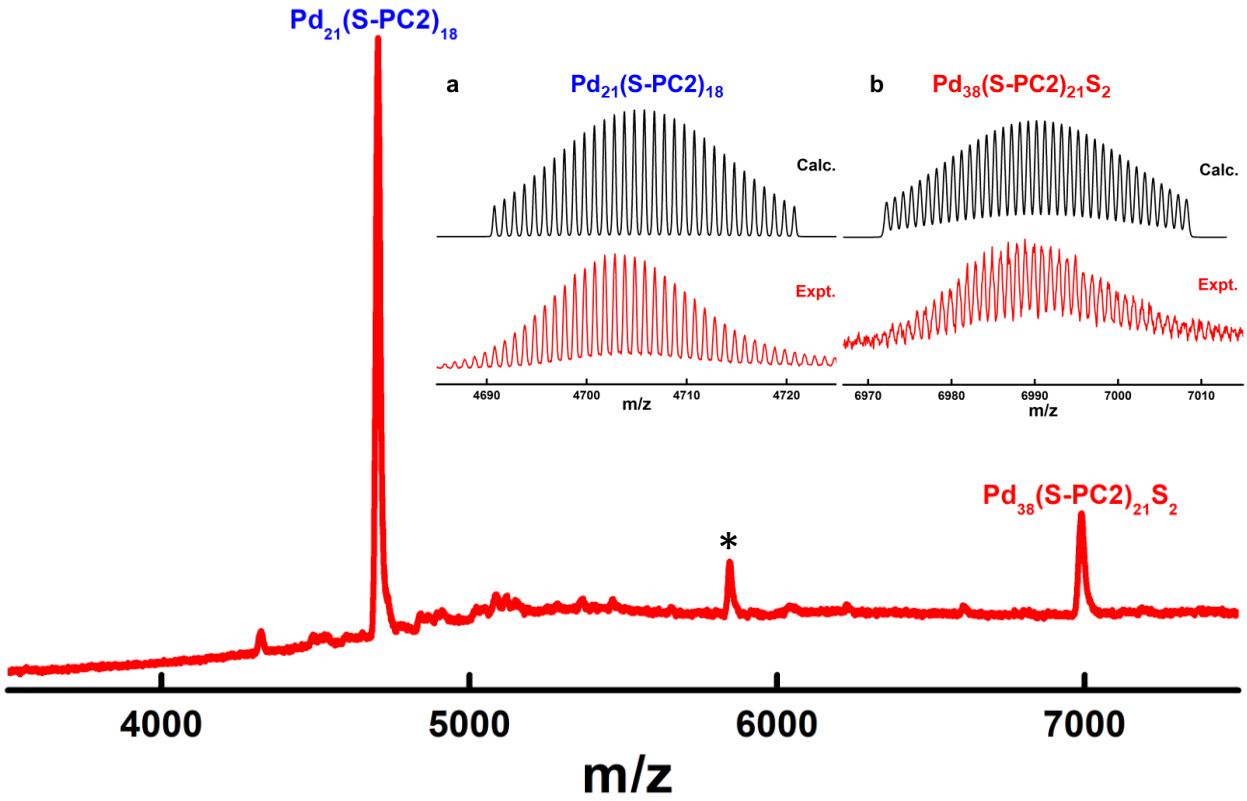

Figure 5.1. Electrospray Ionization Mass spectra (ESI-MS) of Size Exclusion Chromatography (SEC) purified product of Pd nanoclusters protected by phenylethanethiol (PC2) showing 2 products, $Pd_{21}(SR)_{18}$ and $Pd_{38}(SR)_{21}S_2$. * Represents less intense peak at 5844 Da.

able to obtain ESI-MS data of the atomically precise Pd NCs shown in Figure 5.1. As mentioned in the experimental section, the first part of synthesis provides crude product which was then reacted with excess thiol at elevated temperature to obtain etched product with narrow size distribution. The etched product was purified using size exclusion chromatography (SEC).

Figure 5.2 shows the MALDI-MS spectra of selected SEC fractions. A photograph of the SEC column is shown on the right in Figure 5.2. The SEC column has two major bands, yellow and dark bands. Fraction 8 (F08) represents the yellow band and fraction 4 (F04) represents the dark band. Their corresponding MALDI-MS spectra in positive mode is shown

on the left side. The top spectrum corresponding to the yellow band shows many sharp peaks below 5 kDa. The sharp peaks represent the atomic precision of the NCs, in other words, these NCs are precise enough to ionize and show up in ESI-MS. MALDI-MS is a hard ionization technique. The sample is bombarded with laser to ablate the sample and get the spectra. So, the NCs tend to fragment in MALDI-MS, which corresponds to the multiple peaks in the top spectra. In comparison, ESI-MS is a soft ionization technique which is more important to identify the molecular mass of the NCs. The bottom spectrum corresponds to the dark bank showing a broad peak from 4 to 14 kDa. Since this is a broad beak with less mass precise, this dark band is not ionizing in the ESI-MS.

The ESI-MS in positive mode of SEC-purified product as shown in Figure 5.1, has two major peaks, which are identified as 4700 Da and 6989 Da. An expanded view of these two peaks is shown in Figure 5.1(inset). The NCs are formed with a metal core that is protected by thiolate ligands. These NCs have a precise number of metal and ligand count, Pd_xSR_y where x and y represent the number of Pd atoms and ligands respectively in the NC. In some cases, sulfur atoms alone can bond with the metal core without a ligand chain and can be denoted as $Pd_xSR_yS_z$.[90] The NC at 4700 Da is identified as $Pd_{21}(SCH_2CH_2Ph)_{18}$ and 6989 Da is identified as $Pd_{38}(SCH_2CH_2Ph)_{21}S_2$. Figure 5.1 (inset) shows an expanded view of the major peaks revealing the isotopic distribution of these two NCs. The bottom spectrum of Figure 5.1a is an expanded view of Figure 5.1 at 4700 Da range to show the isotopic distribution of NC. The isotopomer splitting showing (Figure 5.1a & 5.1b) mass differences of 1 Da suggests that these peaks correspond to the 1+ charge state of the respective Pd NCs. The top spectrum of Figure 5.1a is a calculated spectrum of $Pd_{21}(SCH_2CH_2Ph)_{18}$ with isotopically resolved peaks. The exact match between the experimental and theoretical spectra confirms

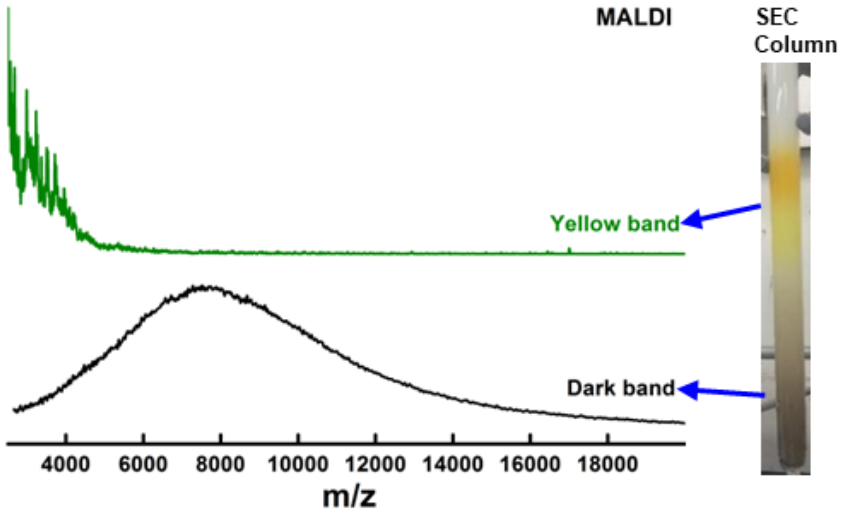

Figure 5.2. Matrix assisted Laser Desorption Ionization Mass spectra (MALDI-MS) of Size Exclusion Chromatography (SEC) products, in that, the top spectra correspond to the yellow band which has low mass products. The bottom spectra come from the dark band which has high mass products compared to the yellow band.

the composition, that the NC has 21 Pd atoms protected by 18 thiolate ligands. Likewise, in Figure 5.1b, the top spectrum is a calculated spectrum of $Pd_{38}(SCH_2CH_2Ph)_{21}S_2$ and the bottom spectrum is an expanded view of Figure 5.1 at 6989 Da range. The isotopic matching of theoretical and experimental spectra confirms the assigned chemical composition. The less intense peak at 5844 Da is not isotopically resolved to exactly assign the peak. The closest match of the 5844 Da peak is $Pd_{34}(SCH_2CH_2Ph)_{16}S$. Previously reported studies on thiolate protected larger Pd NCs and thiolate Self Assembled Monolayer (SAM) on 2D Pd surface suggest that the formation of a Pd-S interlayer between the core and thiolate ligands adds stability.[176-178]

5.3.2 Optical Spectroscopy. The UV-visible spectrum, Figure 5.3 corresponds to the final SEC purified yellow band product. The inset of Figure 5.3 shows the photograph of the SEC purified yellow band sample in toluene. The UV-visible spectrum rises from ~600 nm and shows two distinct features, ~414 and ~322 nm. These two features are close to the

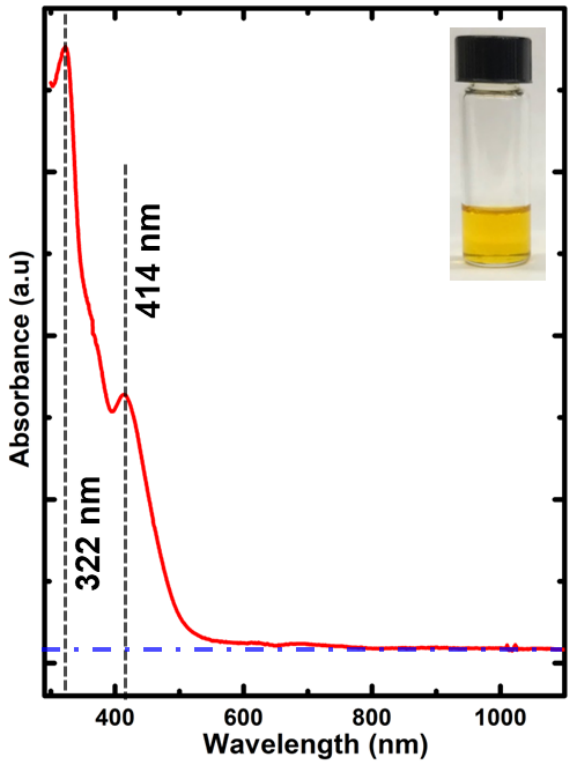

Figure 5.3. Ultraviolet and visible (UV-visible) spectra of Size Exclusion Chromatography (SEC) purified product of Pd nanoclusters protected by Phenyl ethanethiol (PC2) in toluene. Blue dash-dot line represents the baseline.

reported $Pd_6(SC_{12}H_{25})_{12}$ complex.[174, 179-180] The ESI-MS comparison of fractions 8, 9 and 10 (Figure S5.1) shows that most of the smaller complexes eluted in the latter fractions (F09 & F10) and a minute amount remains in fraction 8. In the seminal work of Negishi et al., on 1 nm Pd clusters, similar optical spectra were reported.[175] Though they observed features of the $Pd_6(SR)_{12}$ complex, based on several factors they ascribe that a significant portion of the spectrum was contributed by $Pd_n(SR)_m$ clusters. Similarly, based on the ESI-MS data (Figure S5.1), XPS data (Figure 5.4, S5.2 & S5.3) and SEC separation technique, we can ascribe that a significant portion of our spectrum is from the Pd NCs.[175]

5.3.3 X-ray Photoelectron Spectrum. The full survey X-ray Photoelectron Spectrum (XPS) of SEC purified Pd NCs (yellow band) with the main core level lines is presented in Figure 5.4. Here, spectral features corresponding to palladium (Pd), sulfur (S), and carbon (C) are detected. The XPS spectrum is calibrated using C 1s photoemission at 285 eV. XPS features of all elements of the clusters with their photoelectron shell identification are shown in Figure 5.4 and their high-resolution core-level spectra are shown in Figure S5.2. The high-resolution Pd core-level photoemission spectra (Figure 5.4(inset)) show two peaks: 342.6

and 337.3 eV, which have been assigned as Pd $3d_{3/2}$ and Pd $3d_{5/2}$ from Pd clusters. The Pd $3d_{5/2}$ peak position at 337.3 eV is located between Pd metal (335.1 eV) and Pd(II) in $PdCl_2$ (338 eV).[181-183] The observation of these features for these clusters is qualitatively interpreted based on XPS studies on gold nanoclusters.[50, 184-186] In these studies a monotonic

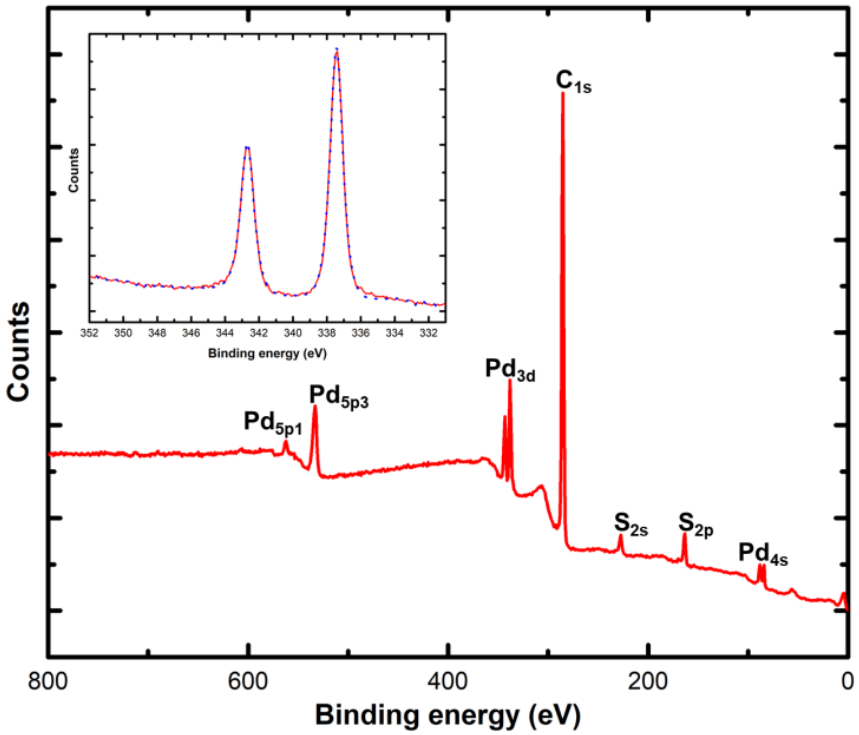

Figure 5.4. X-ray photoelectron spectroscopy (XPS) spectrum of SEC purified product of Pd nanoclusters protected by Phenyl ethanethiol. Inset, high-resolution spectrum focused on Pd 3d

shift of a Au($4f_{7/2}$) peak is observed due to two components: "final state effect" arising from inner Au core atoms and "initial state effect" arising from surface Au atoms.[50, 184-188] Similarly, these two components could contribute to the shift of Pd($3d_{5/2}$ and $3d_{3/2}$) peaks for the Pd NCs reported here. Due to the smaller sizes of these Pd NCs, the shift could most probably be influenced by the "initial state effect". The comparison of Pd 3d core level spectra of dark and yellow bands (Figure S5.3) shows similar binding energy, which further confirms the the presence of monotonic shift in thiolate protected Pd NCs. Another important observation is

the absence of satellite peaks. The good match of the observed spectra with preliminary data fitting (blue dotted line in Figure 5.4(inset)) and the absence of satellite peaks eliminates the possibility of other charge states of Pd being present in the sample.[181-182, 189-190]

5.4 Experimental

5.3.1 Materials. Palladium (II) Chloride 99.9% (metal basis) Pd 59.0% (Alfa Aesar), tetra-n-octylammonium bromide (ToABr, Acros, 99%), Hydrochloric Acid (ACS grade) (VWR), Sodium borohydride (Acros, 99%), phenylethanemercaptan, (Sigma-Aldrich), and trans-2-[3[(4-tertbutyl- phenyl)-2-methyl-2-propenylidene]malononitrile (DCTB matrix) (Fluka≥99%) were used as received. HPLC grade solvents such as tetrahydrofuran, toluene, methanol, butylated hydroxytoluene stabilized tetrahydrofuran (THF-BHT) and acetonitrile were obtained from Fisher Scientific. Bio-Rad-SX1 beads (BioRad) were used for size exclusion chromatography.

5.3.2 Synthesis. The Pd nanoclusters were synthesized based on a modified synthetic protocol reported in literature.[7, 191] In this procedure, first, a crude product was synthesized based on Brust two phase synthesis.[7] Then the crude product was thermochemically treated with elevated temperature and finally the pure product was isolated using Size Exclusion Chromatography (SEC).[35]

Crude Synthesis: Palladium chloride ($PdCl_2$) (0.1 g) was dissolved in 0.366 mL of concentrated hydrochloric acid and 1.5 mL of H_2O. ToABr (0.47 g) was dissolved in 5 mL of toluene separately. They are both mixed in a 100 mL round bottom flask under stirring at 500 rpm. The mixture was allowed to stir for 15 min. When phase transfer was completed, the organic layer was separated and 57 mL of phenylethanethiol (PC2) (Pd: Thiol = 1:0.75)

was added. Then the reaction between gold and thiol was allowed to proceed for 1 hour with the same stirring rate. At this point, the reaction was reduced by rapidly adding 0.2 g $NaBH_4$ (Pd: $NaBH_4$ = 1:10) dissolved in 5 mL of ice-cold water. The solution changed to black color indicating the formation of nanoclusters. The stirring was continued for about 18 hours. Then, the resulting products in the organic phase was separated, and rotary evaporated to remove excess solvent. Finally, the product was washed with excess methanol-water mixture to obtain the crude product.

Etching and SEC: The washed crude product ~130 mg, was thermochemically treated (etched) at 70 °C with 2.5 mL of toluene and 2.5 mL of excess PC2 thiol for 24 hours. The etched product was rotary evaporated and washed with methanol and water mixture to remove all the byproducts. The final step was to isolate the different sizes of the product using SEC. When the etched product was passed through the SEC column, two differentiable bands (yellow and dark) were seen. These two bands represent two completely different products with a significant mass difference. The reported Pd nanoclusters were obtained from the yellow band.

5.3.3 Instrumentation. MALDI mass spectra were acquired using Voyager-De PRO MALDI-time of flight mass spectrometry using DCTB[48] matrix. ESI mass spectra were collected using Waters Synapt XS instrument, with tetrahydrofuran as solvent. UV–visible absorption spectra were collected using a Shimadzu UV-1601 instrument, and samples were dissolved in toluene.

5.5 Conclusions

In summary, we demonstrated the two phase Brust synthesis can be utilized to synthesize atomically precise Pd NCs. The composition of new Pd NCs is $Pd_{21}(SCH_2CH_2Ph)_{18}$ and $Pd_{38}(SCH_2CH_2Ph)_{21}S_2$. These compositions are unequivocally confirmed by isotopically resolved ESI-MS. The size distribution is confirmed using MALDI-MS. The XPS spectrum corroborates the cluster formation and the size of these Pd NCs.

CHAPTER 6
SIZE EXCLUSION CHROMATOGRAPHY: EFFECT OF COLUMN LENGTH

Part of the text and figures in this chapter are reprinted (adapted) with permission from: Sakthivel, N. A.; Jupally, V. R.; Eswaramoorthy, S. K.; Wijesinghe, K. H.; Nimmala, P. R.; Kumara, C.; Rambukwella, M.; Jones, T.; Dass, A., Size Exclusion Chromatography: An Indispensable Tool for the Isolation of Monodisperse Gold Nanomolecules. Anal. Chem.* ***2021,* *93 (8), 3987-3996; Copyright 2021, American Chemical Society.*

Author Contributions

Senthil Kumar Eswaramoorthy and Hirunika Wijesinghe developed the synthetic protocol, conducted mass spectrometric and UV-visible absorption measurements and wrote the column effect part of the manuscript. Amala Dass assisted in experimental design, data analysis, and edited the manuscript.

6.1 Abstract

Atomically precise gold nanomolecules (Au NMs) are needed in high purity to understand their properties clearly and to develop applications using them. Unfortunately, we observe polydisperse product with a mixture of core-sizes in any synthetic path. Therefore, the product requires post synthetic separation techniques to obtain pure Au NMs. Methods like solvent extraction and Liquid Chromatography have their limitations. Size exclusion chromatography (SEC) is a versatile and indispensable tool used for separating nanomolecules and nanoparticles. Our group has used SEC for more than past 5 years and demonstrated the importance of SEC during the course of research by various group

members.Here, my work focuses on expanding that research and studying the effect of column length in SEC using *tert*-butylthiol protected Au NMs.

6.2 Introduction

Gold nanomolecules (Au NMs also known as nanocrystals, nanoclusters) are atomically precise ultra-small thiolate protected gold nanoparticles.[9-11, 55, 192] Au NM preparation involves a two-step protocol. The first step involves preparation of a crude product following a two-phase (Brust-Schiffrin) method[193] or a single phase method (using THF/methanol as the solvent). The crude product is polydisperse in nature, consisting of a mixture of sizes. The second step involves thermochemical treatment of the product at an elevated temperature in presence of an excess amount of ligand. The thermochemical treatment is also referred to etching.[8] The etching step results in a product with narrowed size distribution, where the products are atomically precise and thermodynamically stable. The availability of such precise compounds[54] has enabled us to understand the structure and property evolution in the ultrasmall size range of 1 to 3 nm.[128] The research interest in Au NMs is growing exponentially due to their high stability[54], unique optical[20, 83, 147] and electronic properties[20, 123, 143, 192, 194-198] with potential applications in biomedicine, catalysis, etc.[199-201]

To understand their fundamental properties, highly pure Au NMs need to be isolated from the mixture. Therefore, the use of separation techniques becomes unavoidable. Separation techniques such as solvent fractionation[54, 202], high pressure liquid chromatography (HPLC)[82, 203-208], size exclusion chromatography (SEC)[34, 109, 209-212] and preparative thin layer chromatography (PTLC)[213] have been widely employed in isolating

pure Au NMs. Whetten et al. employed solvent fractionation for isolating organosoluble Au NMs in their seminal work.[9] The HPLC of organosoluble thiolate capped Au NMs has been explored widely.[82, 203-208] The separation takes place based on varying intermolecular interaction between the analyte and the stationary phase. [82, 203-207] However, it is challenging to process tens of milligrams of the product using HPLC. The PTLC[213] technique has also been used to isolate Au NMs. In the case of PTLC, a significant amount of human interaction is involved with spotting the sample, plate development and then recovering each separated species from the plate (by scrapping and further processing). In some cases, column chromatography (CC) has also been employed (using alumina or silica beads) in the separation of AuNMs.[123, 214] Gel electrophoresis (and various chromatographic methods) have also been used in the case of water soluble thiolate ligand protected (Au and Ag) nanomolecules.[215-218]

SEC was originally developed for separations of proteins, lipids, fatty acids, lipophilic polymers and polycyclic aromatic compounds.[219-221] The separation by SEC is based on the hydrodynamic volume (size) of the nanomolecules.[34] The smaller sized compounds travel through the pores in the beads and take a longer path to elute. The larger sizes take a shorter path and elute faster through the larger pores or spaces between the beads. Thus, the larger nanomolecules elute first and the smaller nanomolecules elute later. In literature, majority of the work employing SEC for separation of nanomolecules (or nanoparticles) has used HPLC instruments with a commercial SEC column and different types of detectors.[209-212] The use of sophisticated instruments severely limits the quantity of product that can be separated per run. Our group has demonstrated the versatility and indispensable nature of the gravity flow SEC technique to isolate the organosoluble thiolate ligand capped Au NMs

Table 6.1. SEC column parameters

	Long	Medium	Short
Column length (cm)	199.4	149.9	60.9
Expanded bed Length (cm)	196.8	138.4	54.6
Bed length (cm)	180.3	130.8	50.8
Inner diameter (cm)	2.64	2.64	2
Outer diameter (cm)	3.2	3.2	2.54
Tip OD (cm)	1.04	1	1
Tip Length (cm)	~5	~5	~6.4
Frit to tip length (cm)	~11.4	~11.4	~11.4
Flow Rate (ml/min)	0.65	1.05	1.3
Optimum loading mass (mg)	50-100	35-40	15-20
Elution time (hours)	~16-18	~4-6	~1-1.5
Beads	Bio-Rad SX-1 Support		

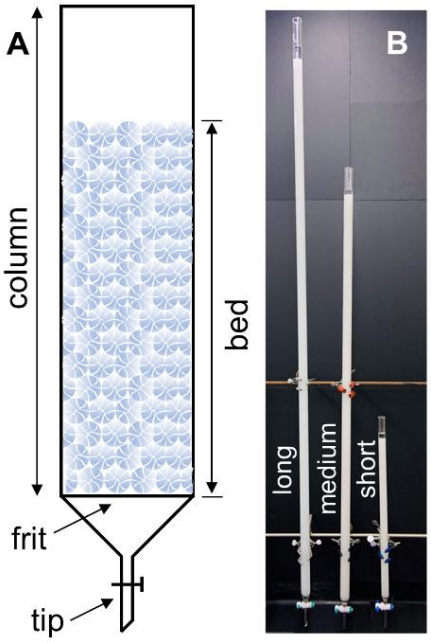

The column dimensions are shown in (A), and three column images are shown in (B).

and elucidated the following: the control and ease of separation offered by SEC compared to solvent fractionation, separation of a wide range of sizes (a crude nanoparticle mixture ranging from ~5 to ~200 kDa), separation of closely sized Au NMs ($Au_{137}(SR)_{56}$ from a mixture of $Au_{329}(SR)_{84}$, $Au_{144}(SR)_{60}$, $Au_{137}(SR)_{56}$ and $Au_{130}(SR)_{50}$), and separation of Au NMs protected by different ligands (phenylethanethiolate, thiophenolate, 4-*tert*-butylbenzenethiolate, tert-butyl thiolate).[35] In continuation, this work focuses on the effect of column length in SEC using *tert*-butylthiol protected Au NMs.

6.4 Results & Discussion

SEC can be used for separation of various ligand products in a various size range. The pure NM is obtained by doing multiple SEC cycles. After completion of the first SEC, the fractions having similar sized Au NMs based on MALDI data are combined, and a second SEC

was done. Likewise, the process is repeated until final pure product was obtained. The number of SEC cycles is based on the input mixture and its size composition. We use 3 sizes of column based on their length (short, medium, and long) for our SEC. The parameters of the column are given in Table 6.1. The loading mass for the column was determined by column size. The interaction of mobile phase (sample solution) with stationary phase (beads) is high for smaller size of NMs as they go through the beads and take longer paths; meanwhile, larger size particles have less interaction and take shorter path around the beads. As a result, the larger sizes elute first, followed by next size, and smaller ones elute last. The resolution of separation should increase as the length of the column increases, because the sample mixture interacts with increased volume of beads.

To illustrate the separation of Au NMs based on their mass in different sized columns, we have used a mixture of $Au_{30}(S\text{-}tBu)_{18}$ (7514 Da), $Au_{46}(S\text{-}tBu)_{24}$ (11200 Da) and $Au_{65}(S\text{-}tBu)_{29}$ (15389 Da) as the loading sample (herein after denoted as Au_{30}, Au_{46} and Au_{65}, respectively). This mixture was synthesized following the published literature.[16] SEC was done in short and medium length columns using THF stabilized with BHT, as eluent. In the short column, 19 mg of the sample mixture, dissolved in 300 µL THF stabilized with BHT, was loaded as a thin band. The valve was completely open and mobile phase was allowed to flow in gravity without any external pressure. The obtained flow rate for the short column was 1.3 mL/min. Figure S6.1 clearly shows the separation of the species when it flows through the column. The left most photo was taken just after loading the column, which shows a thin loaded layer in the start. As we move towards right in Figure S6.1, the band expands as the Au NMs separate when flowing through the column. The right most photo (57-min), right before fraction collection, shows the maximum expanded band for the short

column. It shows a green color band at the top followed by dark brown color band at the middle and ending with light brown color. The final light brown color is the diluted color of the middle dark color band. The first fraction was collected 57 minutes after loading the

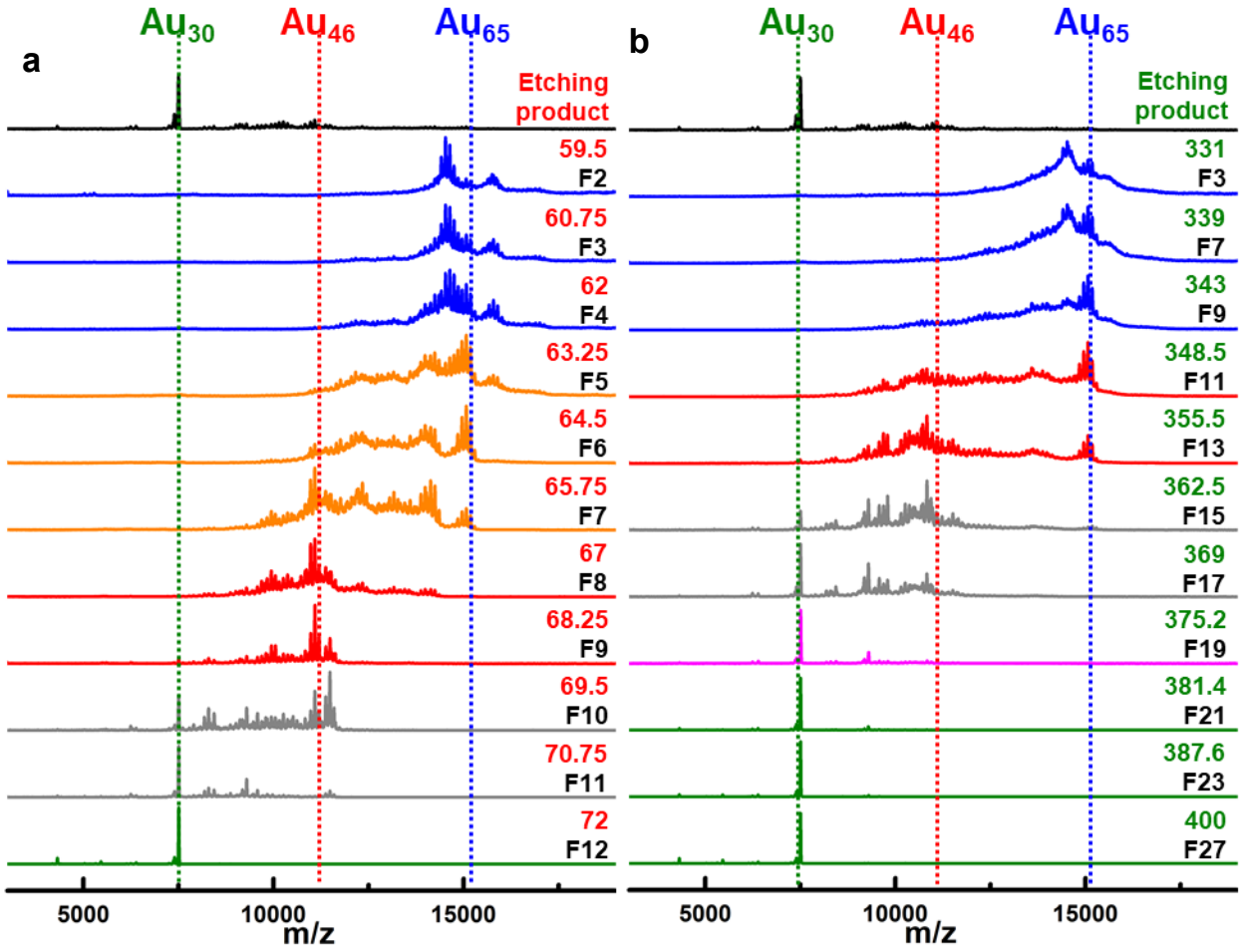

Figure 6.1. SEC of *tert*-butyl thiolate protected Au NMs etched product containing $Au_{30}(SR)_{18}$ (7514 Da), $Au_{46}(SR)_{24}$ (11200 Da) and $Au_{65}(SR)_{29}$ (15389 Da). MALDI-MS showing different fractions collected during SEC using (a) short and (b) medium columns with elution time in minutes and fraction numbers.

sample. In total 12 fractions were collected. Each fraction was collected for 75 seconds (~1.62 mL of eluted sample) and named as F1, F2 etc.

For the medium column, 25 mg of sample was dissolved in 500 µL THF stabilized with BHT and loaded as mentioned before. In medium column, fully open gravity flow gave 1.05

mL/min flowrate. The Figure S6.2 is a pictorial display of the separation of Au NMs species through the medium column. Similar to Figure S6.1, the left most photo is taken just after loading the column. As we move towards right the interaction time of the sample increases along with its flow through the column. The elution time of the medium column increased to ~5.5 hour which is 5.5 times more than the short column (~1 hour) and length of medium column is ~2.5 times longer than sort column. The longer column length with increasing interactions between mobile and stationary phase results in more expansion of the bands in the medium column during elution. As seen in Figure S6.2 the band expands slowly in the first 1.5 to 2 hour of elution. Then it expands well towards 3 hour and continues to expand up to end at 5.5 hour. In the medium column it took 330 minutes to elute the first fraction. The final right most photo at 330 minute shows the completely expanded band. As per the colored band, the medium column shows 2 bands, green and dark brown, similar to short column. But the band is well expanded in medium column. It almost separated two bands with very little mixing whereas the short column had more mixing of bands. Altogether, 27 fractions were collected. Fractions 1-10 were collected for 120 seconds each (~2.1 mL), fractions 11-10 were collected for 210 seconds each (~3.68 mL) and fractions 16-27 were collected for 190 seconds each (3.32 mL).

The collected fractions from the SEC of short and medium columns were analyzed by MALDI-MS, and shown in Figure 6.1 (for the clarity, the spectra of odd numbered fractions of medium column are plotted). The etched product shows the presences of Au_{30} with a high intense peak and Au_{46} and Au_{65} peaks minorly. In the short column fractions, F2-4 has Au_{65}, F5-6 has both Au_{65} and Au_{46}, F7-8 has both Au_{46} and Au_{30} and F9-12 has Au_{30}. A fraction with major or pure Au_{46} was not obtained in the short column. In the medium column F5-11 has

Au_{65}, F13-15 have Au_{65} and Au_{46}, F17-19 has Au_{46}, F21-23 have Au_{46} and Au_{30} and F25-27 has Au_{30}. The elution time for the first fraction going from short column to medium column, increased from 57 min to 330 min. Unlike the short column, we were able to get fractions containing Au_{46} as a major species using the medium column. The increase in length of the column improves the resolution, where the entire elution window from first fraction to the last is 12 min for short column and 70 min for the medium column. The green colored Au_{30} NM elutes last and could be visually distinguished to be collected as a pure fraction. Pure Au_{46} and Au_{65} could also be obtained by repeating a few SEC cycles using fractions having same size distribution.

6.3 Experimental

6.3.1 Materials. Hydrogen tetrachloroaurate(III) ($HAuCl_4 .3H_2O$) (Alfa Aesar, ACS grade), Tetraoctylammonium bromide (Sigma-Aldrich, 98%), Sodium borohydride (Acros, 99%), thiophenol (Acros, 99%), *tert*-butylthiol (Sigma-Aldrich, 99%), anhydrous ethyl alcohol (Acros, 99.5%) and trans-2-[3[(4-tertbutylphenyl)-2-methyl-2-propenylidene] malononitrile (DCTB matrix) (Fluka ≥99%) were purchased from Aldrich. HPLC grade solvents such as tetrahydrofuran, toluene, methanol, THF-BHT and acetonitrile were obtained from Fisher Scientific. Bio-Beads S-X1 support resin (styrene divinylbenzene beads, mesh size – 200-400, cross-linkage - 1%, bead size – 40–80 μm, exclusion range – 600–14,000 Da) was obtained from Bio-Rad Laboratories.

6.3.2 Synthesis. *tert*-Butylthiolate protected Au NMs were prepared following the reported protocols.[16]

6.3.3 Instrumentation. Matrix assisted laser desorption time-of-flight (MALDI-TOF) mass spectra were acquired using DCTB matrix[44] on a Voyager DE PRO mass spectrometer. Compositional analysis was performed with electrospray ionization mass spectra (ESI-MS) collected from Waters Synapt HDMS using THF as the solvent.

6.3.4 Size exclusion chromatography. Normally, three different lengths were used in our research. They are named short (~61 cm), medium (~150 cm) and long (~200 cm) based on their length (Table 6.1. In this work, short and medium column is used to show the column effect. First, the beads were soaked with THF-BHT for at least 6 hrs, preferably overnight. The beads expand in volume during this time. After sufficient soaking, the slurry of swollen beads was then packed in the column. The columns for SEC were ordered from Chemglass, teflon stopcock, coarse fritted disc, and beaded top. The slurry was slowly loaded through the top side of the column with the stopcock open and excess solvent to avoid any air bubbles. The excess THF elutes out as the beads settle and pack in the column. The column was packed with beads until the final level of the bed was ~4 inches from the top. Once the beads are completely packed, the stopcock was closed. It is important to make sure that the column never runs out of solvent to avoid drying of the beads.

Sample preparation. Polydisperse product to be separated was dissolved in THF - BHT and centrifuged at 4000 rpm for 3 to 4 min to precipitate any insoluble material. Supernatant was separated, dried, and weighed for loading on the SEC columns.

Loading and elution. The SEC bed expands in volume when it is idle. Therefore, the solvent above the bed level was eluted until the bed reached a constant height. The bed surface was made flat by stirring it with a glass rod/pipette during this process. After the settled bed was flat and constant in height, the solvent above the bed was eluted to the level

of the bed. The dissolved sample was taken in a 9" pasteur pipette and loaded carefully (drop by drop), spreading it across the surface as a thin disk (layer). The loading step is crucial for good separation. Then fresh mobile phase was added to allow the loaded sample to enter the bed. The solvent was added evenly on the surface of the thin band drop by drop using a pasteur pipette in circular motion. The shape of the band was maintained flat by adding the solvent uniformly. Elution time varies significantly based on the size of the AuNM and the column dimension. Elution times listed in Table 6.1 were the representative time recorded from elution of various products (different size range, ligands, and composition). The stopcock was closed after all the product was eluted. Fractions collected from SEC were then analyzed by mass spectrometry to determine the composition. The fractions were washed with excess methanol after rotary evaporation to remove the residual BHT for storage or crystallization of the desired product.

6.5 Conclusions

SEC was known to separate Au NMS better than any other technique in large quantity with large size range. In this work, when the mixture of Au_{30}, Au_{46}, and Au_{65} eluted through short and the medium columns, the Au_{30} and Au_{65} pure products were isolated in both short and medium columns. However, the isolation of Au_{46} from Au_{30} and Au_{65} was obtained only in medium column. In summary, the resolution of separation can be improved by increasing the column length.

CHAPTER 7
LIGAND EFFECT OF PARA SUBSTITUTED AROMATIC THIOLATED LIGANDS AND FUTURE DIRECTIONS

7.1 Abstract

Since the discovery of the Brust synthesis, atomically precise Au NMs have been envisioned as the gateway to the manipulation of matter.[222] Instead, we have found a more complex system at the molecular level than ever imagined from bulk metal. There is a significant dependence in the self-assembly process of gold NMs, based on the capping ligand. To harness this power of manipulation over matter at the atomic level, we must first understand the ligand dependency phenomenon. Core size conversion is one of the best methods to study those ligand dependency by skipping lot of steps included in the Brust synthesis. In this work, the ligand effect of para substituted aromatic thiols was investigated using the core size conversion method on $Au_{144}(SR)_{60}$ Au NMs. The same method can be used on various sizes in the future to better understand the ligand effects on Au NMs.

7.2 Introduction

The size, shape and structure of a material determines its properties in any scale. When the size of the material reaches nanometer scale, it shows an extraordinary property change from the bulk.[85-86] Understanding these properties in nanometer scale needs various characterization techniques which can analyze this material at the atomic level. Gold

nanoparticles (Au NPs) are a rigid material which enable us to probe their properties in atomic level. Among Au NPs, thiolate protected Au NPs are a great candidate due to the vast interest in understanding from the last two decades of reported works, starting from the pioneering work by Faraday on gold colloids, followed by Brust synthesis method,[7] inclusion of mass spectrometry and thermochemical treatment by Whetten et al.,[8-9] and total structure determination by Kornberg et al., and Murray et al.[10-11]

Thiolate protected gold nanoparticles (Au NPs) research expanded substantially after the introduction of the two phase method by Brust et al.[7] Various modifications on this method have been made since to form Au NPs with varying sizes and ligands. [12-16] In thiolate protected Au NPs, atomic precision can be achieved in smaller than 3 nm size particles. These atomically precise Au NPs have distinct numbers of gold atoms and thiolate ligands, which are also known as gold nanomolecules (Au NMs). One phase Brust synthesis method was later developed using polar or slightly polar organic solvents.[16] The one and two phase Brust synthesis methods commonly result in polydisperse products. Therefore, these crude products are thermochemically treated to convert all meta-stable sizes into stable Au NMs, but thermochemically treated products needed further purification to achieve pure Au NMs. Achieving pure Au NMs is comparatively easy using a few protecting ligands, whereas it becomes quite tedious while using certain other ligands.[34, 106, 210, 223] It was envisioned that after achieving atomically precise Au NMs, we could manipulate the matter and tweak the structure at the molecular level. Instead, we came to know that the system is more complex, and the resulting size significantly depends on the self-assembly of gold atoms and thiolate ligands. Here, the gold metal remains constant while the differing protecting ligand dictates the self-assembly and final composition of the resulting compound. Therefore, each ligand

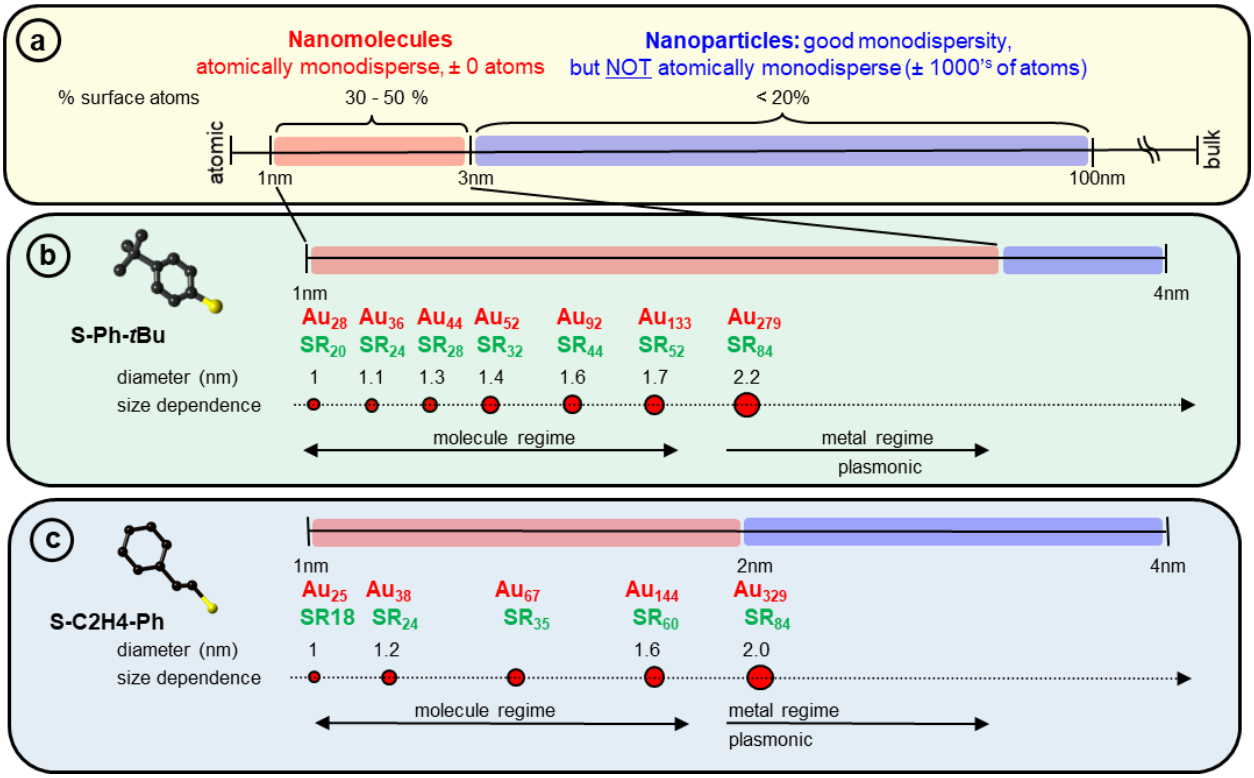

Figure 7.1. Thiolate protected series of Au NMs reported to date in two widely used systems. (a) 1-100 nm size range with 1-3 nm containing nanomolecules (±0 atoms) and 3-100 nm containing nanoparticles where size dispersity has been achieved but still variation of ±1000 atoms exists. (b) TBBT series and (c) phenylethanethiolate series of Au NMs.

forms a unique series with discrete number of gold atoms and thiolate ligands. The two well established series ware from phenylethanethiol (PC2) and 4-*tert*-butylbenzenethiol (TBBT). The reported Au NMs from PC2 and TBBT series are shown in Figure 7.1. The literature study based on ultra-small Au NMs (<1.5 nm) categorized them into 3 main classes, namely aliphatic, aromatic, and bulky series. But recent developments with several resolved crystal structures with various thiols contradicts this general categorization.[14, 33, 40, 63, 127-129] However, the ligand dictation of final composition and structure of Au NMs is still unquestioned. Understanding this ligand dictation will allow nanomolecular chemists to gain higher level of precision and control in developing and understanding new nanomaterials.

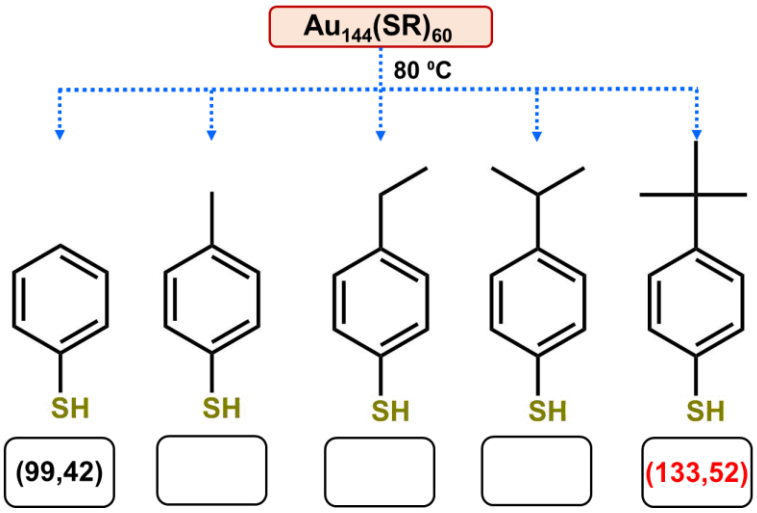

Scheme 7.1. Core size conversion reaction of $Au_{144}(SR)_{60}$ reacted with para substituted aromatic thiolated ligands. The transformation with thiophenol results in $Au_{99}(SR)_{42}$ whereas transformation with TBBT results in $Au_{133}(SR)_{52}$. The remaining transformation will be made in the proposed works.

Core size conversion: The two or one phase Brust synthesis forms a series of Au NMs based on the ligands. Separation of those species is tedious in most of the cases. One of the alternative synthetic ways is ligand exchange. Ligand exchange is a conversion method in which a pure Au NM is treated with an incoming ligand with elevated temperature.[224] If the incoming ligand has similar steric and electronic property as the original ligand, the incoming ligand replaces the original ligand while maintaining the original core size. If the incoming ligand has different steric and electronic properties, replacement of the original ligand with incoming ligand makes the gold core unstable and converts it to the nearby stable size. The second conversion is known as core size conversion or transformation.[13, 39, 65-67, 225] The core size conversion can be monitored using mass spectrometry and UV-visible spectroscopy. Core size conversion can also be used to convert easily attainable pure Au NM in one ligand to a difficult to isolate Au NM in a different ligand of comparable size. .[13, 39, 65-67, 225] Core size conversion became interesting after the report of $Au_{38}(SR)_{24}$ to $Au_{36}(SR)_{24}$ and $Au_{144}(SR)_{60}$ to $Au_{133}(SR)_{60}$.[37-38] Due to its higher stability and well-established nature, the transformation from PC2 series to TBBT series was inevitable. The highest number of

transformations were reported between these 2 series, which are $Au_{25}(SR)_{18}$ to $Au_{28}(SR)_{20}$, $Au_{38}(SR)_{24}$ to $Au_{36}(SR)_{24}$, $Au_{144}(SR)_{60}$ to $Au_{133}(SR)_{60}$ and finally the work discussed in chapter 2, $Au_{329}(SR)_{84}$ to $Au_{279}(SR)_{84}$.[39-42] This covers the majority of the reported Au NMs in both series (Figure 7.1). In the case of transforming $Au_{38}(SR)_{24}$, it is predictable that aromatic ligands like thiophenol and TBBT form $Au_{36}(SR)_{24}$, but $Au_{38}(SR)_{24}$ transformation with cyclopentanethiol forming $Au_{36}(SR)_{24}$ was not expected.[131] The effect of ligands on these transformation was discussed in a 2015 perspective.[64] This perspective lays out three layers of ligand effects: (1) bulkiness in the α-carbon; (2) bulkiness in the isomeric methylbenzenethiol; and (3) bulkiness in the para-position of the benzenethiol.[64] However, a few other reported works, like the interconversion between $Au_{30}(SR)_{18}$ and $Au_{38}(SR)_{24}$, tend to disagree with this generalization.[65] The authors do state in the perspective that further analysis is required of why a particular ligand behaves in a certain way. My proposal is to extend the transformation study with new commercially available thiols with different substitution on the phenyl ring and get better understanding of the ligand effects.

7.2.4 Proposed Work and Hypothesis. Remarkably robust Au_{144} protected by PC2 and hexanethiol becomes reactive when reacted with aromatic thiols. But this reactivity differs based on the substitution in the phenyl ring. $Au_{144}(SR)_{60}$ core converts to $Au_{99}(SR)_{42}$ when reacted with thiophenol whereas it core size converts to $Au_{133}(SR)_{52}$ when reacted with 4-*tert*-butylbenzenethiol (TBBT) (Scheme 7.1). On the other hand, core conversion of $Au_{38}(SR)_{24}$ forms $Au_{36}(SR)_{24}$ using both TBBT and thiophenol. The only difference between the two thiols is the substitution in the para position: TBBT has *tert*-butyl group whereas thiophenol has no substitution. It was also reported that simple substitution like F, CH_3 or OCH_3 on the para position also leads to transformation from $Au_{144}(SR)_{60}$ to $Au_{99}(SR)_{42}$. But

methyl substituted benzene thiol (*p*MBT) forms robust $Au_{130}(SR)_{50}$ using direct Brust synthesis method where the total structure was determined using ScXRD.[127] Therefore, hypothetically, *p*MBT should transform to $Au_{130}(SR)_{50}$. In order to understand the effect of substitution of the phenyl ring on core size conversion I propose the following works.

7.2.5 Objectives We will study the ligand effects by employing core size conversion of $Au_{144}(SR)_{60}$ with three aromatic thiols, where the para position is substituted with methyl, ethyl, and iso-propyl groups respectively. We know from the previously reported works that $Au_{144}(SR)_{60}$ transforms to $Au_{133}(SR)_{52}$ with TBBT and $Au_{99}(SR)_{42}$ with thiophenol. Therefore, studying the core conversion of these three thiols will close the loop from no substitution to bulky *tert*-butyl substitution (Scheme 7.1) and help us understand the effects of substituents on the para position of the phenyl ring on the gold core formation. $Au_{144}(SCH_2CH_2Ph)_{60}$ will be synthesized using two phase Brust synthesis method and isolated using SEC. Then, the core size conversion with the other three ligands will be monitored using mass spectrometry. Since there were no prominent UV-visible features in this size range, UV-visible monitoring of core size conversion is not needed.

7.3 Experimental

7.3.1 Materials. Tetrachloroauric (III) acid ($HAuCl_4{\cdot}3H_2O$,>99% metal basis, Aldrich), Sodium borohydride ($NaBH_4$, 99%), 4-tert-butylbenzenethiol (TCI, 99%), phenylethylmercaptan, (Sigma-Aldrich), cesium acetate (Acros, 99%), anhydrous ethyl alcohol (Acros, 99.5%), isopropylbenzenethiol (Acros, 99%), *p*-toluenethiol (TCI America, 99%), ethylbenzenethiol (Acros, 99%), and trans-2-[3[(4-tertbutyl-phenyl)-2-methyl-2-propenylidene] malononitrile (DCTB matrix) (Fluka≥99%) were purchased and used as

received. HPLC grade solvents such as tetrahydrofuran, toluene, methanol, butylated hydroxytoluene stabilized tetrahydrofuran and acetonitrile were obtained from Fisher Scientific.

7.3.2 Synthesis. The synthesis of $Au_{144}(SCH_2CH_2Ph)_{60}$ was done in two steps following the previous report.[226] The first step is the synthesis of crude products and the second step is the thermochemical treatment followed by size exclusion chromatography to get the pure $Au_{144}(SCH_2CH_2Ph)_{60}$.

***Crude synthesis*:** $HAuCl_4.3H_2O$ (0.177 g) was dissolved in 5 mL of distilled water. In a 250 mL round bottom flask, 0.284 mg of TOABr was dissolved in 10 mL of toluene. Then $HAuCl_4$ solution was added to the 250 mL round bottom flask under 1200 rpm of stirring. $HAuCl_4$ was phase transferred from water to toluene and it is indicated by the color change of the organic layer from colorless to orange. The solution was allowed to stir for 30 min. After all the Au salt transfer into the organic layer, it was separated from the aqueous layer and dipped in an ice bath for another 30 min. Then phenylethyl thiol was added (Au: thiol = 1:3) to the solution and stirred 1 h at 1200 rpm. The orange color of the solution changed to a white color indicating the formation of -Au-SR-Au- polymer [55]. Then 0.171 g of $NaBH_4$ dissolved in 5 mL of ice-cold water was added rapidly to the reaction mixture. The solution turned to a black color indicating the formation of nanomolecules. The reaction was allowed to stir for 18 hours after the $NaBH_4$ was added to the solution. It was then rotatory evaporated to remove excess solvent, washed with methanol and water to remove byproducts, and finally, the crude product was extracted in toluene.

***Thermochemical treatment*:** The crude product was dissolved in toluene and etched in excess phenylethyl thiol at 80 °C with stirring at 600 rpm for 22 h. After that, the excess

solvent was rotatory evaporated, and washed with methanol and water to remove byproducts. Pure $Au_{144}(SCH_2CH_2Ph)_{60}$ was isolated by size exclusion chromatography.

The synthesis of $Au_{144}(SC_6H_{13})_{60}$ with hexanethiol was done using slight modification from the digestive ripening synthesis reported in chapter 2.[223]

Core size conversion: Once-purified $Au_{144}(SR)_{60}$ was etched at 80 °C in excess amounts of each incoming thiol in the ratio mg of $Au_{144}(SR)_{60}$ to 100 µL of incoming ligand. The reaction was monitored between 24-48 hours to observe the effects taking place on the NMs. The incoming ligands used include: *p*-ethylbenzenethiol (SPh-Et), *p*-isopropylbenzene thiol (SPh-iPr), *p*-methylbenzenethiol, *p*-methylbenzenethiol (PMBT), and *tert*-butylbenzene thiol (TBBT).

7.3.3 Instrumentation. Matrix assisted laser desorption time-of-flight (MALDI-TOF) mass spectra was acquired using DCTB matrix[44] on a Voyager DE PRO mass spectrometer. Compositional analysis was performed with electrospray ionization mass spectra (ESI-MS) collected from Waters Synapt HDMS using THF as the solvent.

7.4 Results and Discussion

$Au_{144}(SCH_2CH_2Ph)_{60}$ was synthesized following previously reported method. The detailed synthesis procedure is given in the experimental section.[226] The SEC purified product was first verified using MALDI-MS and ESI-MS. Then the ligand induced core size conversion process was done using elevated temperature with excess thiol. In previously reported process, $Au_{144}(SCH_2CH_2Ph)_{60}$ converts to $Au_{133}(SPh\text{-}tBu)_{52}$ within 5 hours.[39] The same reaction condition was repeated, and its ESI-MS results are shown in Figure S7.1. In these ESI-MS spectra, the core conversion starts in 2 hours with a major peak at Au_{133}(SPh-

*t*Bu)$_{52}$. In 6 hours, the reaction was completed and $Au_{144}(SCH_2CH_2Ph)_{60}$ completely core converts to Au_{133}(SPh-*t*Bu)$_{52}$. However, the reaction was continued non-stop up to 24 hours to examine the stability of prolonged etching. After etching for 24 hours, the product Au_{133}(SPh-*t*Bu)$_{52}$ was stable without any decomposition (Figure S7.1). However, when we increase the temperature to 140 ^{o}C, the core converts to higher sizes reported by our group.[227]

7.4.1 Ligand effect of isopropyl group

Next, $Au_{144}(SCH_2CH_2Ph)_{60}$ reacted with isopropylbenzenethiol at elevated temperature to study the ligand effect of the isopropyl group. Figure 7.2 show the MALDI-MS spectra of the samples collected at each time interval during the reaction. The MALDI-MS clearly shows that the $Au_{144}(SCH_2CH_2Ph)_{60}$ at 33 kDa core converts first to Au_{130}(SPh-*i*Pr)$_{50}$ upon etching, with excess thiol and eventually completely converts to $Au_{99\text{-}102}$(SPh-*i*Pr)$_{42\text{-}44}$ upon continuous etching leading to complete core conversion. Evidently, at the start (0 H), the only Au NMs species present was $Au_{144}(SCH_2CH_2Ph)_{60,}$ which was confirmed by MALDI-MS at 33 kDa (Figure 7.2 (0 H)). After 3 h, the core size conversion had started and $Au_{144}(SCH_2CH_2Ph)_{60}$ converted into 32 k Da (Au_{130}(SPh-*i*Pr)$_{50}$). As the reaction proceeds and after 6 h, the peak was still centered on 32 kDa but the spectrum was broad and elongated on the low mass region, which shows the beginning of core conversion from 32 kDa towards smaller sizes. At 12 hours, the core has completely converted to 32 kDa (Au_{130}(SPh-*i*Pr)$_{50}$), but simultaneously a new peak at 25 kDa ($Au_{99\text{-}102}$(SPh-*i*Pr)$_{42\text{-}44}$) arises. When the reaction proceeds towards 24 hours the 32 kDa peak decreases and the 25 kDa peak become more prominent, affirming that $Au_{99\text{-}102}$(SPh-*i*Pr)$_{42\text{-}44}$ was formed at the expense of Au_{130}(SPh-*i*Pr)$_{50}$. Continuous etching up to 48 hours completely converted the core to the 25 kDa ($Au_{99\text{-}}$

$_{102}$(SPh-*i*Pr)$_{42\text{-}44}$) species.

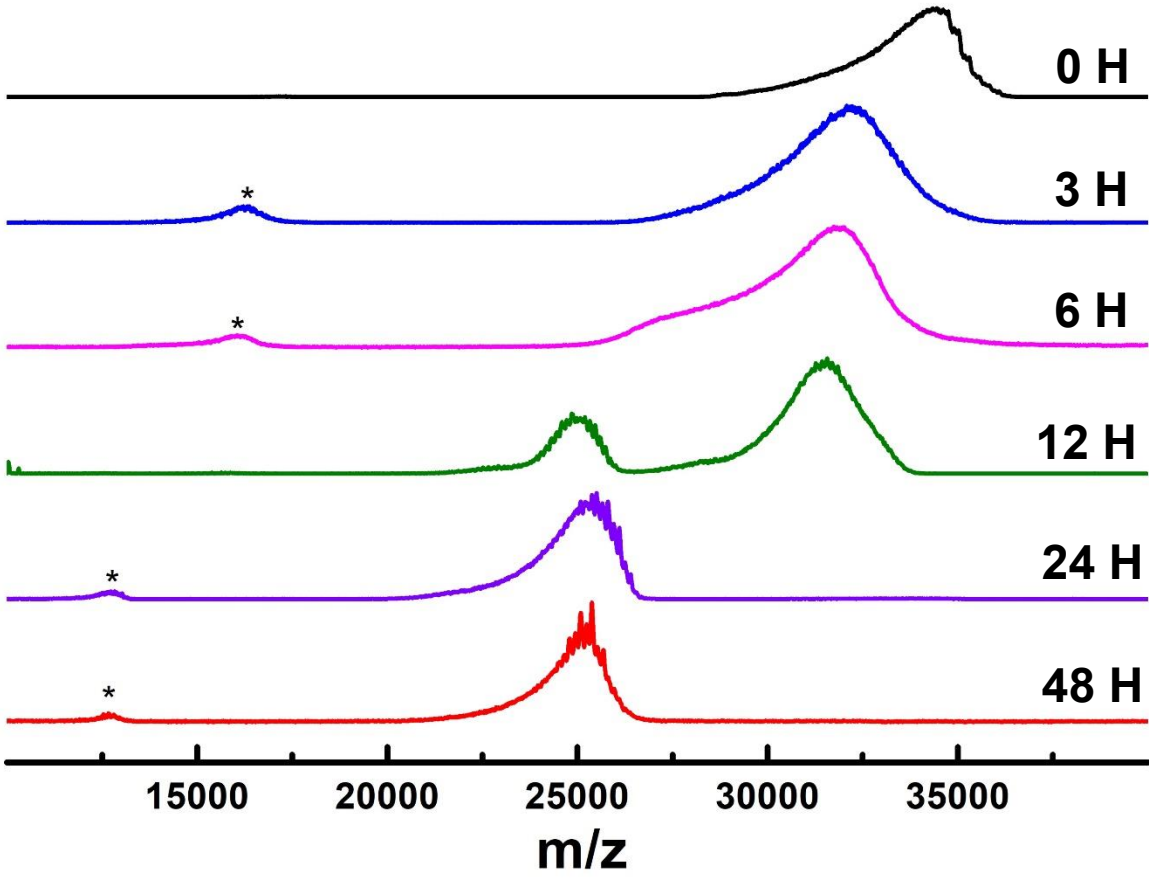

Figure 7.2. MALDI-MS of the starting $Au_{144}(SCH_2CH_2Ph)_{60}$ and its transformation to $Au_{99\text{-}102}$(SPh-*i*Pr)$_{42\text{-}44}$ upon reacting with *i*PrBT ligand at 80 ^{0}C for 48 h. * indicates the 2+ charge state of respective nanomolecules.

To determine the exact composition of the intermediates and the converted Au NMs, ESI-MS analysis was performed. ESI-MS is a softer ionization technique where fragmentation is minimized, and thus it does not inhibit the determination of the Au NM composition.[37] In comparison, MALDI-MS is considered as a hard ionization technique where fragmentation of the Au NMs is observed. The molecular weight of phenylethanethiol and isopropylbenzenethiol are 137.2 and 151.2 Da, which gives a mass difference of 14 Da. The black spectra at the top on Figure 7.3a and 7.3b represents the starting material ($Au_{144}(SCH_2CH_2Ph)_{60}$), which shows peak at 12198 Da and 9149 Da representing the +3 and

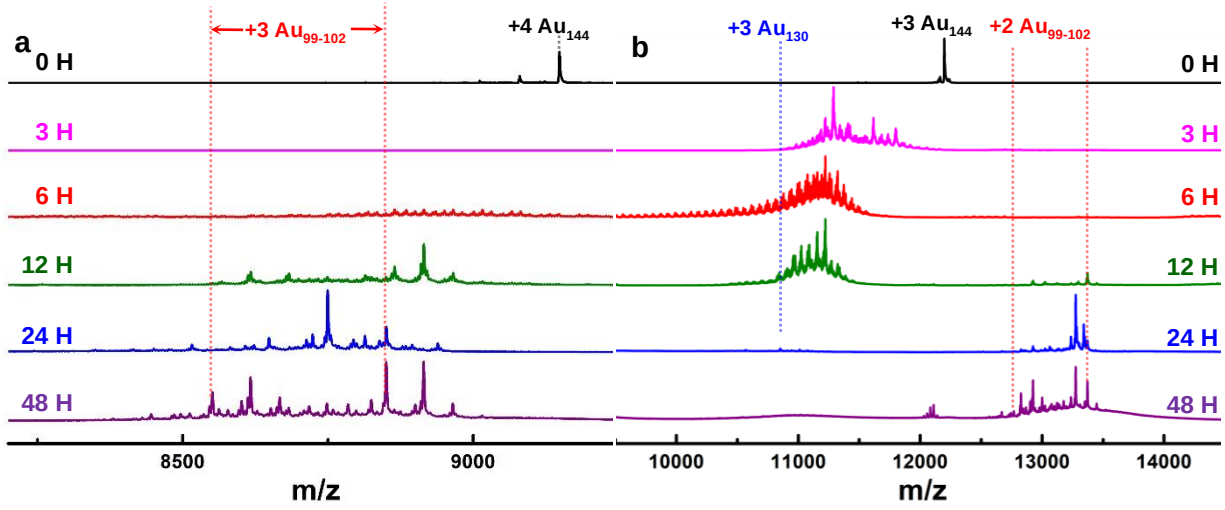

Figure 7.3. ESI-MS spectra of the starting $Au_{144}(SCH_2CH_2Ph)_{60}$ at 0 H, and its transformation to $Au_{99\text{-}102}(SPh\text{-}iPr)_{42\text{-}44}$ upon reacting with *i*PrBT ligand at 80 ^{0}C for 48 H. a) the expanded spectra from 8000 Da to 9500 Da showing the conversion of Au_{144} in +4 charge state to $Au_{99\text{-}102}$ in +3 charge state. b) the expanded spectra from 10,000 Da to 14500 Da showing the conversion of Au_{144} in +3 charge state to $Au_{99\text{-}102}$ in +2 charge state.

+4 of $Au_{144}(SCH_2CH_2Ph)_{60}$. At 3 hours (magenta spectrum), an envelope of peaks was observed representing the initiation of core size conversion. Here, the envelope expands from 11,000 to 12,000 Da, showing the core size conversion and ligand exchange happening simultaneously. At 6 hours (red spectra), the peak around 11,000 Da become dominant and 12,000 Da peaks are decreasing. Here, the core converts to $Au_{130}(SPh\text{-}iPr)_{50}$. The exact +3 charge state mass of $Au_{130}(SPh\text{-}iPr)_{50}$ is 11056 Da. However, at this point the core is still converting with multiple exchange peaks. At 12 hours (olive spectra), the envelope of peaks has reduced to some sharp peaks with mass difference of Au atoms in +3 (66 Da), and simultaneously a new envelope of peaks arises at 13500 Da. These peaks correspond to species $Au_{99\text{-}102}(SPh\text{-}iPr)_{42\text{-}44}$. Similarly, in the mass range from 8000 Da to 9500 Da shown in Figure 7.3a, $Au_{144}(SCH_2CH_2Ph)_{60}$ converts to an envelope of peaks as shown in the 3 hour spectra (magenta) and 6 hour spectra (red) which corresponds to the exchange peaks in the

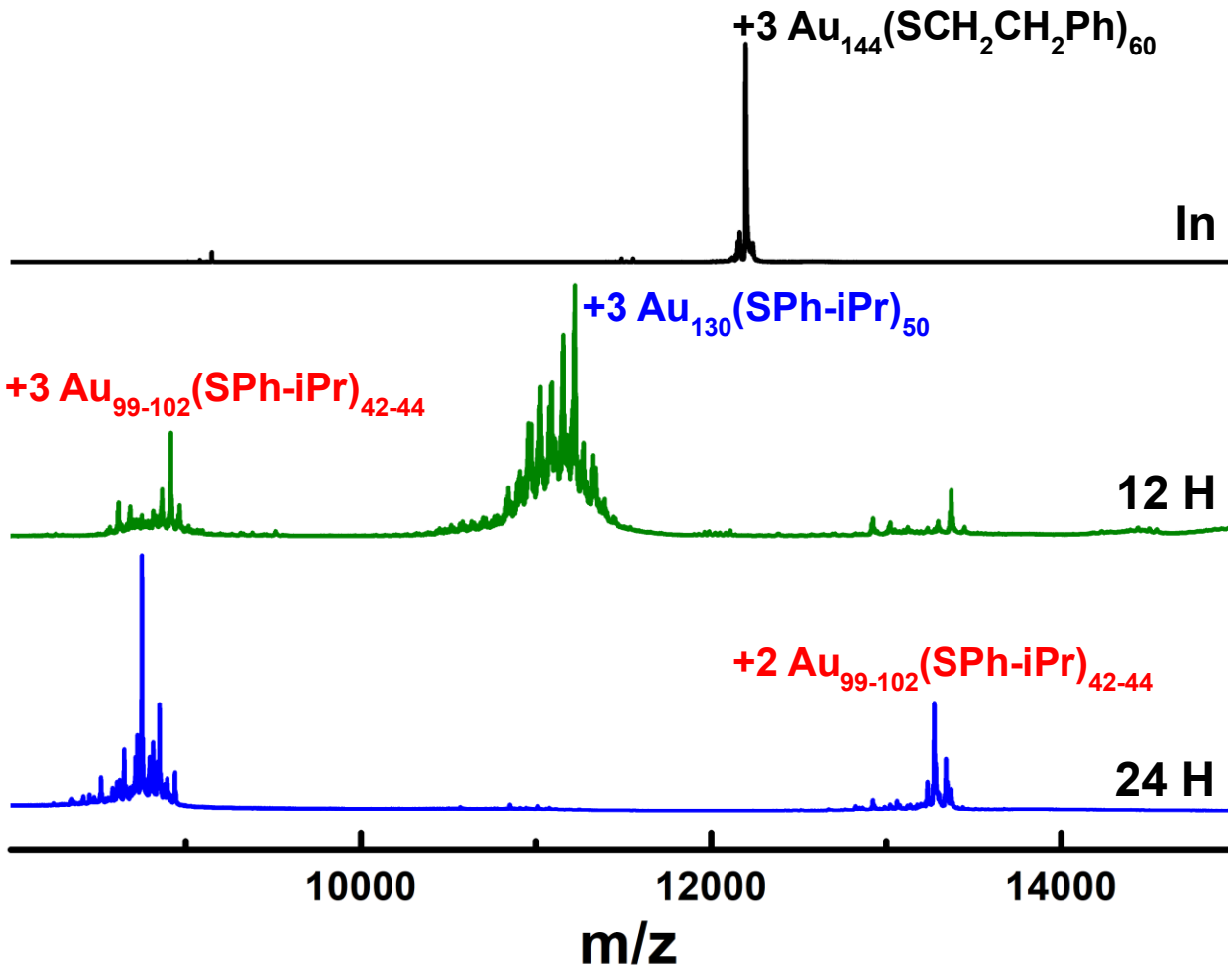

Figure 7.4. ESI-MS spectra of the starting $Au_{144}(SCH_2CH_2Ph)_{60}$ at 0 H, and its transformation to $Au_{99\text{-}102}(SPh\text{-}iPr)_{42\text{-}44}$ upon reacting with *i*PrBT ligand at 80 ^{0}C. At 12-hour Au_{144} converts to 2 size ranges, Au_{130} and $Au_{99\text{-}102}$. In the end, (24 hour) the 2 size ranges completely convert to $Au_{99\text{-}102}$ size.

+4 mass range of $Au_{130}(SPh\text{-}iPr)_{50}$. Then, during continuation of the reaction after 12 hours (olive), the peaks show the exchange peaks of $Au_{99\text{-}102}(SPh\text{-}iPr)_{42\text{-}44}$ in +3 charge state and $Au_{130}(SPh\text{-}iPr)_{50}$ in +4 charge state (Figure 7.4). In continuous reaction, at 24 hours (blue), the core mostly converted to $Au_{99\text{-}102}(SPh\text{-}iPr)_{42\text{-}44}$ and the $Au_{130}(SPh\text{-}iPr)_{50}$ peak became less prominent as shown in Figure 7.3b and 7.4. Similarly, at 24 hours, +3 mass range of $Au_{99\text{-}102}(SPh\text{-}iPr)_{42\text{-}44}$ become more prominent than $Au_{130}(SPh\text{-}iPr)_{50}$ (Figure 7.3a and 7.4). At 48

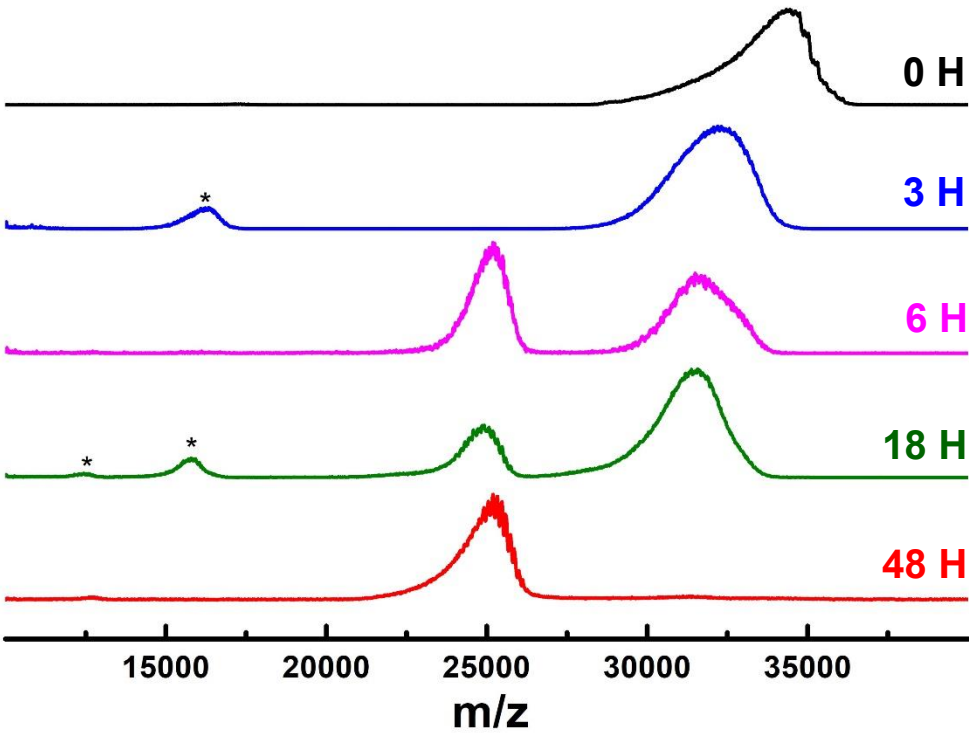

Figure 7.5. MALDI-MS of the starting $Au_{144}(SCH_2CH_2Ph)_{60}$ and its transformation to $Au_{99\text{-}102}(SPh\text{-}Et)_{42\text{-}44}$ and $Au_{130}(SPh\text{-}Et)_{50}$ upon reacting with EtBT ligand at 80 °C for 48 h. * indicates the 2+ charge state of respective nanomolecules.

hours, the core completely converts to $Au_{99\text{-}102}(SPh\text{-}iPr)_{42}$ as shown in Figure 7.3a and 7.3b (purple). However, the distribution of the $Au_{99\text{-}102}(SPh\text{-}iPr)_{42\text{-}44}$ spectra expanded which explains that all the species from $Au_{99}(SPh\text{-}iPr)_{42}$ to $Au_{102}(SPh\text{-}iPr)_{44}$ have good stability and complete conversion into one size is not feasible.

Figure 7.4 shows the reaction sequence better where a pure $Au_{144}(SCH_2CH_2Ph)_{60}$ converts to 2 cores at 12 hours, $Au_{130}(SPh\text{-}iPr)_{50}$ and $Au_{99\text{-}102}(SPh\text{-}iPr)_{42\text{-}44.}$ Then, at 24 hours, the $Au_{130}(SPh\text{-}iPr)_{50}$ has mostly converted to $Au_{99\text{-}102}(SPh\text{-}iPr)_{42\text{-}44}$.

7.4.2 Ligand effect of ethyl group

The same reaction condition was repeated with ethylbenzenethiol. This time the para

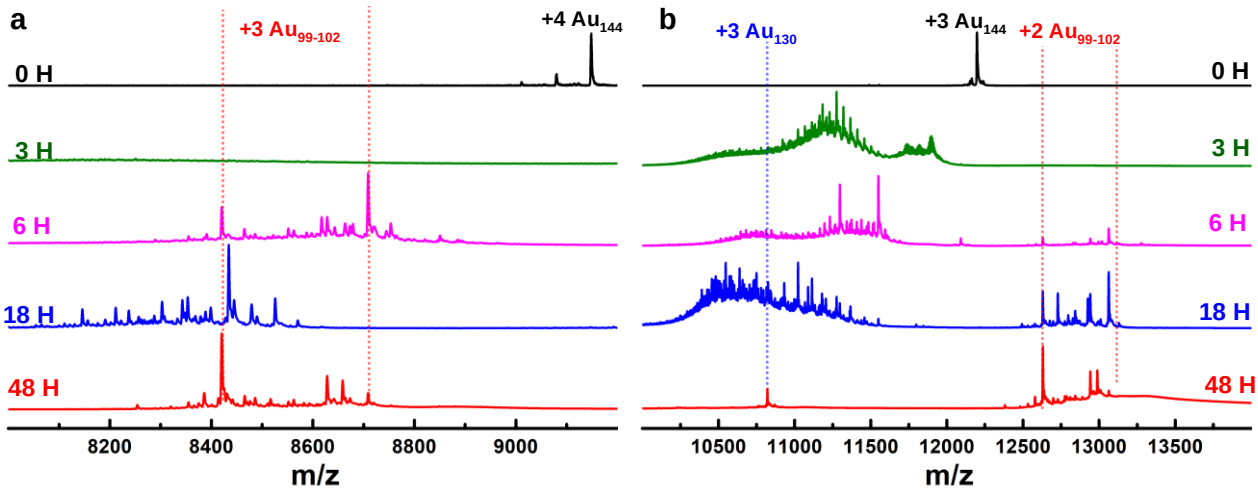

Figure 7.6. ESI-MS spectra of the starting $Au_{144}(SCH_2CH_2Ph)_{60}$ at 0 H, and its transformation to $Au_{99-102}(SPh\text{-}Et)_{42-44}$ upon reacting with SPh-Et ligand at 80 ºC for 48 H. a) the expanded spectra from 8000 Da to 9200 Da showing the conversion of Au_{144} in +4 charge state to Au_{99-102} in +3 charge state. b) the expanded spectra from 10,000 Da to 14000 Da showing the conversion of Au_{144} in +3 charge state to Au_{99-102} in +2 charge state.

position has an ethyl group instead of a tert-butyl group. Note that phenylethanethiol and ethylbenzenethiol have the same molecular weight. The core size conversion with ethylbenzenethiol was done with pure $Au_{144}(C_6H_{13}S)_{60}$. The $Au_{144}(C_6H_{13}S)_{60}$ was synthesized using previously reported method and isolated using SEC. Then the reaction was monitored using MALDI-MS. At 0-hour, pure $Au_{144}(C_6H_{13}S)_{60}$ (33 kDa) was shown in Figure 7.5 (black). At 3 hours (Figure 7.5 (blue), the ligand exchange was happening along with core size conversion and the peak becomes broader centering around 32 kDA ($(Au_{130}(SPh\text{-}Et)_{50}$). At 6 hours, the core converts into two, 32 kDa corresponding to $Au_{130}(SPh\text{-}Et)_{50}$ and 25 kDa corresponding to $Au_{99\text{-}102}(SPh\text{-}Et)_{42\text{-}44}$ as shown in Figure 7.5 (magenta). As the reaction proceeds and at 18 hours, still two cores at 32 and 25 kDa are presented with some mass ratio difference (Figure 7.5 (olive)). Finally, the reaction was allowed to continue up to 48 hours and then stopped. At this point the core had mostly converted to 25 kDa.

As mentioned before, MALDI-MS is a hard ionization technique whereas ESI-MS is a

soft ionization technique. Therefore, the reaction was also monitored using ESI-MS as shown in Figure 7.6. At 0-hour, the staring material $Au_{144}(C_6H_{13}S)_{60,}$ in its +3 charge state at 11799 Da, is shown in Figure 7.6b. Then the rection was started and at 3 hours, the core started to convert towards $Au_{130}(SPh\text{-}Et)_{50}$ (Figure 7.6b (green)). At 6 hours, the core conversion was still happening, but the envelope reduced to some sharper peaks and new peaks start to rise around 13,000 Da corresponding to $Au_{99\text{-}102}(SPh\text{-}Et)_{42\text{-}44}$ (Figure 7.6b (magenta)), which correlates with the MALDI-MS spectra where two cores at 25 and 32 kDa are seen at 6 hours. At 18 hours, the core conversion majorly moves and is now centered around 10882 Da ($Au_{130}(SPh\text{-}Et)_{50}$), and peaks around 13,000 Da become more prominent as shown in Figure 7.6b (blue), consistent with the analysis by MALDI-MS. Similarly, In Figure 7.6a, $Au_{144}(C_6H_{13}S)_{60}$ in its +4 charge starts core converting and shows an envelope of peaks at 6 hours (magenta) centering around $Au_{99\text{-}102}(SPh\text{-}Et)_{42\text{-}44}$. Then, the envelope shifted towards left, shifting the equilibrium beyond $Au_{99\text{-}102}(SPh\text{-}Et)_{42\text{-}44}$. However, finally at 48 hours, the whole $Au_{144}(C_6H_{13}S)_{60}$ has core converted to two cores, $Au_{130}(SPh\text{-}Et)_{50}$ in its +3 charge (10822 Da) and +4 charge (8116 Da) respectively as shown in Figure 7.6b ad 7.6a (red) and $Au_{99\text{-}102}(SPh\text{-}Et)_{42\text{-}44}$ whose +2 charge state species is shown in Figure 7.5b and +3 charge state is shown in Figure 7.5a respectively.

7.4.2 Ligand effect of methyl group

In the final core size conversion investigation the ligand effect of aromatic thiols with different para substitutions, we used para-methylbenzenethiol(PMBT). The same reaction conditions were repeated. In all these core size conversions. PMBT has much higher reaction rate than the other two thiols, therefore the reaction ends in 18 hours. The reaction was first

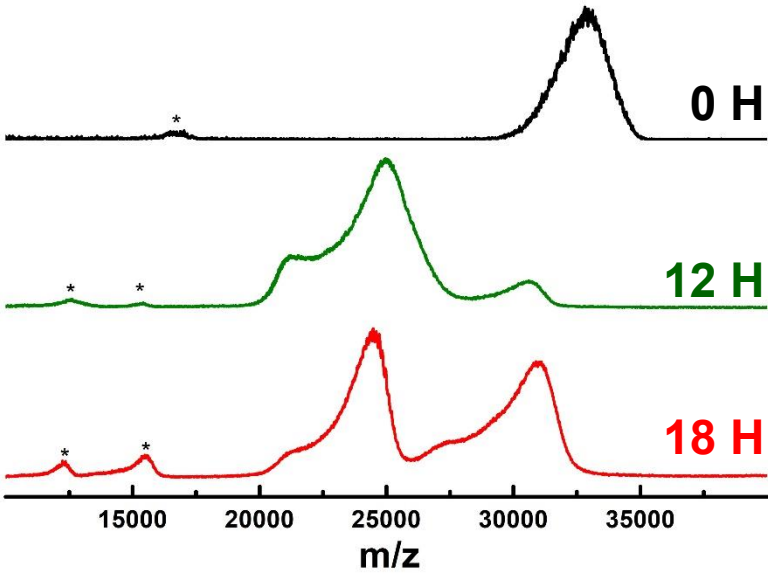

Figure 7.7. MALDI-MS of the starting $Au_{144}(SCH_2CH_2Ph)_{60}$ and its transformation to $Au_{99\text{-}102}(PMBT)_{42\text{-}44}$ and $Au_{130}(PMBT)_{50}$ upon reacting with *PMBT* ligand at 80 °C for 48 h. * indicates the 2+ charge state of respective nanomolecules.

monitored using MALDI-MS as shown in Figure 7.7. The starting material $Au_{144}(SCH_2CH_2Ph)_{60}$ shows a peak at 33 kDa represented by the black spectra in Figure 7.7. At 12 hour the core converts to 2 cores, one at 31 kDa representing $Au_{130}(PMBT)_{50}$ and next one at 25 kDa representing the $Au_{99\text{-}102}(PMBT)_{42\text{-}44}$ (Figure 7.7 (green)). At 18 hours, the two cores become stable and show almost well-defined peaks of $Au_{99\text{-}102}(PMBT)_{42\text{-}44}$ and $Au_{130}(PMBT)_{50}$ (Figure 7.7 (red)).

Then, the reaction was monitored using ESI-MS. The +3 charge state of $Au_{144}(SCH_2CH_2Ph)_{60}$ at 12198 Da represents the purity of starting material at 0-hour (Figure 7.8). At 12 hours, three envelopes of peaks are observed as shown in Figure 7.8 (green). Those three envelopes represent +3 and +2 charge state of $Au_{99\text{-}102}(PMBT)_{42\text{-}44}$ and +3 charge state of $Au_{130}(PMBT)_{50}$ in the middle. Their respective expanded spectra are shown in Figure S7.2, S7.3, S7.4 and S7.5. At 18 hours, the three envelopes reduce to sharp peaks representing

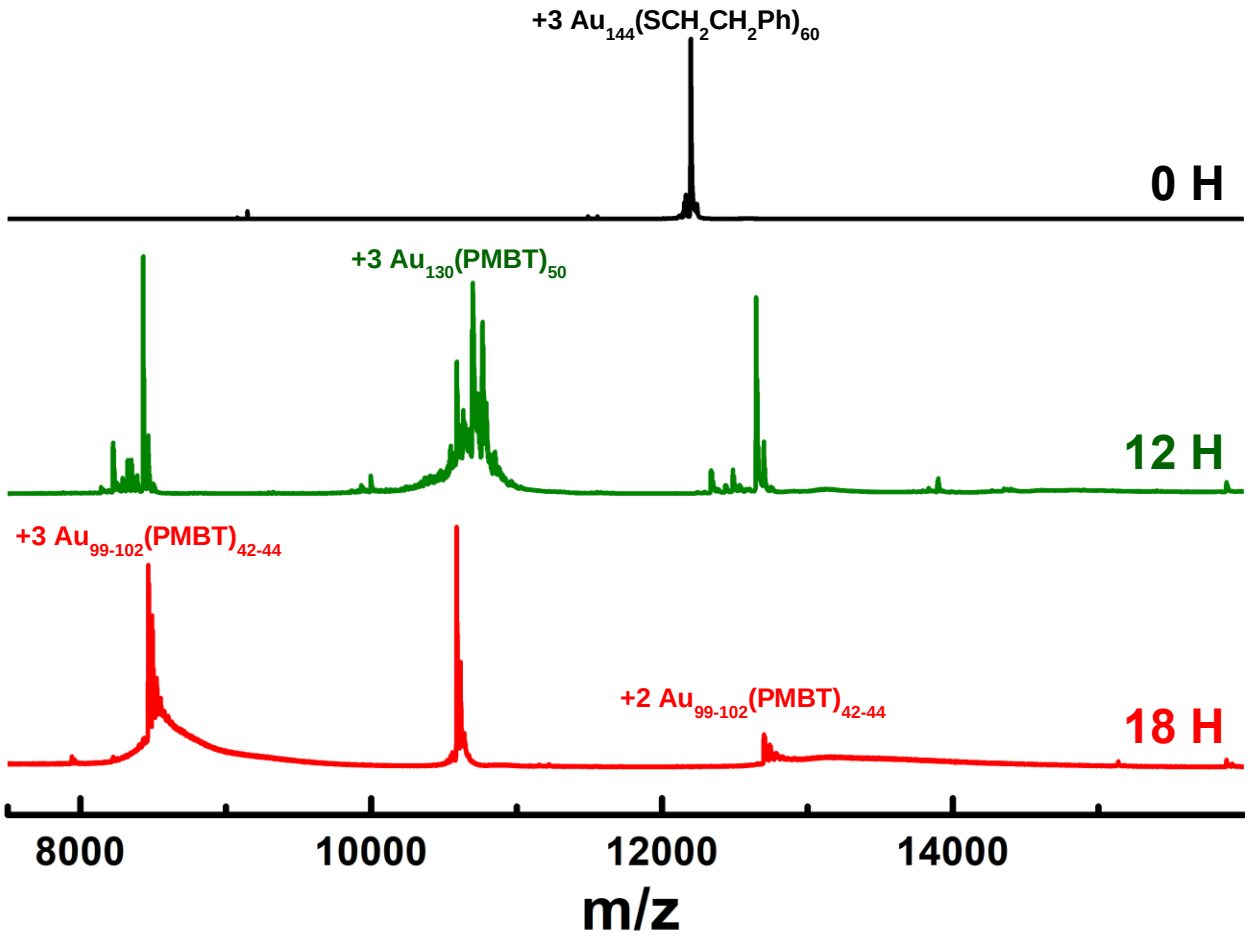

Figure 7.8. ESI-MS spectra of the starting $Au_{144}(SCH_2CH_2Ph)_{60}$ at 0 H, and its transformation to $Au_{99-102}(PMBT)_{42-44}$ and $Au_{130}(PMBT)_{50}$ upon reacting with PMBT ligand at 80 °C. At 12-hour, Au_{144} converts to 2 size ranges, Au_{130} and Au_{99-102}. In the end (18 hour), the 2 size ranges remain stable.

$Au_{99-102}(PMBT)_{42-44}$ and $Au_{130}(PMBT)_{50}$. Figure S7.2 shows expanded spectra from 12300 Da to 13000 Da where the +2 charge state of $Au_{99-102}(PMBT)_{42-44}$ lies. At 12 hours the peaks representing $Au_{99}(PMBT)_{42}$ to $Au_{102}(PMBT)_{44}$ were found; however, at 18 hours the peak converts to $Au_{102}(PMBT)_{44}$. Figure S7.3 shows expanded spectra from 8100 Da to 8650 Da showing the +3 charge state mass range of $Au_{99-102}(PMBT)_{42-44}$. Like the +2 charge state peaks, at 12 hours $Au_{99}(PMBT)_{42}$ to $Au_{102}(PMBT)_{44}$ species was found and it converts to mostly $Au_{102}(PMBT)_{44}$ at 18 hours with minute peaks in $Au_{99}(PMBT)_{42}$ range. Figure S7.4

shows expanded spectra 10400 Da to 11000 Da showing the +3 charge state mass region of $Au_{130}(PMBT)_{50}$. At 12 hours, the envelope of peaks core converting with left most peak representing $Au_{130}(PMBT)_{50}$ was observed. At 18 hours, the peaks converge to $Au_{130}(PMBT)_{50}$ with minute peak at one gold atom difference.

7.5 Conclusions

The results obtained from ESI-MS and MALDI-MS were used to draw final conclusions regarding the ligand effects of substitution of different groups at para position. Repeating the core conversion of $Au_{144}(SR)_{60}$ with TBBT gave the reported $Au_{133}(SPh\text{-}tBu)_{52}$.[39] Also, it showed that prolonged etching for a longer time does not affect the core any more and $Au_{133}(SPh\text{-}tBu)_{52}$ was stable. When we move from tert-butyl to isopropyl group in the para position, the reaction become slower and it converts to $Au_{130}(SR)_{50}$ in the beginning; however, it converts to $Au_{99\text{-}102}(SR)_{42\text{-}44}$ after 48 hours of reaction. In ethyl substituted reaction, similar results were obtained, but in addition to $Au_{99\text{-}102}(SR)_{42\text{-}44}$, $Au_{130}(SR)_{50}$ was also present in small quantity. When we moved from ethyl to methyl para substituted benzenethiol, both $Au_{99\text{-}102}(SR)_{42\text{-}44}$ and

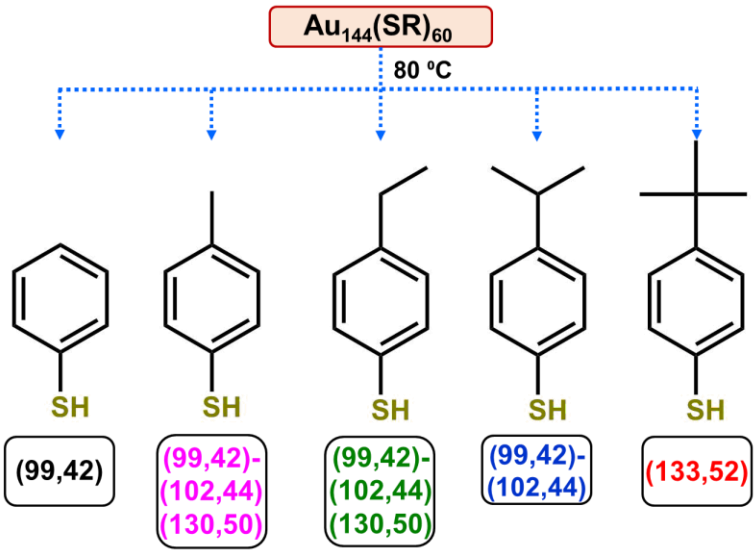

Scheme 7.2 Core size conversion reaction of $Au_{144}(SR)_{60}$ reacted with para substituted aromatic thiolated ligands.

$Au_{130}(SR)_{50}$ were obtained in comparable quantity. The conclusions are summarized in Scheme 7.2.

These reactions shows that $Au_{99\text{-}102}(SR)_{42\text{-}44}$ was obtained in core size conversion of all the para substituted ligands except TBBT. The bulky nature of the tert-butyl group in TBBT makes the $Au_{133}(SR)_{52}$ highly stable which does not allow it to core convert further.[39] But the reaction of TBBT with $Au_{99\text{-}102}(SR)_{42\text{-}44}$ gives $Au_{99\text{-}102}(SR)_{42\text{-}44}$ as reported earlier.[130] It also shows a trend that in PMBT the $Au_{144}(SR)_{60}$ core converts to $Au_{99\text{-}102}(SR)_{42\text{-}44}$ and $Au_{130}(SR)_{50}$, but the amount of $Au_{130}(SR)_{50}$ reduces in ethyl substituted thiol and is finally not found in isopropyl substituted thiol.

7.6 Future works

The formation Au NMs and its composition is mainly based on the protecting ligands. The detailed study on the ligand effect on the formation of Au NMS will provide precise engineering of materials in nanoscale. A small change from tert-butyl group in para position to isopropyl group results in two different cores. Also, the core size conversion proves to be an easy method to study these types of ligand effects.

Currently, the ligand effect on the substitution on para position is studied. In future, the different ligand substitution in ortho and meta position will provide more data towards ligand effects. Number of crystal structures protected by aromatic thiols with various substitution was reported which indicated the feasibility of forming single crystals is higher in aromatic thiols.[10, 14, 33, 42, 84, 127-128, 132, 134, 137] Therefore, focusing on different substituted aromatic thiols will be a good start to study structural evolution using various thiols and their ligand effects. The collection of all these results combined with previously reported

results will provide fundamental understanding of ligand effects on Au NMs. Using that, we will be precisely nanoengineer Au NMs for a targeted application.

REFERENCES

1. Jeevanandam, J.; Barhoum, A.; Chan, Y. S.; Dufresne, A.; Danquah, M. K., Review on nanoparticles and nanostructured materials: history, sources, toxicity and regulations. *Beilstein journal of nanotechnology* **2018**, *9*, 1050-1074.
2. Templeton, A. C.; Wuelfing, W. P.; Murray, R. W., Monolayer-Protected Cluster Molecules. *Acc. Chem. Res.* **2000**, *33*, 27-36.
3. Barber, D. J.; Freestone, I. C., An investigation of the origin of the colour of the Lycurgus cup by analytical transmission electron microscopy,. *Archaeometry* **1990**, *32*, 33-45.
4. Thompson, D., Michael Faraday's recognition of ruby gold: the birth of modern nanotechnology. *Gold Bulletin* **2007**, *40*, 267-269.
5. Mingos, D. M. P., *Gold Clusters, Colloids and Nanoparticles I*, 1 ed.; Springer International Publishing, 2014, p 282.
6. Kumara, C.; Zuo, X.; Ilavsky, J.; Chapman, K. W.; Cullen, D. A.; Dass, A., Super-Stable, Highly Monodisperse Plasmonic Faradaurate-500 Nanocrystals with 500 Gold Atoms: $Au_{\sim 500}(SR)_{\sim 120}$. *J Am Chem Soc* **2014**, *136*, 7410-7.
7. Brust, M.; Walker, M.; Bethell, D.; Schiffrin, D. J.; Whyman, R., Synthesis of thiol-derivatised gold nanoparticles in a two-phase Liquid–Liquid system. *J. Chem. Soc., Chem. Commun.* **1994**, 801-802.
8. Schaaff, T. G.; Whetten, R. L., Controlled Etching of Au:SR Cluster Compounds. *J. Phys. Chem. B* **1999**, *103*, 9394-9396.
9. Whetten, R. L.; Khoury, J. T.; Alvarez, M. M.; Murthy, S.; Vezmar, I.; Wang, Z. L.; Stephens, P. W.; Cleveland, C. L.; Luedtke, W. D.; Landman, U., Nanocrystal gold molecules. *Adv. Mater.* **1996**, *8*, 428-433.
10. Jadzinsky, P. D.; Calero, G.; Ackerson, C. J.; Bushnell, D. A.; Kornberg, R. D., Structure of a Thiol Monolayer-Protected Gold Nanoparticle at 1.1 Å Resolution. *Science* **2007**, *318*, 430-433.
11. Heaven, M. W.; Dass, A.; White, P. S.; Holt, K. M.; Murray, R. W., Crystal Structure of the Gold Nanoparticle $[N(C_8H_{17})_4][Au_{25}(SCH_2CH_2Ph)_{18}]$. *J. Am. Chem. Soc.* **2008**, *130*, 3754-3755.
12. Knoppe, S.; Bürgi, T., Chirality in Thiolate-Protected Gold Clusters. *Acc. Chem. Res.* **2014**, *47*, 1318-1326.
13. Rambukwella, M.; Sakthivel, N. A.; Delcamp, J. H.; Sementa, L.; Fortunelli, A.; Dass, A., Ligand Structure Determines Nanoparticles' Atomic Structure, Metal-Ligand Interface and Properties. *Front. Chem.* **2018**, *6*.
14. Sakthivel, N. A.; Dass, A., Aromatic Thiolate-Protected Series of Gold Nanomolecules and a Contrary Structural Trend in Size Evolution. *Acc. Chem. Res.* **2018**, *51*, 1774-1783.
15. Kumara, C.; Zuo, X.; Ilavsky, J.; Chapman, K. W.; Cullen, D. A.; Dass, A., Super-Stable, Highly Monodisperse Plasmonic Faradaurate-500 Nanocrystals with 500 Gold Atoms: $Au_{\sim 500}(SR)_{\sim 120}$. *J. Am. Chem. Soc.* **2014**, *136*, 7410-7417.
16. Jones, T. C.; Sumner, L.; Ramakrishna, G.; Hatshan, M. b.; Abuhagr, A.; Chakraborty, S.; Dass, A., Bulky t-Butyl Thiolated Gold Nanomolecular Series: Synthesis, Characterization, Optical Properties, and Electrocatalysis. *J. Phys. Chem. C* **2018**, *122*, 17726-17737.
17. Kumara, C.; Dass, A., $Au_{329}(SR)_{84}$ Nanomolecules: Compositional Assignment of the 76.3 kDa Plasmonic Faradaurates. *Anal. Chem.* **2014**, *86*, 4227-4232.
18. Kumara, C.; Zuo, X.; Cullen, D. A.; Dass, A., Faradaurate-940: Synthesis, Mass Spectrometry, Electron Microscopy, High-Energy X-ray Diffraction, and X-ray Scattering Study of $Au_{\sim 940\pm 20}(SR)_{\sim 160\pm 4}$ Nanocrystals. *ACS Nano* **2014**, *8*, 6431-6439.
19. Vergara, S.; Santiago, U.; Kumara, C.; Alducin, D.; Whetten, R. L.; Jose Yacaman, M.; Dass, A.; Ponce, A., Synthesis, Mass Spectrometry, and Atomic Structural Analysis of $Au_{\sim 2000}(SR)_{\sim 290}$ Nanoparticles. *J. Phys. Chem. C* **2018**, *122*, 26733-26738.
20. Alvarez, M. M.; Khoury, J. T.; Schaaff, T. G.; Shafigullin, M. N.; Vezmar, I.; Whetten, R. L., Optical Absorption Spectra of Nanocrystal Gold Molecules. *J. Phys. Chem. B* **1997**, *101*, 3706-3712.
21. Weissker, H. C.; Escobar, H. B.; Thanthirige, V. D.; Kwak, K.; Lee, D.; Ramakrishna, G.; Whetten, R. L.; López-Lozano, X., Information on quantum states pervades the visible spectrum of the ubiquitous Au144(SR)60

gold nanocluster. *Nature Communications* **2014**, *5*, 3785.
22. Giljohann, D. A.; Seferos, D. S.; Daniel, W. L.; Massich, M. D.; Patel, P. C.; Mirkin, C. A., Gold Nanoparticles for Biology and Medicine. *Angewandte Chemie (International ed. in English)* **2010**, *49*, 3280-3294.
23. Mayer, K. M.; Hafner, J. H., Localized Surface Plasmon Resonance Sensors. *Chem. Rev.* **2011**, *111*, 3828-3857.
24. Tiwari, P.; Vig, K.; Dennis, V.; Singh, S., Functionalized Gold Nanoparticles and Their Biomedical Applications. *Nanomaterials* **2011**, *1*, 31.
25. Capek, I., Polymer decorated gold nanoparticles in nanomedicine conjugates. *Adv. Colloid Interface Sci.* **2017**, *249*, 386-399.
26. Petros, R. A.; DeSimone, J. M., Strategies in the design of nanoparticles for therapeutic applications. *Nature Reviews Drug Discovery* **2010**, *9*, 615.
27. Ghosh, P.; Han, G.; De, M.; Kim, C. K.; Rotello, V. M., Gold nanoparticles in delivery applications. *Advanced Drug Delivery Reviews* **2008**, *60*, 1307-1315.
28. Delehanty, J. B.; Boeneman, K.; Bradburne, C. E.; Robertson, K.; Bongard, J. E.; Medintz, I. L., Peptides for specific intracellular delivery and targeting of nanoparticles: implications for developing nanoparticle-mediated drug delivery. *Therapeutic delivery* **2010**, *1*, 411-33.
29. Zhu, W.; Michalsky, R.; Metin, Ö.; Lv, H.; Guo, S.; Wright, C. J.; Sun, X.; Peterson, A. A.; Sun, S., Monodisperse Au Nanoparticles for Selective Electrocatalytic Reduction of CO_2 to CO. *J. Am. Chem. Soc.* **2013**, *135*, 16833-16836.
30. Abbas, M. A.; Kim, T.-Y.; Lee, S. U.; Kang, Y. S.; Bang, J. H., Exploring Interfacial Events in Gold-Nanocluster-Sensitized Solar Cells: Insights into the Effects of the Cluster Size and Electrolyte on Solar Cell Performance. *J. Am. Chem. Soc.* **2016**, *138*, 390-401.
31. Schaaff, T. G.; Whetten, R. L., Controlled Etching of Au:SR Cluster Compounds. *J. Phys. Chem. B* **1999**, *103*, 9394.
32. Perala, S. R. K.; Kumar, S., On the Mechanism of Metal Nanoparticle Synthesis in the Brust–Schiffrin Method. *Langmuir* **2013**, *29*, 9863-9873.
33. Sakthivel, N. A.; Theivendran, S.; Ganeshraj, V.; Oliver, A. G.; Dass, A., Crystal Structure of Faradaurate-279: Au_{279}(SPh-tBu)$_{84}$ Plasmonic Nanocrystal Molecules. *J. Am. Chem. Soc.* **2017**, *139*, 15450-15459.
34. Knoppe, S.; Boudon, J.; Dolamic, I.; Dass, A.; Bürgi, T., Size Exclusion Chromatography for Semipreparative Scale Separation of $Au_{38}(SR)_{24}$ and $Au_{40}(SR)_{24}$ and Larger Clusters. *Anal. Chem.* **2011**, *83*, 5056-5061.
35. Sakthivel, N. A.; Jupally, V. R.; Eswaramoorthy, S. K.; Wijesinghe, K. H.; Nimmala, P. R.; Kumara, C.; Rambukwella, M.; Jones, T.; Dass, A., Size Exclusion Chromatography: An Indispensable Tool for the Isolation of Monodisperse Gold Nanomolecules. *Anal. Chem.* **2021**, *93*, 3987-3996.
36. Knoppe, S.; Boudon, J.; Dolamic, I.; Dass, A.; Bürgi, T., Size Exclusion Chromatography for Semipreparative Scale Separation of Au38(SR)24 and Au40(SR)24 and Larger Clusters. *Anal. Chem.* **2011**, *83*, 5056.
37. Zeng, C.; Liu, C.; Pei, Y.; Jin, R., Thiol Ligand-Induced Transformation of $Au_{38}(SC_2H_4Ph)_{24}$ to Au_{36}(SPh-t-Bu)$_{24}$. *ACS Nano* **2013**, *7*, 6138-6145.
38. Nimmala, P. R.; Dass, A., $Au_{99}(SPh)_{42}$ Nanomolecules: Aromatic Thiolate Ligand Induced Conversion of $Au_{144}(SCH_2CH_2Ph)_{60}$. *J. Am. Chem. Soc.* **2014**, *136*, 17016-17023.
39. Nimmala, P. R.; Theivendran, S.; Barcaro, G.; Sementa, L.; Kumara, C.; Jupally, V. R.; Apra, E.; Stener, M.; Fortunelli, A.; Dass, A., Transformation of $Au_{144}(SCH_2CH_2Ph)_{60}$ to Au_{133}(SPh-tBu)$_{52}$ Nanomolecules: Theoretical and Experimental Study. *J. Phys. Chem. Lett.* **2015**, *6*, 2134-2139.
40. Zeng, C.; Qian, H.; Li, T.; Li, G.; Rosi, N. L.; Yoon, B.; Barnett, R. N.; Whetten, R. L.; Landman, U.; Jin, R., Total Structure and Electronic Properties of the Gold Nanocrystal $Au_{36}(SR)_{24}$. *Angew. Chem. Int. Ed.* **2012**, *51*, 13114-13118.
41. Eswaramoorthy, S. K.; Sakthivel, N. A.; Dass, A., Core Size Conversion of $Au_{329}(SCH_2CH_2Ph)_{84}$ to Au_{279}(SPh-tBu)$_{84}$ Nanomolecules. *J. Phys. Chem. C* **2019**.
42. Zeng, C.; Li, T.; Das, A.; Rosi, N. L.; Jin, R., Chiral Structure of Thiolate-Protected 28-Gold-Atom Nanocluster Determined by X-ray Crystallography. *J. Am. Chem. Soc.* **2013**, *135*, 10011-10013.
43. Tracy, J. B.; Crowe, M. C.; Parker, J. F.; Hampe, O.; Fields-Zinna, C. A.; Dass, A.; Murray, R. W., Electrospray Ionization Mass Spectrometry of Uniform and Mixed Monolayer Nanoparticles: $Au_{25}[S(CH_2)_2Ph]_{18}$ and $Au_{25}[S(CH_2)_2Ph]_{18-x}(SR)_x$. *J. Am. Chem. Soc.* **2007**, *129*, 16209-16215.
44. Dass, A.; Stevenson, A.; Dubay, G. R.; Tracy, J. B.; Murray, R. W., Nanoparticle MALDI-TOF Mass Spectrometry without Fragmentation: $Au_{25}(SCH_2CH_2Ph)_{18}$ and Mixed Monolayer $Au_{25}(SCH_2CH_2Ph)_{18-x}$(L)x. *J. Am. Chem. Soc.* **2008**, *130*, 5940.

45. Angel, L. A.; Majors, L. T.; Dharmaratne, A. C.; Dass, A., Ion Mobility Mass Spectrometry of $Au_{25}(SCH_2CH_2Ph)_{18}$ Nanoclusters. *ACS Nano* **2010**, *4*, 4691.
46. Cole, R. B., Electrospray and MALDI Mass Spectrometry Fundamentals, Instrumentation, Practicalities, and Biological Applications. **2010**.
47. Tanaka, K.; Waki, H.; Ido, Y.; Akita, S.; Yoshida, Y.; Yoshida, T.; Matsuo, T., Protein and polymer analyses up to m/z 100 000 by laser ionization time-of-flight mass spectrometry. *Rapid Commun. Mass Spectrom.* **1988**, *2*, 151-153.
48. Dass, A.; Stevenson, A.; Dubay, G. R.; Tracy, J. B.; Murray, R. W., Nanoparticle MALDI-TOF Mass Spectrometry without Fragmentation: $Au_{25}(SCH_2CH_2Ph)_{18}$ and Mixed Monolayer $Au_{25}(SCH_2CH_2Ph)_{18-x}(L)_x$. *J. Am. Chem. Soc.* **2008**, *130*, 5940-5946.
49. Negishi, Y.; Takasugi, Y.; Sato, S.; Yao, H.; Kimura, K.; Tsukuda, T., Magic-Numbered Au_n Clusters Protected by Glutathione Monolayers (n = 18, 21, 25, 28, 32, 39): Isolation and Spectroscopic Characterization. *J. Am. Chem. Soc.* **2004**, *126*, 6518-6519.
50. Negishi, Y.; Nobusada, K.; Tsukuda, T., Glutathione-Protected Gold Clusters Revisited: Bridging the Gap between Gold(I)−Thiolate Complexes and Thiolate-Protected Gold Nanocrystals. *J. Am. Chem. Soc.* **2005**, *127*, 5261-5270.
51. Shichibu, Y.; Negishi, Y.; Tsukuda, T.; Teranishi, T., Large-Scale Synthesis of Thiolated Au_{25} Clusters via Ligand Exchange Reactions of Phosphine-Stabilized Au_{11} Clusters. *J. Am. Chem. Soc.* **2005**, *127*, 13464-13465.
52. Negishi, Y.; Takasugi, Y.; Sato, S.; Yao, H.; Kimura, K.; Tsukuda, T., Kinetic Stabilization of Growing Gold Clusters by Passivation with Thiolates. *J. Phys. Chem. B* **2006**, *110*, 12218-12221.
53. Rambukwella, M.; Sakthivel, N. A.; Delcamp, J. H.; Sementa, L.; Fortunelli, A.; Dass, A., Ligand Structure Determines Nanoparticles' Atomic Structure, Metal-Ligand Interface and Properties. *Front. Chem.* **2018**, *6*, 330.
54. Dass, A., Faradaurate Nanomolecules: A Superstable Plasmonic 76.3 kDa Cluster. *J. Am. Chem. Soc.* **2011**, *133*, 19259-19261.
55. Hostetler, M. J.; Green, S. J.; Stokes, J. J.; Murray, R. W., Monolayers in Three Dimensions: Synthesis and Electrochemistry of ω-Functionalized Alkanethiolate-Stabilized Gold Cluster Compounds. *J. Am. Chem. Soc.* **1996**, *118*, 4212-4213.
56. Jupally, V. R.; Kota, R.; Dornshuld, E. V.; Mattern, D. L.; Tschumper, G. S.; Jiang, D.-e.; Dass, A., Interstaple Dithiol Cross-Linking in Au25(SR)18 Nanomolecules: A Combined Mass Spectrometric and Computational Study. *J. Am. Chem. Soc.* **2011**, *133*, 20258-20266.
57. Heinecke, C. L.; Ni, T. W.; Malola, S.; Mäkinen, V.; Wong, O. A.; Häkkinen, H.; Ackerson, C. J., Structural and Theoretical Basis for Ligand Exchange on Thiolate Monolayer Protected Gold Nanoclusters. *J. Am. Chem. Soc.* **2012**, *134*, 13316-13322.
58. Guo, R.; Song, Y.; Wang, G.; Murray, R. W., Does Core Size Matter in the Kinetics of Ligand Exchanges of Monolayer-Protected Au Clusters? *J. Am. Chem. Soc.* **2005**, *127*, 2752-2757.
59. Si, S.; Gautier, C.; Boudon, J.; Taras, R.; Gladiali, S.; Bürgi, T., Ligand Exchange on Au_{25} Cluster with Chiral Thiols. *J. Phys. Chem. C* **2009**, *113*, 12966-12969.
60. Ni, T. W.; Tofanelli, M. A.; Phillips, B. D.; Ackerson, C. J., Structural Basis for Ligand Exchange on $Au_{25}(SR)_{18}$. *Inorg. Chem.* **2014**, *53*, 6500-6502.
61. Huang, Z.; Ishida, Y.; Narita, K.; Yonezawa, T., Kinetics of Cationic-Ligand-Exchange Reactions in Au_{25} Nanoclusters. *J. Phys. Chem. C* **2018**, *122*, 18142-18150.
62. Niihori, Y.; Hossain, S.; Kumar, B.; Nair, L. V.; Kurashige, W.; Negishi, Y., Perspective: Exchange Reactions in Thiolate-Protected Metal Clusters. *APL Materials* **2017**, *5*, 053201.
63. Nimmala, P. R.; Dass, A., $Au_{36}(SPh)_{23}$ Nanomolecules. *J. Am. Chem. Soc.* **2011**, *133*, 9175-9177.
64. Zeng, C.; Chen, Y.; Das, A.; Jin, R., Transformation Chemistry of Gold Nanoclusters: From One Stable Size to Another. *J. Phys. Chem. Lett.* **2015**, *6*, 2976-2986.
65. Dass, A.; Jones, T. C.; Theivendran, S.; Sementa, L.; Fortunelli, A., Core Size Interconversions of $Au_{30}(S\text{-}tBu)_{18}$ and $Au_{36}(SPhX)_{24}$. *J. Phys. Chem. C* **2017**, *121*, 14914-14919.
66. Rambukwella, M.; Sementa, L.; Fortunelli, A.; Dass, A., Core-Size Conversion of $Au_{38}(SCH_2CH_2Ph)_{24}$ to $Au_{30}(S–tBu)_{18}$ Nanomolecules. *J. Phys. Chem. C* **2017**, *121*, 14929-14935.
67. Theivendran, S.; Dass, A., Synthesis of Aromatic Thiolate-Protected Gold Nanomolecules by Core Conversion: The Case of $Au_{36}(SPh\text{-}t\text{Bu})_{24}$. *Langmuir* **2017**, *33*, 7446-7451.
68. Zeng, C.; Chen, Y.; Kirschbaum, K.; Appavoo, K.; Sfeir, M. Y.; Jin, R., Structural patterns at all scales in a

nonmetallic chiral $Au_{133}(SR)_{52}$ nanoparticle. *Sci. Adv.* **2015**, *1*, e1500045.
69. Nimmala, P. R.; Jupally, V. R.; Dass, A., Core Size Conversion: Route for Exclusive Synthesis of Au_{38} or Au_{40} Nanomolecules. *Langmuir* **2014**, *30*, 2490-2497.
70. Gan, Z.; Xia, N.; Wu, Z., Discovery, Mechanism, and Application of Antigalvanic Reaction. *Acc. Chem. Res.* **2018**, *51*, 2774-2783.
71. Wang, S.; Li, Q.; Kang, X.; Zhu, M., Customizing the Structure, Composition, and Properties of Alloy Nanoclusters by Metal Exchange. *Acc. Chem. Res.* **2018**, *51*, 2784-2792.
72. Rambukwella, M.; Burrage, S.; Neubrander, M.; Baseggio, O.; Aprà, E.; Stener, M.; Fortunelli, A.; Dass, A., $Au_{38}(SPh)_{24}$: Au38 Protected with Aromatic Thiolate Ligands. *J. Phys. Chem. Lett.* **2017**, *8*, 1530-1537.
73. Nimmala, P. R.; Knoppe, S.; Jupally, V. R.; Delcamp, J. H.; Aikens, C. M.; Dass, A., $Au_{36}(SPh)_{24}$ Nanomolecules: X-ray Crystal Structure, Optical Spectroscopy, Electrochemistry, and Theoretical Analysis. *J. Phys. Chem. B* **2014**, *118*, 14157-14167.
74. Dong, H.; Liao, L.; Wu, Z., Two-Way Transformation Between FCC- and NonFCC-Structured Gold Nanoclusters. *J. Phys. Chem. Lett.* **2017**, *8*, 5338-5343.
75. Higaki, T.; Liu, C.; Chen, Y.; Zhao, S.; Zeng, C.; Jin, R.; Wang, S.; Rosi, N. L.; Jin, R., Oxidation-Induced Transformation of Eight-Electron Gold Nanoclusters: $[Au_{23}(SR)_{16}]^-$ to $[Au_{28}(SR)_{20}]^0$. *J. Phys. Chem. Lett.* **2017**, *8*, 866-870.
76. Dainese, T.; Antonello, S.; Bogialli, S.; Fei, W.; Venzo, A.; Maran, F., Gold Fusion: From $Au_{25}(SR)_{18}$ to $Au_{38}(SR)_{24}$, the Most Unexpected Transformation of a Very Stable Nanocluster. *ACS Nano* **2018**, *12*, 7057-7066.
77. Higaki, T.; Liu, C.; Zhou, M.; Luo, T.-Y.; Rosi, N. L.; Jin, R., Tailoring the Structure of 58-Electron Gold Nanoclusters: $Au_{103}S_2(S\text{-}Nap)_{41}$ and Its Implications. *J. Am. Chem. Soc.* **2017**, *139*, 9994-10001.
78. Rambukwella, M.; Sementa, L.; Barcaro, G.; Fortunelli, A.; Dass, A., Organosoluble $Au_{102}(SPh)_{44}$ Nanomolecules: Synthesis, Isolation, Compositional Assignment, Core Conversion, Optical Spectroscopy, Electrochemistry, and Theoretical Analysis. *J. Phys. Chem. C* **2015**, *119*, 25077-25084.
79. Sakthivel, N. A.; Stener, M.; Sementa, L.; Fortunelli, A.; Ramakrishna, G.; Dass, A., $Au_{279}(SR)_{84}$: The Smallest Gold Thiolate Nanocrystal That Is Metallic and the Birth of Plasmon. *J. Phys. Chem. Lett.* **2018**, *9*, 1295-1300.
80. Sumner, L.; Sakthivel, N. A.; Schrock, H.; Artyushkova, K.; Dass, A.; Chakraborty, S., Electrocatalytic Oxygen Reduction Activities of Thiol Protected Nanomolecules Ranging in Size from $Au_{28}(SR)_{20}$ to $Au_{279}(SR)_{84}$. *J. Phys. Chem. C* **2018**, Accepted. DOI: 10.1021/acs.jpcc.8b07962.
81. Higaki, T.; Zhou, M.; Lambright, K. J.; Kirschbaum, K.; Sfeir, M. Y.; Jin, R., Sharp Transition from Nonmetallic Au_{246} to Metallic Au_{279} with Nascent Surface Plasmon Resonance. *J. Am. Chem. Soc.* **2018**, *140*, 5691-5695.
82. Negishi, Y.; Nakazaki, T.; Malola, S.; Takano, S.; Niihori, Y.; Kurashige, W.; Yamazoe, S.; Tsukuda, T.; Häkkinen, H., A Critical Size for Emergence of Nonbulk Electronic and Geometric Structures in Dodecanethiolate-Protected Au Clusters. *J. Am. Chem. Soc.* **2015**, *137*, 1206-1212.
83. Kwak, K.; Thanthirige, V. D.; Pyo, K.; Lee, D.; Ramakrishna, G., Energy Gap Law for Exciton Dynamics in Gold Cluster Molecules. *J. Phys. Chem. Lett.* **2017**, *8*, 4898-4905.
84. Dass, A.; Theivendran, S.; Nimmala, P. R.; Kumara, C.; Jupally, V. R.; Fortunelli, A.; Sementa, L.; Barcaro, G.; Zuo, X.; Noll, B. C., $Au_{133}(SPh\text{-}t\text{Bu})_{52}$ Nanomolecules: X-ray Crystallography, Optical, Electrochemical, and Theoretical Analysis. *J. Am. Chem. Soc.* **2015**, *137*, 4610-4613.
85. Downs, E. L.; Tyler, D. R., Nanoparticle catalysts for nitrile hydration. *Coord. Chem. Rev.* **2014**, *280*, 28-37.
86. Fang, J.; Zhang, B.; Yao, Q.; Yang, Y.; Xie, J.; Yan, N., Recent advances in the synthesis and catalytic applications of ligand-protected, atomically precise metal nanoclusters. *Coord. Chem. Rev.* **2016**, *322*, 1-29.
87. Sun, S.; Mendes, P.; Critchley, K.; Diegoli, S.; Hanwell, M.; Evans, S. D.; Leggett, G. J.; Preece, J. A.; Richardson, T. H., Fabrication of Gold Micro- and Nanostructures by Photolithographic Exposure of Thiol-Stabilized Gold Nanoparticles. *Nano Lett.* **2006**, *6*, 345-350.
88. Schaal, P. A.; Besmehn, A.; Maynicke, E.; Noyong, M.; Beschoten, B.; Simon, U., Electrically Conducting Nanopatterns Formed by Chemical e-Beam Lithography via Gold Nanoparticle Seeds. *Langmuir* **2012**, *28*, 2448-2454.
89. Crasto, D.; Dass, A., Green Gold: $Au_{30}(S\text{-}t\text{-}C_4H_9)_{18}$ Molecules. *J. Phys. Chem. C* **2013**, *117*, 22094-22097.
90. Crasto, D.; Malola, S.; Brosofsky, G.; Dass, A.; Häkkinen, H., Single Crystal XRD Structure and Theoretical Analysis of the Chiral $Au_{30}S(S\text{-}t\text{-}Bu)_{18}$ Cluster. *J. Am. Chem. Soc.* **2014**, *136*, 5000-5005.

91. Yang, H.; Wang, Y.; Edwards, A. J.; Yan, J.; Zheng, N., High-yield synthesis and crystal structure of a green Au_{30} cluster co-capped by thiolate and sulfide. *Chem. Commun.* **2014**, *50*, 14325-14327.
92. Booth, S. G.; Uehara, A.; Chang, S. Y.; La Fontaine, C.; Fujii, T.; Okamoto, Y.; Imai, T.; Schroeder, S. L. M.; Dryfe, R. A. W., The significance of bromide in the Brust–Schiffrin synthesis of thiol protected gold nanoparticles. *Chem. Sci.* **2017**, *8*, 7954-7962.
93. Cao, Y.; Liu, T.; Chen, T.; Zhang, B.; Jiang, D.-e.; Xie, J., Revealing the etching process of water-soluble Au_{25} nanoclusters at the molecular level. *Nature Communications* **2021**, *12*, 3212.
94. Bhakta, A.; Ruckenstein, E., Ostwald ripening: A stochastic approach. *J. Chem. Phys* **1995**, *103*, 7120-7135.
95. Lifshitz, I. M.; Slyozov, V. V., The kinetics of precipitation from supersaturated solid solutions. *J. Phys. Chem. Solids* **1961**, *19*, 35-50.
96. Wagner, C., Theorie der Alterung von Niederschlägen durch Umlösen (Ostwald-Reifung). *Zeitschrift für Elektrochemie, Berichte der Bunsengesellschaft für physikalische Chemie* **1961**, *65*, 581-591.
97. Lin, X., Sorensen, C. & Klabunde, K., Digestive Ripening, Nanophase Segregation and Superlattice Formation in Gold Nanocrystal Colloids. *J. Nanopart. Res.* **2000**, *2*, 157-164.
98. Jose, D.; Jagirdar, B. R., Au@Pd Core–Shell Nanoparticles through Digestive Ripening. *J. Phys. Chem. C* **2008**, *112*, 10089-10094.
99. Shimpi, J. R.; Sidhaye, D. S.; Prasad, B. L. V., Digestive Ripening: A Fine Chemical Machining Process on the Nanoscale. *Langmuir* **2017**, *33*, 9491-9507.
100. Seth, J.; Prasad, B. L. V., Bromide ion mediated modification to digestive ripening process: Preparation of ultra-small Pd, Pt, Rh and Ru nanoparticles. *Nano Research* **2016**, *9*, 2007-2017.
101. Sahu, P.; Prasad, B. L. V., Fine control of nanoparticle sizes and size distributions: temperature and ligand effects on the digestive ripening process. *Nanoscale* **2013**, *5*, 1768-1771.
102. Prasad, B. L. V.; Stoeva, S. I.; Sorensen, C. M.; Klabunde, K. J., Digestive Ripening of Thiolated Gold Nanoparticles: The Effect of Alkyl Chain Length. *Langmuir* **2002**, *18*, 7515-7520.
103. Lin, M.-L.; Yang, F.; Lee, S., Digestive ripening for self-assembly of thiol-capped gold nanoparticles: the effects of adding dodecanethiol and reflux-heating. *Colloids Surf.* **2014**, *448*, 16-22.
104. Sahu, P.; Prasad, B. L. V., Effect of digestive ripening agent on nanoparticle size in the digestive ripening process. *Chem. Phys. Lett.* **2012**, *525-526*, 101-104.
105. Wang, P.; Qi, X.; Zhang, X.; Wang, T.; Li, Y.; Zhang, K.; Zhao, S.; Zhou, J.; Fu, Y., Solvent: A Key in Digestive Ripening for Monodisperse Au Nanoparticles. *Nanoscale Res. Lett.* **2017**, *12*, 25.
106. Qian, H.; Jin, R., Ambient Synthesis of $Au_{144}(SR)_{60}$ Nanoclusters in Methanol. *Chem. Mater.* **2011**, *23*, 2209-2217.
107. Zhu, M.; Lanni, E.; Garg, N.; Bier, M. E.; Jin, R., Kinetically Controlled, High-Yield Synthesis of Au_{25} Clusters. *J. Am. Chem. Soc.* **2008**, *130*, 1138-1139.
108. Luo, Z.; Nachammai, V.; Zhang, B.; Yan, N.; Leong, D. T.; Jiang, D.-e.; Xie, J., Toward Understanding the Growth Mechanism: Tracing All Stable Intermediate Species from Reduction of Au(I)–Thiolate Complexes to Evolution of Au_{25} Nanoclusters. *J. Am. Chem. Soc.* **2014**, *136*, 10577-10580.
109. Jupally, V. R.; Dharmaratne, A. C.; Crasto, D.; Huckaba, A. J.; Kumara, C.; Nimmala, P. R.; Kothalawala, N.; Delcamp, J. H.; Dass, A., $Au_{137}(SR)_{56}$ nanomolecules: composition, optical spectroscopy, electrochemistry and electrocatalytic reduction of CO_2. *Chem. Commun.* **2014**, *50*, 9895-9898.
110. Chaki, N. K.; Negishi, Y.; Tsunoyama, H.; Shichibu, Y.; Tsukuda, T., Ubiquitous 8 and 29 kDa Gold:Alkanethiolate Cluster Compounds: Mass-Spectrometric Determination of Molecular Formulas and Structural Implications. *J. Am. Chem. Soc.* **2008**, *130*, 8608-8610.
111. Chen, S.; Templeton, A. C.; Murray, R. W., Monolayer-Protected Cluster Growth Dynamics. *Langmuir* **2000**, *16*, 3543-3548.
112. Shon, Y.-S.; Mazzitelli, C.; Murray, R. W., Unsymmetrical Disulfides and Thiol Mixtures Produce Different Mixed Monolayer-Protected Gold Clusters. *Langmuir* **2001**, *17*, 7735-7741.
113. García-Barrasa, J.; López-de-Luzuriaga, J. M.; Monge, M.; Soulantica, K.; Viau, G., Synthesis of thiolate-protected silver nanocrystal superlattices from an organometallic precursor and formation of molecular di-n-alkyldisulfide lamellar phases. *J. Nanopart. Res.* **2011**, *13*, 791-801.
114. Li, Y.; Zaluzhna, O.; Tong, Y. J., Critical Role of Water and the Structure of Inverse Micelles in the Brust–Schiffrin Synthesis of Metal Nanoparticles. *Langmuir* **2011**, *27*, 7366-7370.
115. Li, Y.; Zaluzhna, O.; Xu, B.; Gao, Y.; Modest, J. M.; Tong, Y. J., Mechanistic Insights into the Brust–Schiffrin Two-Phase Synthesis of Organo-chalcogenate-Protected Metal Nanoparticles. *J. Am. Chem. Soc.* **2011**, *133*, 2092-2095.

116. Zaluzhna, O.; Li, Y.; Allison, T. C.; Tong, Y. J., Inverse-Micelle-Encapsulated Water-Enabled Bond Breaking of Dialkyl Diselenide/Disulfide: A Critical Step for Synthesizing High-Quality Gold Nanoparticles. *J. Am. Chem. Soc.* **2012**, *134*, 17991-17996.
117. Zaluzhna, O.; Li, Y.; Zangmeister, C.; Allison, T. C.; Tong, Y. J., Mechanistic insights on one-phase vs. two-phase Brust–Schiffrin method synthesis of Au nanoparticles with dioctyl-diselenides. *Chem. Commun.* **2012**, *48*, 362-364.
118. Goulet, P. J. G.; Lennox, R. B., New Insights into Brust–Schiffrin Metal Nanoparticle Synthesis. *J. Am. Chem. Soc.* **2010**, *132*, 9582-9584.
119. Dass, A.; Jones, T.; Rambukwella, M.; Crasto, D.; Gagnon, K. J.; Sementa, L.; De Vetta, M.; Baseggio, O.; Aprà, E.; Stener, M., et al., Crystal Structure and Theoretical Analysis of Green Gold Au_{30}(S-*t*Bu)$_{18}$ Nanomolecules and Their Relation to $Au_{30}S$(S-*t*Bu)$_{18}$. *J. Phys. Chem. C* **2016**, *120*, 6256-6261.
120. Devadas, M. S.; Kim, J.; Sinn, E.; Lee, D.; Goodson, T.; Ramakrishna, G., Unique Ultrafast Visible Luminescence in Monolayer-Protected Au_{25} Clusters. *J. Phys. Chem. C* **2010**, *114*, 22417-22423.
121. Chen, T.; Yao, Q.; Yuan, X.; Nasaruddin, R. R.; Xie, J., Heating or Cooling: Temperature Effects on the Synthesis of Atomically Precise Gold Nanoclusters. *J. Phys. Chem. C* **2017**, *121*, 10743-10751.
122. Maity, P.; Xie, S.; Yamauchi, M.; Tsukuda, T., Stabilized gold clusters: from isolation toward controlled synthesis. *Nanoscale* **2012**, *4*, 4027-4037.
123. Schaaff, T. G.; Shafigullin, M. N.; Khoury, J. T.; Vezmar, I.; Whetten, R. L.; Cullen, W. G.; First, P. N.; Gutiérrez-Wing, C.; Ascensio, J.; Jose-Yacamán, M. J., Isolation of Smaller Nanocrystal Au Molecules: Robust Quantum Effects in Optical Spectra. *J. Phys. Chem. B* **1997**, *101*, 7885-7891.
124. Pei, Y.; Zeng, X. C., Investigating the structural evolution of thiolate protected gold clusters from first-principles. *Nanoscale* **2012**, *4*, 4054-4072.
125. Zhu, M.; Aikens, C. M.; Hollander, F. J.; Schatz, G. C.; Jin, R., Correlating the Crystal Structure of A Thiol-Protected Au_{25} Cluster and Optical Properties. *J. Am. Chem. Soc.* **2008**, *130*, 5883-5885.
126. Qian, H.; Eckenhoff, W. T.; Zhu, Y.; Pintauer, T.; Jin, R., Total Structure Determination of Thiolate-Protected Au_{38} Nanoparticles. *J. Am. Chem. Soc.* **2010**, *132*, 8280-8281.
127. Chen, Y.; Zeng, C.; Liu, C.; Kirschbaum, K.; Gayathri, C.; Gil, R. R.; Rosi, N. L.; Jin, R., Crystal Structure of Barrel-Shaped Chiral Au_{130}(*p*-MBT)$_{50}$ Nanocluster. *J. Am. Chem. Soc.* **2015**, *137*, 10076-10079.
128. Sakthivel, N. A.; Shabaninezhad, M.; Sementa, L.; Yoon, B.; Stener, M.; Whetten, R. L.; Ramakrishna, G.; Fortunelli, A.; Landman, U.; Dass, A., The Missing Link: Au_{191}(SPh-*t*Bu)$_{66}$ Janus Nanoparticle with Molecular and Bulk-Metal-like Properties. *J. Am. Chem. Soc.* **2020**, *142*, 15799-15814.
129. Zeng, C.; Chen, Y.; Kirschbaum, K.; Lambright, K. J.; Jin, R., Emergence of hierarchical structural complexities in nanoparticles and their assembly. *Science* **2016**, *354*, 1580-1584.
130. Sakthivel, N. A.; Sementa, L.; Yoon, B.; Landman, U.; Fortunelli, A.; Dass, A., Isomeric Thiolate Monolayer Protected Au_{92} and Au_{102} Nanomolecules. *J. Phys. Chem. C* **2020**, *124*, 1655-1666.
131. Das, A.; Liu, C.; Zeng, C.; Li, G.; Li, T.; Rosi, N. L.; Jin, R., Cyclopentanethiolato-Protected $Au_{36}(SC_5H_9)_{24}$ Nanocluster: Crystal Structure and Implications for the Steric and Electronic Effects of Ligand. *J. Phys. Chem. A* **2014**, *118*, 8264-8269.
132. Zeng, C.; Chen, Y.; Liu, C.; Nobusada, K.; Rosi, N. L.; Jin, R., Gold tetrahedra coil up: Kekulé-like and double helical superstructures. *Sci. Adv.* **2015**, *1*, e1500425.
133. Rao, B.; Zhao, T.; Yang, S.; Chai, J.; Pan, Y.; Weng, S.; Yu, H.; Li, X.; Zhu, M., X-ray crystal structure and doping mechanism of bimetallic nanocluster $Au_{36-x}Cu_x$(*m*-MBT)$_{24}$ (x = 1–3). *Dalton Transactions* **2018**, *47*, 475-480.
134. Fan, J.; Song, Y.; Chai, J.; Yang, S.; Chen, T.; Rao, B.; Yu, H.; Zhu, M., The solely motif-doped $Au_{36-x}Ag_x$(SPh-*t*Bu)$_{24}$ (x = 1–8) nanoclusters: X-ray crystal structure and optical properties. *Nanoscale* **2016**, *8*, 15317-15322.
135. Sakthivel, N. A.; Stener, M.; Sementa, L.; Medves, M.; Ramakrishna, G.; Fortunelli, A.; Oliver, A. G.; Dass, A., Crystal Structure of $Au_{36-x}Ag_x$(SPh-*t*Bu)$_{24}$ Nanoalloy and the Role of Ag Doping in Excited State Coupling. *J. Phys. Chem. C* **2019**, *123*, 29484-29494.
136. Wan, X.-K.; Guan, Z.-J.; Wang, Q.-M., Homoleptic Alkynyl-Protected Gold Nanoclusters: Au_{44}(PhC≡C)$_{28}$ and Au_{36}(PhC≡C)$_{24}$. *Angew. Chem. Int. Ed.* **2017**, *56*, 11494-11497.
137. Yang, S.; Chai, J.; Song, Y.; Kang, X.; Sheng, H.; Chong, H.; Zhu, M., A New Crystal Structure of Au_{36} with a Au_{14} Kernel Cocapped by Thiolate and Chloride. *J. Am. Chem. Soc.* **2015**, *137*, 10033-10035.
138. Yang ZHOU, Z. L., Kai ZHENG,Gao LI, Controlled Synthesis of $Au_{36}(SR)_{24}$ (SR = SPh, $SC_6H_4CH_3$, $SCH(CH_3)Ph$, and $SC_{10}H_7$) Nanoclusters. *Acta Phys. -Chim. Sin.* **2018**, *34*, 786-791.

139. Rambukwella, M.; Chang, L.; Ravishanker, A.; Fortunelli, A.; Stener, M.; Dass, A., $Au_{36}(SePh)_{24}$ nanomolecules: synthesis, optical spectroscopy and theoretical analysis. *PCCP* **2018**, *20*, 13255-13262.
140. Dolomanov, O. V.; Bourhis, L. J.; Gildea, R. J.; Howard, J. A. K.; Puschmann, H., OLEX2: a complete structure solution, refinement and analysis program. *J. Appl. Crystallogr.* **2009**, *42*, 339-341.
141. Burla, M. C.; Caliandro, R.; Camalli, M.; Carrozzini, B.; Cascarano, G. L.; De Caro, L.; Giacovazzo, C.; Polidori, G.; Siliqi, D.; Spagna, R., IL MILIONE: a suite of computer programs for crystal structure solution of proteins. *J. Appl. Crystallogr.* **2007**, *40*, 609-613.
142. Sheldrick, G., A short history of SHELX. *Acta Crystallographica Section A* **2008**, *64*, 112-122.
143. Schaaff, T. G.; Shafigullin, M. N.; Khoury, J. T.; Vezmar, I.; Whetten, R. L., Properties of a Ubiquitous 29 kDa Au:SR Cluster Compound. *J. Phys. Chem. B* **2001**, *105*, 8785-8796.
144. Antonello, S.; Hesari, M.; Polo, F.; Maran, F., Electron transfer catalysis with monolayer protected Au_{25} clusters. *Nanoscale* **2012**, *4*, 5333-5342.
145. Aiken, J. D.; Finke, R. G., A review of modern transition-metal nanoclusters: their synthesis, characterization, and applications in catalysis. *J. Mol. Catal. A: Chem.* **1999**, *145*, 1-44.
146. Love, J. C.; Estroff, L. A.; Kriebel, J. K.; Nuzzo, R. G.; Whitesides, G. M., Self-Assembled Monolayers of Thiolates on Metals as a Form of Nanotechnology. *Chem. Rev.* **2005**, *105*, 1103-1170.
147. Hartland, G. V., Optical Studies of Dynamics in Noble Metal Nanostructures. *Chem. Rev.* **2011**, *111*, 3858-3887.
148. Alvarez, M. M.; Khoury, J. T.; Schaaff, T. G.; Shafigullin, M.; Vezmar, I.; Whetten, R. L., Critical sizes in the growth of Au clusters. *Chem. Phys. Lett.* **1997**, *266*, 91-98.
149. Balasubramanian, R.; Guo, R.; Mills, A. J.; Murray, R. W., Reaction of $Au_{55}(PPh_3)_{12}Cl_6$ with Thiols Yields Thiolate Monolayer Protected Au_{75} Clusters. *J. Am. Chem. Soc.* **2005**, *127*, 8126-8132.
150. Jimenez, V. L.; Georganopoulou, D. G.; White, R. J.; Harper, A. S.; Mills, A. J.; Lee, D.; Murray, R. W., Hexanethiolate Monolayer Protected 38 Gold Atom Cluster. *Langmuir* **2004**, *20*, 6864-6870.
151. Schaaff, T. G.; Knight, G.; Shafigullin, M. N.; Borkman, R. F.; Whetten, R. L., Isolation and Selected Properties of a 10.4 kDa Gold:Glutathione Cluster Compound. *J. Phys. Chem. B* **1998**, *102*, 10643-10646.
152. Schaaff, T. G.; Whetten, R. L., Giant Gold−Glutathione Cluster Compounds: Intense Optical Activity in Metal-Based Transitions. *J. Phys. Chem. B* **2000**, *104*, 2630-2641.
153. Gutiérrez, E.; Powell, R. D.; Furuya, F. R.; Hainfeld, J. F.; Schaaff, T. G.; Shafigullin, M. N.; Stephens, P. W.; Whetten, R. L., Greengold, a giant cluster compound of unusual electronic structure. *The European Physical Journal D - Atomic, Molecular, Optical and Plasma Physics* **1999**, *9*, 647-651.
154. Dole, M.; Mack, L. L.; Hines, R. L.; Mobley, R. C.; Ferguson, L. D.; Alice, M. B., Molecular Beams of Macroions. *J. Chem. Phys* **1968**, *49*, 2240-2249.
155. Yamashita, M.; Fenn, J. B., Electrospray ion source. Another variation on the free-jet theme. *The Journal of Physical Chemistry* **1984**, *88*, 4451-4459.
156. Tracy, J. B.; Kalyuzhny, G.; Crowe, M. C.; Balasubramanian, R.; Choi, J.-P.; Murray, R. W., Poly(ethylene glycol) Ligands for High-Resolution Nanoparticle Mass Spectrometry. *J. Am. Chem. Soc.* **2007**, *129*, 6706-6707.
157. Udaya Bhaskara Rao, T.; Pradeep, T., Luminescent Ag_7 and Ag_8 Clusters by Interfacial Synthesis. *Angew. Chem. Int. Ed.* **2010**, *49*, 3925-3929.
158. Khatun, E.; Pradeep, T., New Routes for Multicomponent Atomically Precise Metal Nanoclusters. *ACS Omega* **2021**, *6*, 1-16.
159. Xie, J.; Lee, J. Y.; Wang, D. I. C.; Ting, Y. P., Silver Nanoplates: From Biological to Biomimetic Synthesis. *ACS Nano* **2007**, *1*, 429-439.
160. Yuan, X.; Tay, Y.; Dou, X.; Luo, Z.; Leong, D. T.; Xie, J., Glutathione-Protected Silver Nanoclusters as Cysteine-Selective Fluorometric and Colorimetric Probe. *Anal. Chem.* **2013**, *85*, 1913-1919.
161. Yao, Q.; Chen, T.; Yuan, X.; Xie, J., Toward Total Synthesis of Thiolate-Protected Metal Nanoclusters. *Acc. Chem. Res.* **2018**, *51*, 1338-1348.
162. Zhou, M.; Bao, Y.; Jin, S.; Wen, S.; Chen, S.; Zhu, M., $[Ag_{71}(S\text{-}tBu)_{31}(Dppm)](SbF_6)_2$: an intermediate-sized metalloid silver nanocluster containing a building block of Ag_{64}. *Chem. Commun.* **2021**, *57*, 10383-10386.
163. Ma, X.; Bai, Y.; Song, Y.; Li, Q.; Lv, Y.; Zhang, H.; Yu, H.; Zhu, M., Rhombicuboctahedral Ag_{100}: Four-Layered Octahedral Silver Nanocluster Adopting the Russian Nesting Doll Model. *Angew. Chem. Int. Ed.* **2020**, *59*, 17234-17238.
164. Baghdasaryan, A.; Bürgi, T., Copper nanoclusters: designed synthesis, structural diversity, and multiplatform applications. *Nanoscale* **2021**, *13*, 6283-6340.

165. Li, H.; Zhai, H.; Zhou, C.; Song, Y.; Ke, F.; Xu, W. W.; Zhu, M., Atomically Precise Copper Cluster with Intensely Near-Infrared Luminescence and Its Mechanism. *J. Phys. Chem. Lett.* **2020**, *11*, 4891-4896.
166. Tsuji, J., *Palladium reagents and catalysts : innovations in organic synthesis*; Wiley & Sons: Chichester; New York, 2002.
167. Tsuji, J., Palladium in Organic Synthesis. **2005**.
168. Lu, C.-H.; Chang, F.-C., Polyhedral Oligomeric Silsesquioxane-Encapsulating Amorphous Palladium Nanoclusters as Catalysts for Heck Reactions. *ACS Catalysis* **2011**, *1*, 481-488.
169. Cargnello, M.; Wieder, N. L.; Canton, P.; Montini, T.; Giambastiani, G.; Benedetti, A.; Gorte, R. J.; Fornasiero, P., A Versatile Approach to the Synthesis of Functionalized Thiol-Protected Palladium Nanoparticles. *Chem. Mater.* **2011**, *23*, 3961-3969.
170. Mednikov, E. G.; Dahl, L. F., Palladium: It Forms Unique Nano-Sized Carbonyl Clusters. *J. Chem. Educ.* **2009**, *86*, 1135.
171. Mednikov, E. G.; Jewell, M. C.; Dahl, L. F., Nanosized (μ_{12}-Pt)$Pd_{164-x}Pt_x(CO)_{72}(PPh_3)_{20}$ (x ≈ 7) Containing Pt-Centered Four-Shell 165-Atom Pd−Pt Core with Unprecedented Intershell Bridging Carbonyl Ligands: Comparative Analysis of Icosahedral Shell-Growth Patterns with Geometrically Related $Pd_{145}(CO)_x(PEt_3)_{30}$ (x ≈ 60) Containing Capped Three-Shell Pd_{145} Core. *J. Am. Chem. Soc.* **2007**, *129*, 11619-11630.
172. Marshall, S. T.; O'Brien, M.; Oetter, B.; Corpuz, A.; Richards, R. M.; Schwartz, D. K.; Medlin, J. W., Controlled selectivity for palladium catalysts using self-assembled monolayers. *Nature Materials* **2010**, *9*, 853-858.
173. Zhao, S.; Zhang, H.; House, S. D.; Jin, R.; Yang, J. C.; Jin, R., Ultrasmall Palladium Nanoclusters as Effective Catalyst for Oxygen Reduction Reaction. *ChemElectroChem* **2016**, *3*, 1225-1229.
174. Zhang, L.; Hu, Q.; Li, Z.; Zhang, Y.; Lu, D.; Shuang, S.; Choi, Martin M. F.; Dong, C., Chromatographic separation and mass spectrometric analysis of N-acetyl-l-cysteine-protected palladium nanoparticles. *Analytical Methods* **2017**, *9*, 4539-4546.
175. Negishi, Y.; Murayama, H.; Tsukuda, T., Formation of $Pd_n(SR)_m$ clusters (n<60) in the reactions of $PdCl_2$ and RSH (R=n-$C_{18}H_{37}$, n-$C_{12}H_{25}$). *Chem. Phys. Lett.* **2002**, *366*, 561-566.
176. Murayama, H.; Ichikuni, N.; Negishi, Y.; Nagata, T.; Tsukuda, T., EXAFS study on interfacial structure between Pd cluster and n-octadecanethiolate monolayer: formation of mixed Pd–S interlayer. *Chem. Phys. Lett.* **2003**, *376*, 26-32.
177. Love, J. C.; Wolfe, D. B.; Haasch, R.; Chabinyc, M. L.; Paul, K. E.; Whitesides, G. M.; Nuzzo, R. G., Formation and Structure of Self-Assembled Monolayers of Alkanethiolates on Palladium. *J. Am. Chem. Soc.* **2003**, *125*, 2597-2609.
178. Love, J. C.; Wolfe, D. B.; Chabinyc, M. L.; Paul, K. E.; Whitesides, G. M., Self-Assembled Monolayers of Alkanethiolates on Palladium Are Good Etch Resists. *J. Am. Chem. Soc.* **2002**, *124*, 1576-1577.
179. Yang, Z.; Smetana, A. B.; Sorensen, C. M.; Klabunde, K. J., Synthesis and Characterization of a New Tiara Pd(II) Thiolate Complex, $[Pd(SC_{12}H_{25})_2]_6$, and Its Solution-Phase Thermolysis to Prepare Nearly Monodisperse Palladium Sulfide Nanoparticles. *Inorg. Chem.* **2007**, *46*, 2427-2431.
180. Sakai, N.; Tatsuma, T., One-step synthesis of glutathione-protected metal (Au, Ag, Cu, Pd, and Pt) cluster powders. *Journal of Materials Chemistry A* **2013**, *1*, 5915-5922.
181. Choudary, B. M.; Kumar, K. R.; Jamil, Z.; Thyagarajan, G., A novel 'anchored' palladium(II) phosphinated montmorillonite: the first example in the interlamellars of smectite clay. *J. Chem. Soc., Chem. Commun.* **1985**, 931-932.
182. Kumar, G.; Blackburn, J. R.; Albridge, R. G.; Moddeman, W. E.; Jones, M. M., Photoelectron spectroscopy of coordination compounds. II. Palladium complexes. *Inorg. Chem.* **1972**, *11*, 296-300.
183. Sleigh, C.; Pijpers, A. P.; Jaspers, A.; Coussens, B.; Meier, R. J., On the determination of atomic charge via ESCA including application to organometallics. *J. Electron. Spectrosc. Relat. Phenom.* **1996**, *77*, 41-57.
184. Zhang, P.; Sham, T. K., X-Ray Studies of the Structure and Electronic Behavior of Alkanethiolate-Capped Gold Nanoparticles: The Interplay of Size and Surface Effects. *Phys. Rev. Lett.* **2003**, *90*, 245502.
185. Moriarty, P., Comment on ``X-Ray Studies of the Structure and Electronic Behavior of Alkanethiolate-Capped Gold Nanoparticles: The Interplay of Size and Surface Effects''. *Phys. Rev. Lett.* **2004**, *92*, 109601.
186. Zhang, P.; Sham, T. K., Zhang and Sham Reply. *Phys. Rev. Lett.* **2004**, *92*, 109602.
187. Tanaka, A.; Takeda, Y.; Imamura, M.; Sato, S., Dynamic final-state effect on the Au ***4f*** core-level photoemission of dodecanethiolate-passivated Au nanoparticles on graphite substrates. *Physical Review B* **2003**, *68*, 195415.
188. Tanaka, A.; Takeda, Y.; Nagasawa, T.; Takahashi, K., Chemical states of dodecanethiolate-passivated Au

nanoparticles: synchrotron-radiation photoelectron spectroscopy. *Solid State Commun.* **2003**, *126*, 191-196.
189. Ghijsen, J.; Tjeng, L. H.; van Elp, J.; Eskes, H.; Westerink, J.; Sawatzky, G. A.; Czyzyk, M. T., Electronic structure of Cu_2O and CuO. *Physical Review B* **1988**, *38*, 11322-11330.
190. Ganguly, A.; Chakraborty, I.; Udayabhaskararao, T.; Pradeep, T., A copper cluster protected with phenylethanethiol. *J. Nanopart. Res.* **2013**, *15*, 1522.
191. Corthey, G.; Rubert, A. A.; Picone, A. L.; Casillas, G.; Giovanetti, L. J.; Ramallo-López, J. M.; Zelaya, E.; Benitez, G. A.; Requejo, F. G.; José-Yacamán, M., et al., New Insights into the Chemistry of Thiolate-Protected Palladium Nanoparticles. *J. Phys. Chem. C* **2012**, *116*, 9830-9837.
192. Chen, S.; Ingram, R. S.; Hostetler, M. J.; Pietron, J. J.; Murray, R. W.; Schaaff, T. G.; Khoury, J. T.; Alvarez, M. M.; Whetten, R. L., Gold Nanoelectrodes of Varied Size: Transition to Molecule-Like Charging. *Science* **1998**, *280*, 2098-2101.
193. Brust, M.; Walker, M.; Bethell, D.; Schiffrin, D. J.; Whyman, R., Synthesis of Thiol-Derivatised Gold Nanoparticles in a Two-Phase Liquid-Liquid System. *J. Chem. Soc., Chem. Commun.* **1994**, 801-802.
194. Fernando, A.; Weerawardene, K. L. D. M.; Karimova, N. V.; Aikens, C. M., Quantum Mechanical Studies of Large Metal, Metal Oxide, and Metal Chalcogenide Nanoparticles and Clusters. *Chem. Rev.* **2015**, *115*, 6112-6216.
195. Walter, M.; Akola, J.; Lopez-Acevedo, O.; Jadzinsky, P. D.; Calero, G.; Ackerson, C. J.; Whetten, R. L.; Grönbeck, H.; Häkkinen, H., A Unified View of Ligand-Protected Gold Clusters as Superatom Complexes. *Proc. Natl. Acad. Sci. U.S.A* **2008**, *105*, 9157-9162.
196. Link, S.; El-Sayed, M. A.; Gregory Schaaff, T.; Whetten, R. L., Transition from Nanoparticle to Molecular Behavior: A Femtosecond Transient Absorption Study of A Size-Selected 28 atom Gold Cluster. *Chem. Phys. Lett.* **2002**, *356*, 240-246.
197. Cleveland, C. L.; Landman, U.; Shafigullin, M. N.; Stephens, P. W.; Whetten, R. L., Structural Evolution of Larger Gold Clusters. *Z. Phys. D* **1997**, *40*, 503-508.
198. Price, R. C.; Whetten, R. L., All-Aromatic, Nanometer-Scale, Gold-Cluster Thiolate Complexes. *J. Am. Chem. Soc.* **2005**, *127*, 13750-13751.
199. Daniel, M.-C.; Astruc, D., Gold Nanoparticles: Assembly, Supramolecular Chemistry, Quantum-Size-Related Properties, and Applications toward Biology, Catalysis, and Nanotechnology. *Chem. Rev.* **2004**, *104*, 293-346.
200. Du, Y.; Sheng, H.; Astruc, D.; Zhu, M., Atomically Precise Noble Metal Nanoclusters as Efficient Catalysts: A Bridge between Structure and Properties. *Chem. Rev.* **2020**, *120*, 526-622.
201. Liu, H.; Hong, G.; Luo, Z.; Chen, J.; Chang, J.; Gong, M.; He, H.; Yang, J.; Yuan, X.; Li, L., et al., Atomic-Precision Gold Clusters for NIR-II Imaging. *Adv. Mater.* **2019**, *31*, 1901015.
202. Nimmala, P. R.; Yoon, B.; Whetten, R. L.; Landman, U.; Dass, A., $Au_{67}(SR)_{35}$ Nanomolecules: Characteristic Size-Specific Optical, Electrochemical, Structural Properties and First-Principles Theoretical Analysis. *J. Phys. Chem. A* **2013**, *117*, 504-517.
203. Jimenez, V. L.; Leopold, M. C.; Mazzitelli, C.; Jorgenson, J. W.; Murray, R. W., HPLC of Monolayer-Protected Gold Nanoclusters. *Anal. Chem.* **2003**, *75*, 199-206.
204. Negishi, Y.; Sakamoto, C.; Ohyama, T.; Tsukuda, T., Synthesis and the Origin of the Stability of Thiolate-Protected Au_{130} and Au_{187} Clusters. *J. Phys. Chem. Lett.* **2012**, *3*, 1624-1628.
205. Black, D. M.; Robles, G.; Bach, S. B. H.; Whetten, R. L., Gold Nanocluster Prospecting via Capillary Liquid Chromatography-Mass Spectrometry: Discovery of Three Quantized Gold Clusters in a Product Mixture of "2 nm Gold Nanoparticles". *Ind. Eng. Chem. Res.* **2018**, *57*, 5378-5384.
206. Knoppe, S.; Vogt, P., HPLC of Monolayer-Protected Gold Clusters with Baseline Separation. *Anal. Chem.* **2019**, *91*, 1603-1609.
207. Black, D. M.; Bhattarai, N.; Bach, S. B. H.; Whetten, R. L., Selection and Identification of Molecular Gold Clusters at the Nano(gram) Scale: Reversed Phase HPLC–ESI–MS of a Mixture of Au-Peth MPCs. *J. Phys. Chem. Lett.* **2016**, *7*, 3199-3205.
208. Sugi, K. S.; Bhat, S.; Nag, A.; Ganesan, P.; Mahendranath, A.; Pradeep, T., Ligand Structure and Charge State-Dependent Separation of Monolayer Protected Au_{25} Clusters Using Non-Aqueous Reversed-Phase HPLC. *Analyst* **2020**, *145*, 1337-1345.
209. Wilcoxon, J. P.; Martin, J. E.; Provencio, P., Size Distributions of Gold Nanoclusters Studied by Liquid Chromatography. *Langmuir* **2000**, *16*, 9912-9920.
210. Wilcoxon, J. P.; Provencio, P., Etching and Aging Effects in Nanosize Au Clusters Investigated Using High-

Resolution Size-Exclusion Chromatography. *J. Phys. Chem. B* **2003**, *107*, 12949-12957.
211. Tsunoyama, H.; Negishi, Y.; Tsukuda, T., Chromatographic Isolation of "Missing" Au_{55} Clusters Protected by Alkanethiolates. *J. Am. Chem. Soc.* **2006**, *128*, 6036-6037.
212. Qian, H.; Zhu, Y.; Jin, R., Isolation of Ubiquitous $Au_{40}(SR)_{24}$ Clusters from the 8 kDa Gold Clusters. *J. Am. Chem. Soc.* **2010**, *132*, 4583-4585.
213. Tian, S.; Li, Y.-Z.; Li, M.-B.; Yuan, J.; Yang, J.; Wu, Z.; Jin, R., Structural Isomerism in Gold Nanoparticles Revealed by X-Ray Crystallography. *Nat. Commun.* **2015**, *6*, 8667.
214. Dainese, T.; Antonello, S.; Gascón, J. A.; Pan, F.; Perera, N. V.; Ruzzi, M.; Venzo, A.; Zoleo, A.; Rissanen, K.; Maran, F., $Au_{25}(SEt)_{18}$, a Nearly Naked Thiolate-Protected Au_{25} Cluster: Structural Analysis by Single Crystal X-ray Crystallography and Electron Nuclear Double Resonance. *ACS Nano* **2014**, *8*, 3904-3912.
215. Gautier, C.; Bürgi, T., Chiral N-Isobutyryl-cysteine Protected Gold Nanoparticles: Preparation, Size Selection, and Optical Activity in the UV−vis and Infrared. *J. Am. Chem. Soc.* **2006**, *128*, 11079-11087.
216. Desireddy, A.; Conn, B. E.; Guo, J.; Yoon, B.; Barnett, R. N.; Monahan, B. M.; Kirschbaum, K.; Griffith, W. P.; Whetten, R. L.; Landman, U., et al., Ultrastable Silver Nanoparticles. *Nature* **2013**, *501*, 399-402.
217. Negishi, Y.; Hashimoto, S.; Ebina, A.; Hamada, K.; Hossain, S.; Kawawaki, T., Atomic-level Separation of Thiolate-Protected Metal Clusters. *Nanoscale* **2020**, *12*, 8017-8039.
218. Black, D. M.; Robles, G.; Lopez, P.; Bach, S. B. H.; Alvarez, M.; Whetten, R. L., Liquid Chromatography Separation and Mass Spectrometry Detection of Silver-Lipoate $Ag_{29}(LA)_{12}$ Nanoclusters: Evidence of Isomerism in the Solution Phase. *Anal. Chem.* **2018**, *90*, 2010-2017.
219. Barth, H. G.; Boyes, B. E.; Jackson, C., Size Exclusion Chromatography. *Anal. Chem.* **1996**, *68*, 445-466.
220. Barth, H. G.; Boyes, B. E.; Jackson, C., Size Exclusion Chromatography and Related Separation Techniques. *Anal. Chem.* **1998**, *70*, 251-278.
221. Bio-Beads S-X Resin, Biorad laboratories (http://www.biorad.com/webroot/web/pdf/lsr/literature/LIT263.pdf).
222. Avouris, P., Manipulation of Matter at the Atomic and Molecular Levels. *Acc. Chem. Res.* **1995**, *28*, 95-102.
223. Eswaramoorthy, S. K.; Dass, A., Digestive ripening yields atomically precise Au nanomolecules. *New J. Chem.* **2021**, *45*, 20241-20248.
224. Dass, A.; Holt, K.; Parker, J. F.; Feldberg, S. W.; Murray, R. W., Mass Spectrometrically Detected Statistical Aspects of Ligand Populations in Mixed Monolayer $Au_{25}L_{18}$ Nanoparticles. *J. Phys. Chem. C* **2008**, *112*, 20276-20283.
225. Eswaramoorthy, S. K.; Sakthivel, N. A.; Dass, A., Core Size Conversion of $Au_{329}(SCH_2CH_2Ph)_{84}$ to $Au_{279}(SPh\text{-}tBu)_{84}$ Nanomolecules. *J. Phys. Chem. C* **2019**, *123*, 9634-9639.
226. Qian, H.; Jin, R., Controlling Nanoparticles with Atomic Precision: The Case of $Au_{144}(SCH_2CH_2Ph)_{60}$. *Nano Lett.* **2009**, *9*, 4083-4087.
227. Wijesinghe, K. H.; Sakthivel, N. A.; Sementa, L.; Yoon, B.; Fortunelli, A.; Landman, U.; Dass, A., Nanomolecular Metallurgy: Transformation from $Au_{144}(SCH_2CH_2Ph)_{60}$ to $Au_{279}(SPh\text{-}t\text{Bu})_{84}$. *J. Phys. Chem. C* **2021**, *125*, 20488-20502.

LIST OF APPENDICES

APPENDIX A: SUPPLEMENTARY INFORMATION FOR CHAPTER 2

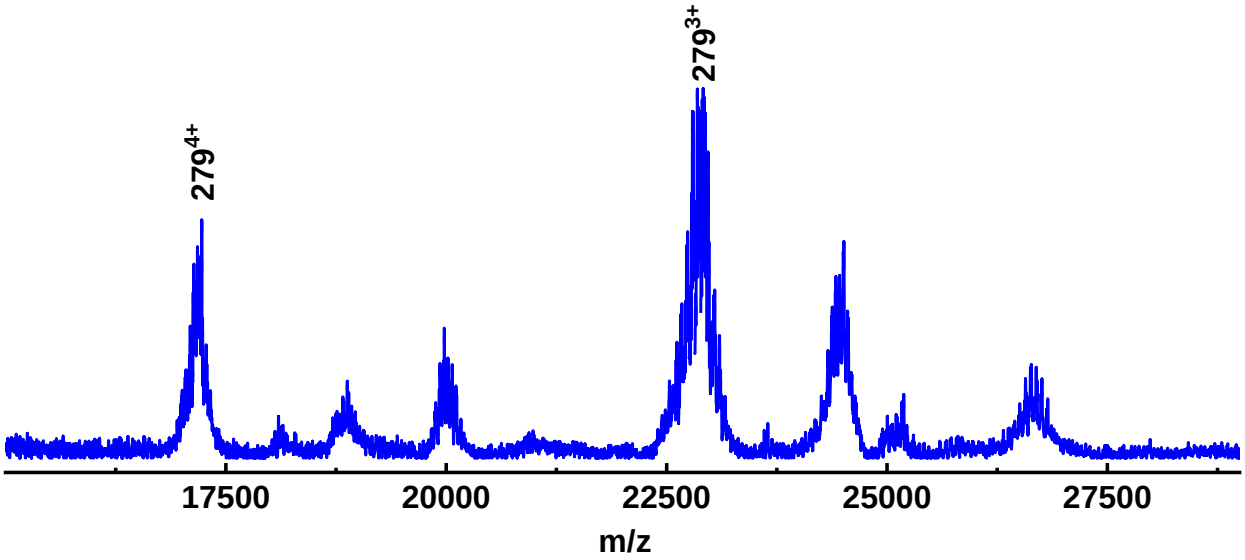

Figure S2.1. ESI-MS spectra of 2 days sample showing 3+ and 4+ of reaction progress

Table S2.1. ESI-MS peak values for Figure 3 inset.

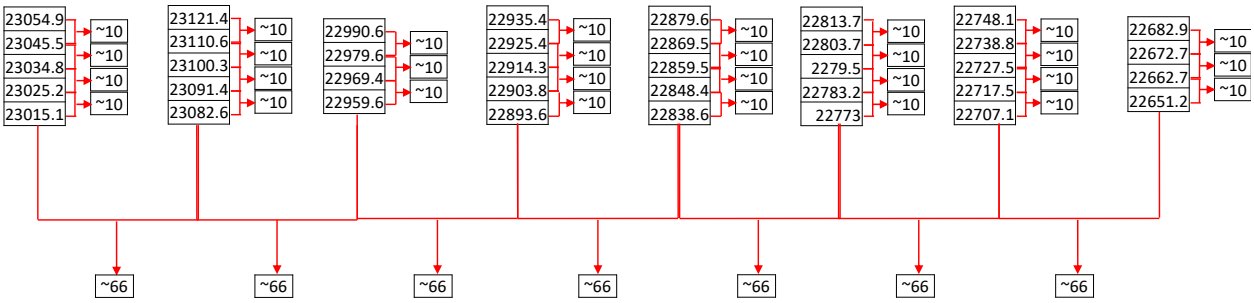

APPENDIX B: SUPPLEMENTARY INFORMATION FOR CHAPTER 3

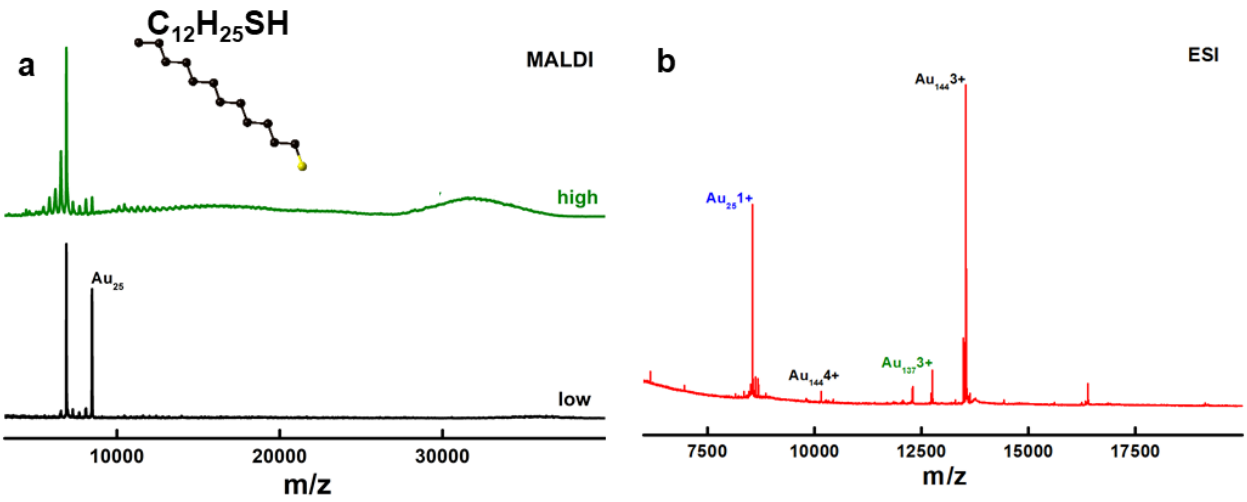

Figure S3.1. Dodecanethiol protected atomically precise gold nanomolecules synthesized using digestive ripening method. a) MALDI-MS data showing high (green) and low (black) laser. (b) ESI-MS data showing the presence of Au_{144}, Au_{137} and Au_{25} species in the product.

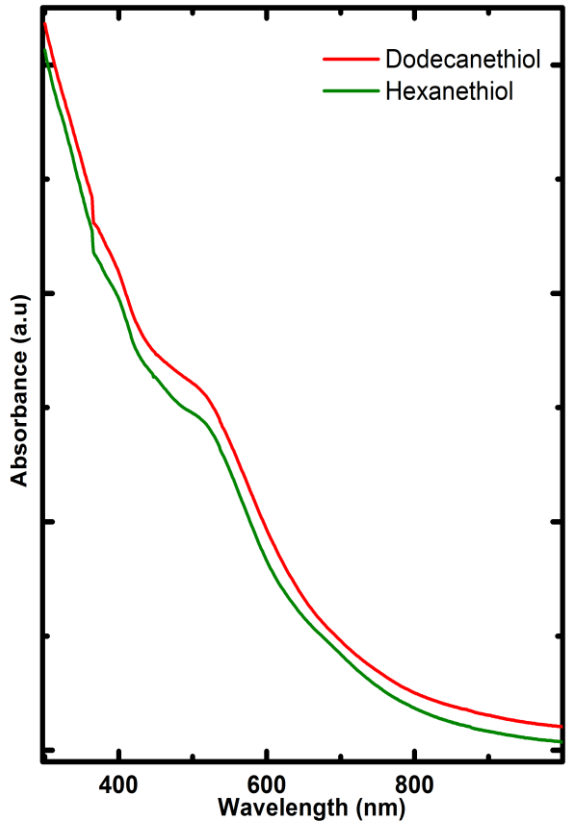

Figure S3.2. UV-visible plot of the digestive ripening synthesis products protected by hexanethiol and dodecanethiol.

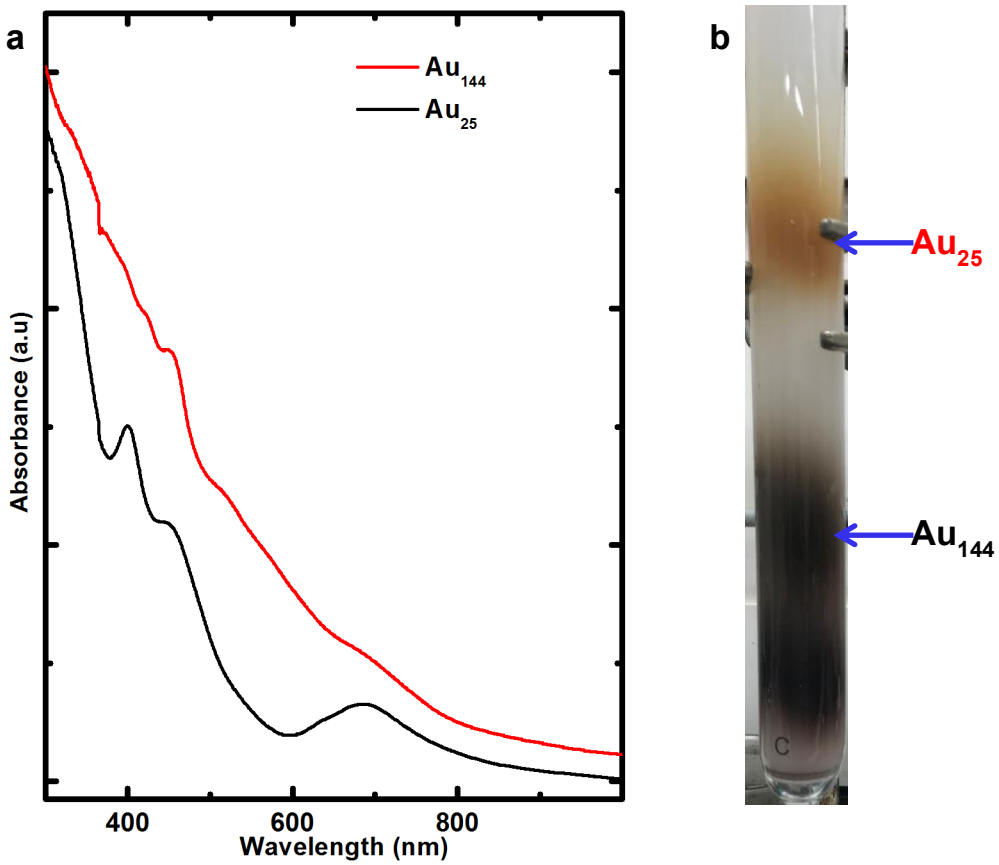

Figure S3.3. Hexanethiol protected gold nanomolecules a) UV-visible plot of $Au_{144}(SR)_{60}$ (with $Au_{137}(SR)_{54}$) and $Au_{25}(SR)_{18}$ after SEC separation. b) Photograph of the SEC column separation performed on final product of digestive ripening synthesis.

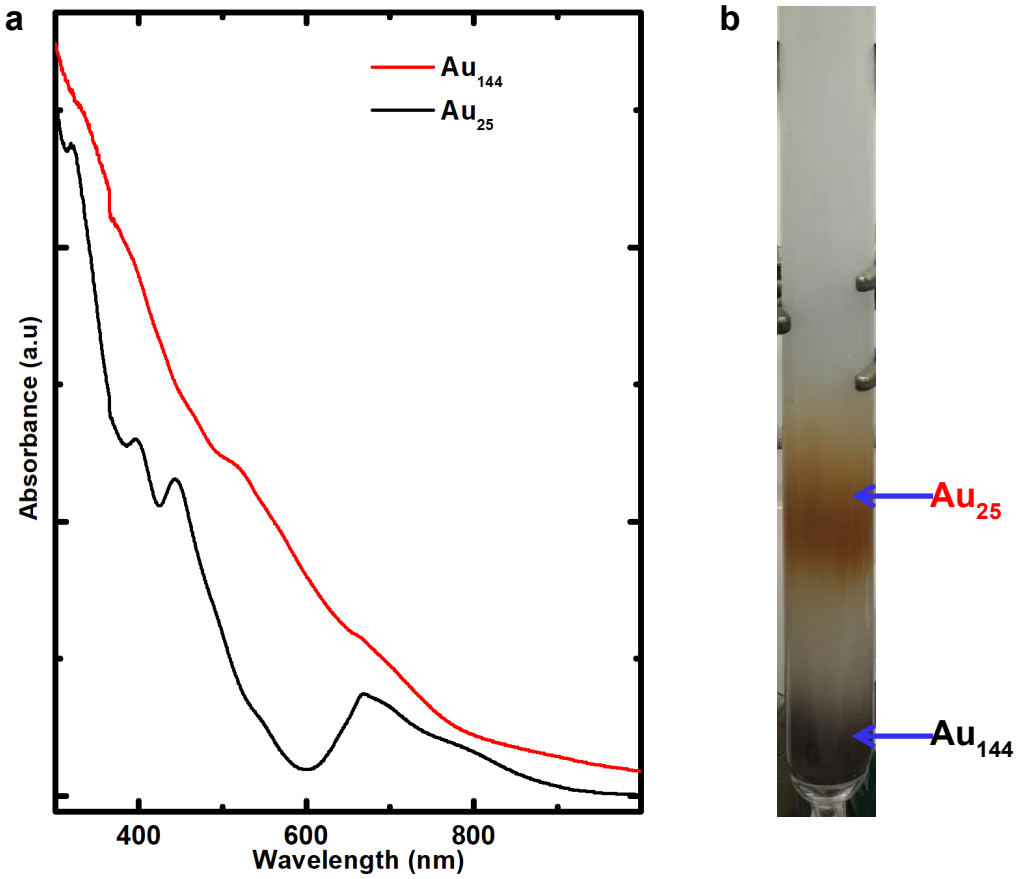

Figure S3.4. Dodecanethiol protected gold nanomolecules a) UV-visible plot of $Au_{144}(SR)_{60}$ (with $Au_{137}(SR)_{54}$) and $Au_{25}(SR)_{18}$ after SEC separation. b) Photograph of the SEC column separation performed on final product of digestive ripening synthesis.

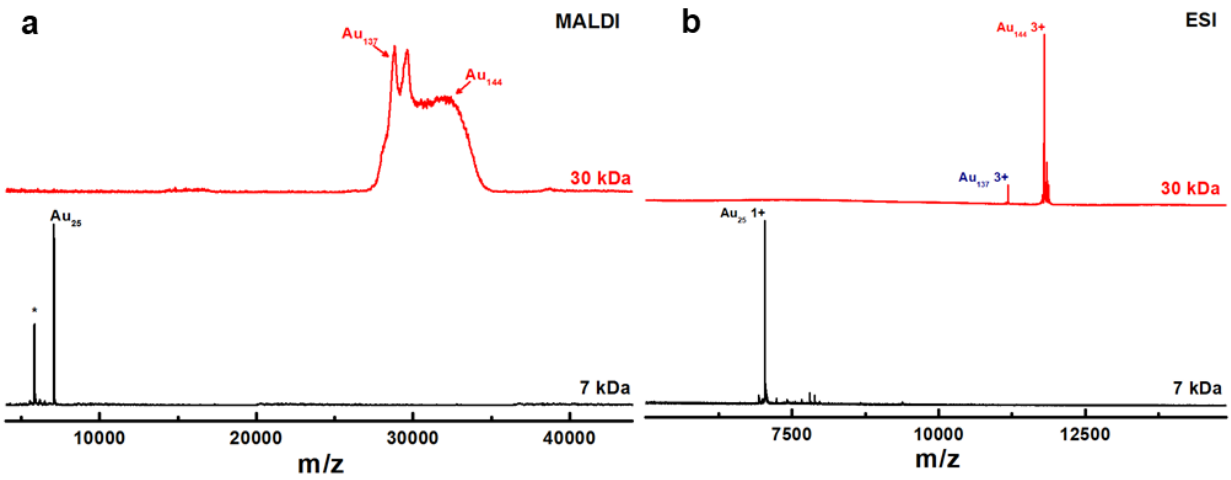

Figure S3.5. Hexanethiol protected gold nanomolecules after SEC a) MALDI-MS spectra showing 30 kDa species ($Au_{144}(SR)_{60}$ & $Au_{137}(SR)_{54}$) and $Au_{25}(SR)_{18}$ (7 kDa). b) ESI-MS spectra showing 30 kDa species ($Au_{144}(SR)_{60}$ & $Au_{137}(SR)_{54}$) and $Au_{25}(SR)_{18}$ (7 kDa). * Fragment peak.

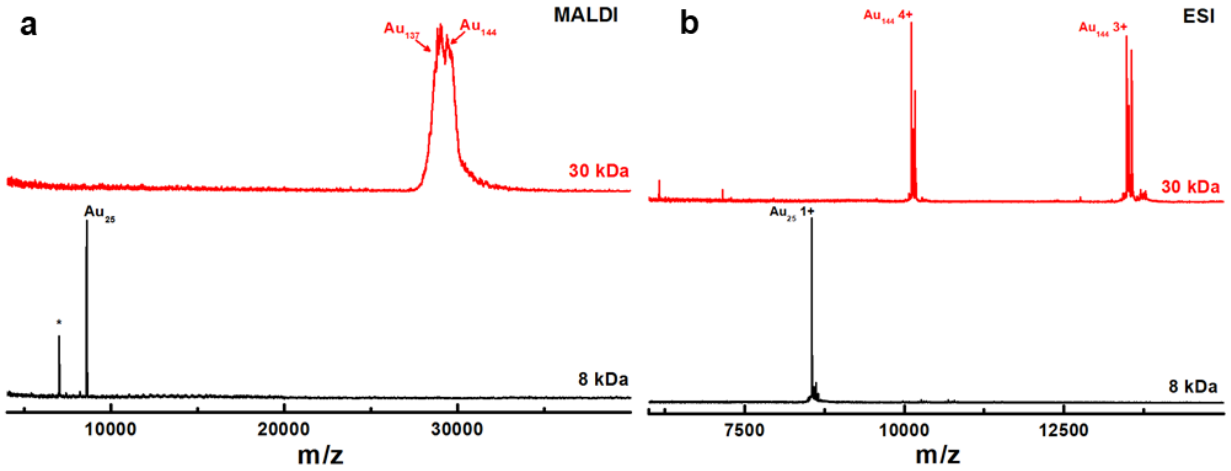

Figure S3.6. Dodecanethiol protected gold nanomolecules after SEC separation a) MALDI-MS spectra showing 30 kDa species ($Au_{144}(SR)_{60}$ & $Au_{137}(SR)_{54}$) and $Au_{25}(SR)_{18}$ (8 kDa). b) ESI-MS spectra showing 30 kDa species ($Au_{144}(SR)_{60}$ & $Au_{137}(SR)_{54}$) and $Au_{25}(SR)_{18}$ (8 kDa). * Fragment peak.

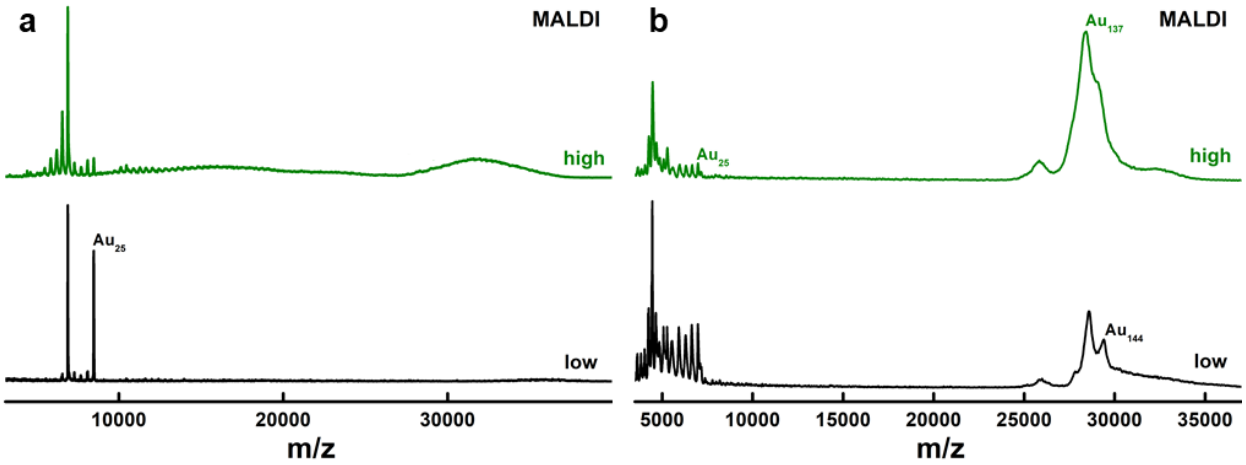

Figure S3.7. High (green) and low (black) laser MALDI-MS data of dodecanethiol protected gold nanomolecules comparing 2 methods (a) Digestive Ripening (b) Brust method

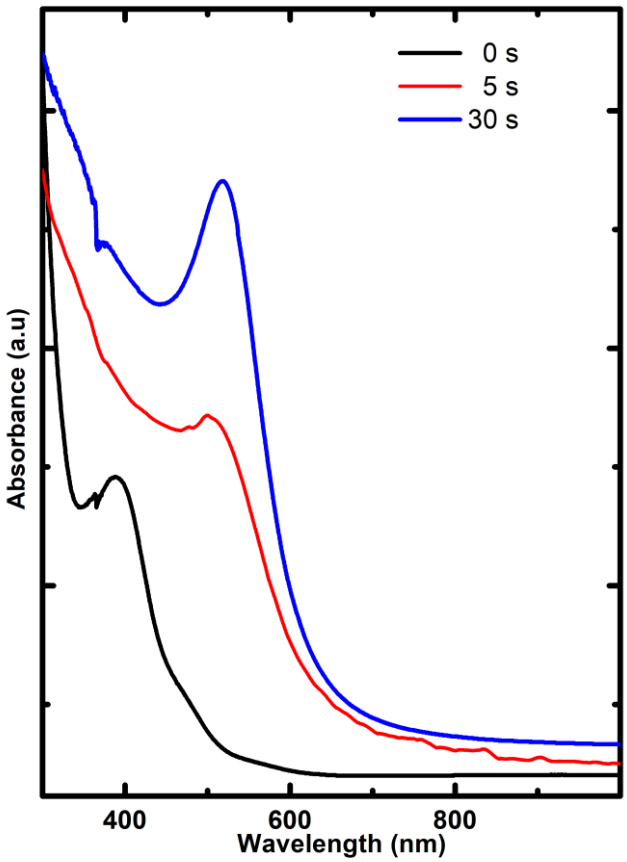

Figure S3.8. UV-visible spectroscopy of digestive ripening synthesis method at various reduction timings.

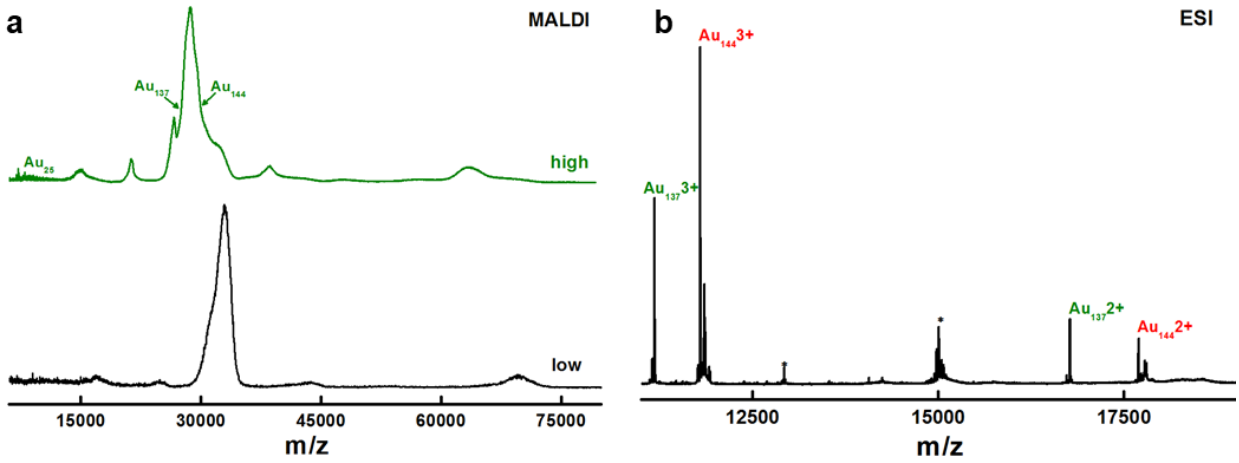

Figure S3.9. MALDI-MS and ESI-MS data of hexanethiol protected gold nanomolecules synthesized using digestive ripening synthesis method with ToABr as phase transfer agent. (* marked peaks are impurity from previous sample)

APPENDIX C: SUPPLEMENTARY INFORMATION FOR CHAPTER 4

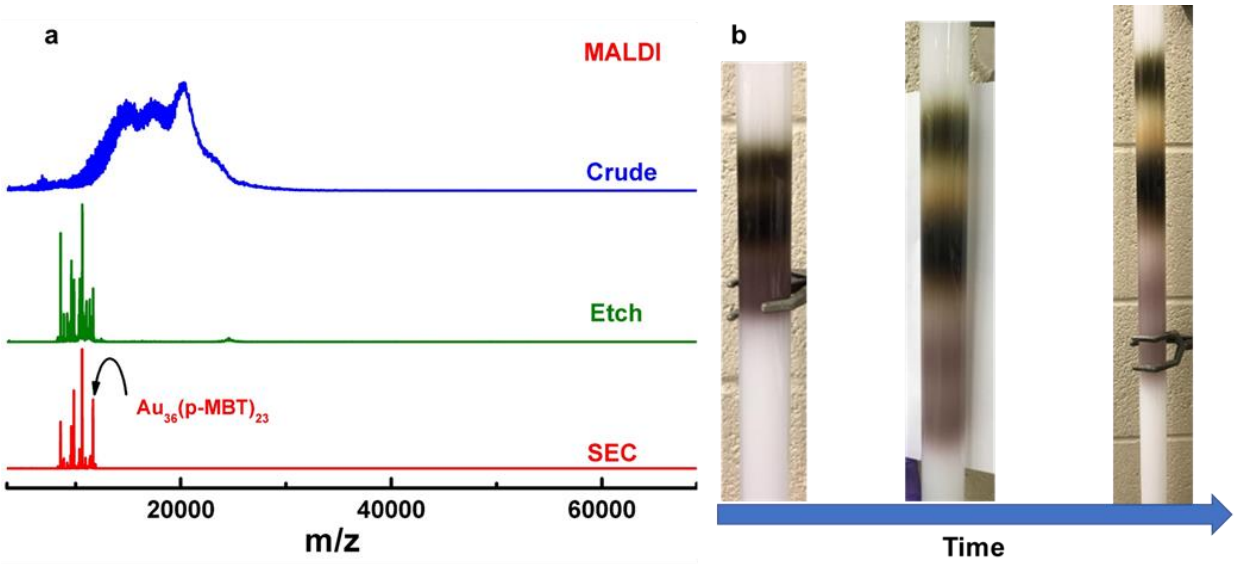

Figure S4.1. Synthesis and isolation of $Au_{36}(SPh\text{-}pCH_3)_{24}$ Nanomolecule (a) MALDI-MS Spectra of the synthesis and isolation process, Top (Blue) corresponds to crude product, followed mass spectra of thermochemical (etch) treated product for 2 hours (Green) and Bottom (Red) corresponds the final isolated $Au_{36}(SPh\text{-}pCH_3)_{24}$ product using SEC. (b) Images of the SEC process, as the time progress different color bands are seen belongs to different sizes. The top (Green) band in the rightmost image corresponds to the $Au_{36}(SR)_{24}$.

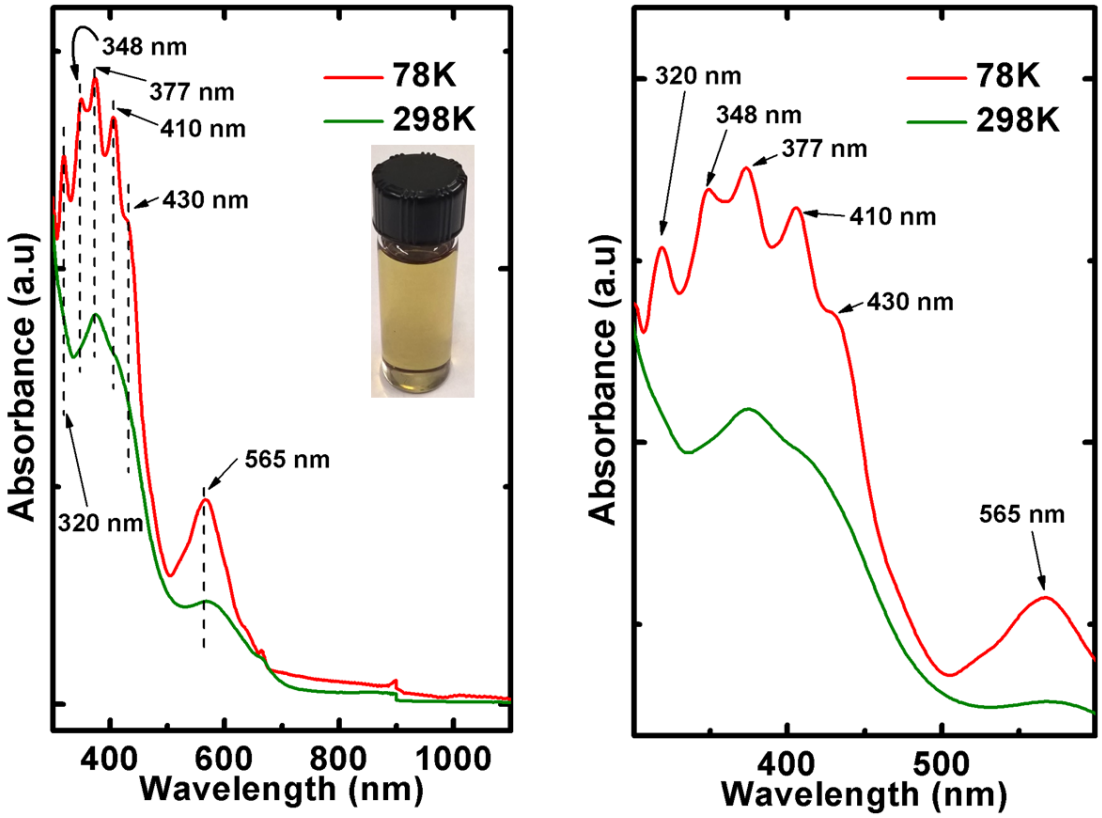

Figure S4.2. UV-visible absorpton spectra of $Au_{36}(SPh\text{-}pCH_3)_{24}$ NM in 2 different temperature 298 K (Green) and 78 K (Red).

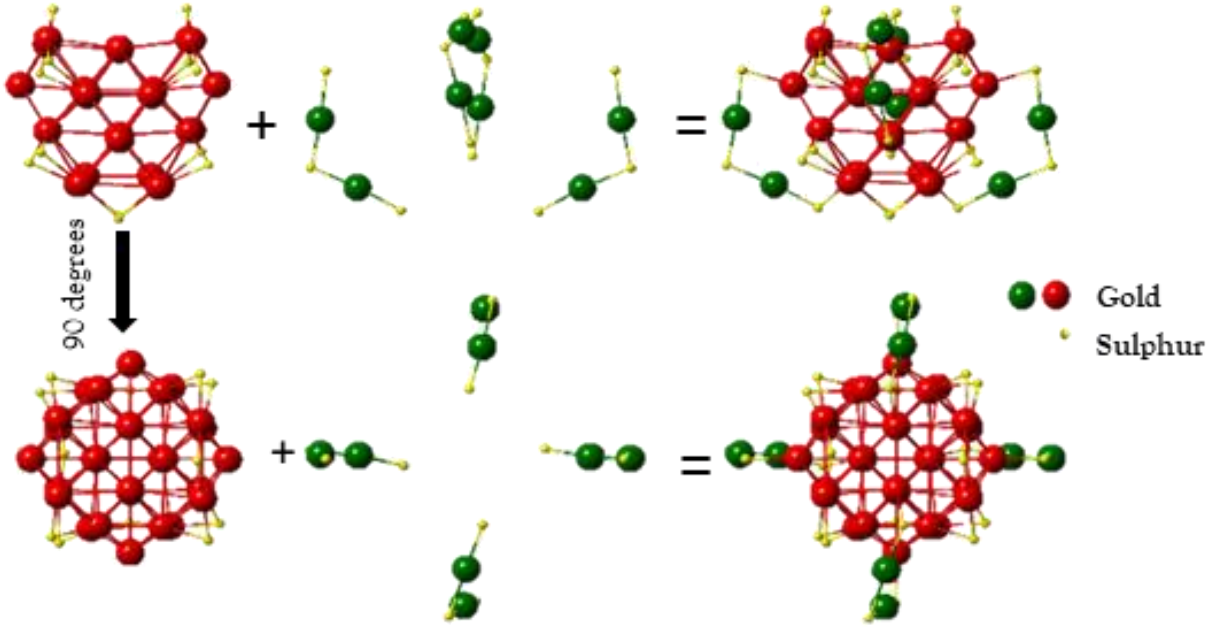

Figure S4.3. Core structure model of $Au_{36}(SPh\text{-}pCH_3)_{24}$ which has an Au_{28} kernel in the core with 4 dimeric staples attached to it. Top row represents how the dimeric staple is attached to the core Au atoms and the bottom row corresponds to a 90-degree rotation.

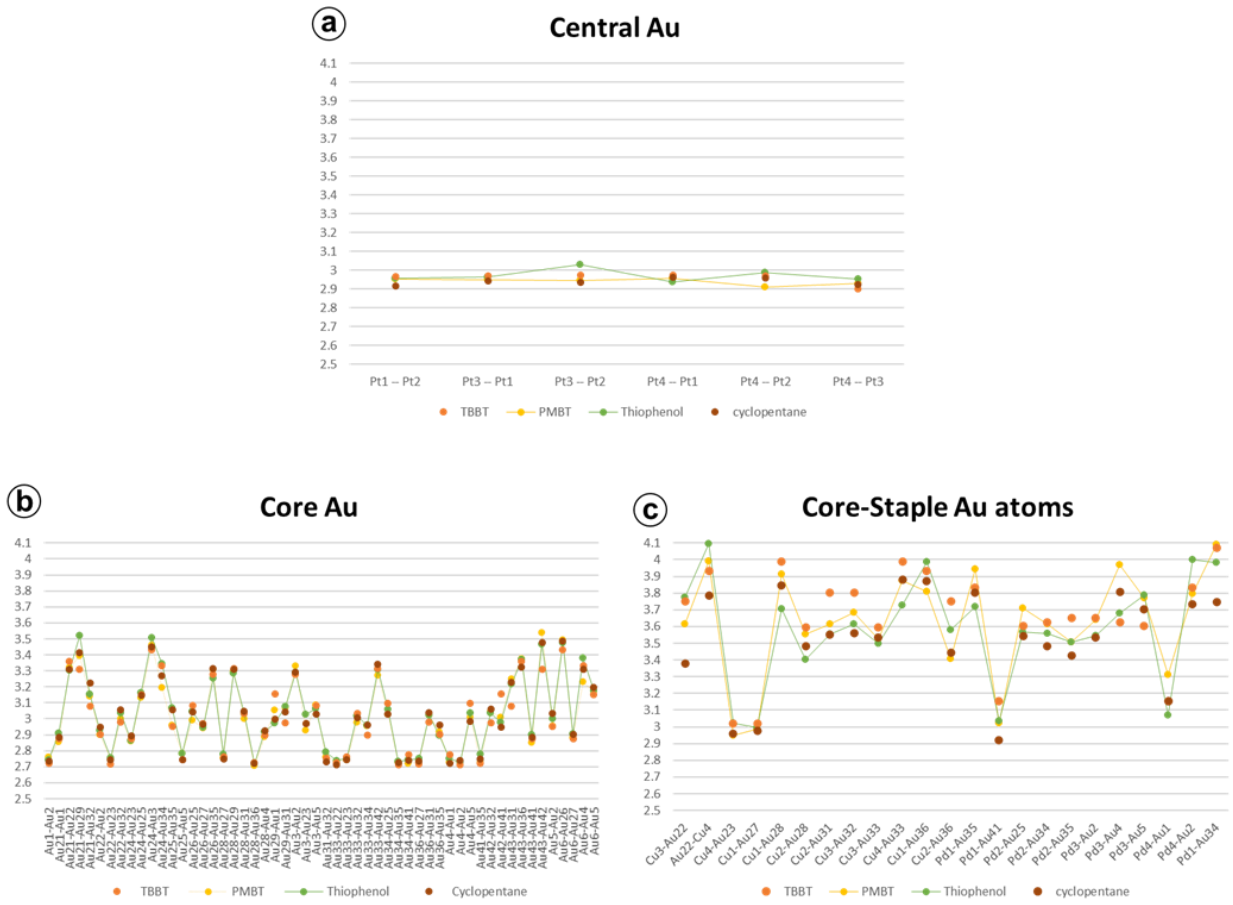

Figure S4.4. Au-Au bond distance comparison of four $Au_{36}(SR)_{24}$ (SR= SPh-*t*Bu, SPh, SC_5H_9, and SPh-*p*CH_3) structure, bond distance deviations between individual positions. a) all Au-Au bond distance between 4 central Au atoms. b) all Au-Au bond distance between 24 core Au atoms. c) all Au-Au bond distance between 24 core and 8 staple Au atoms.

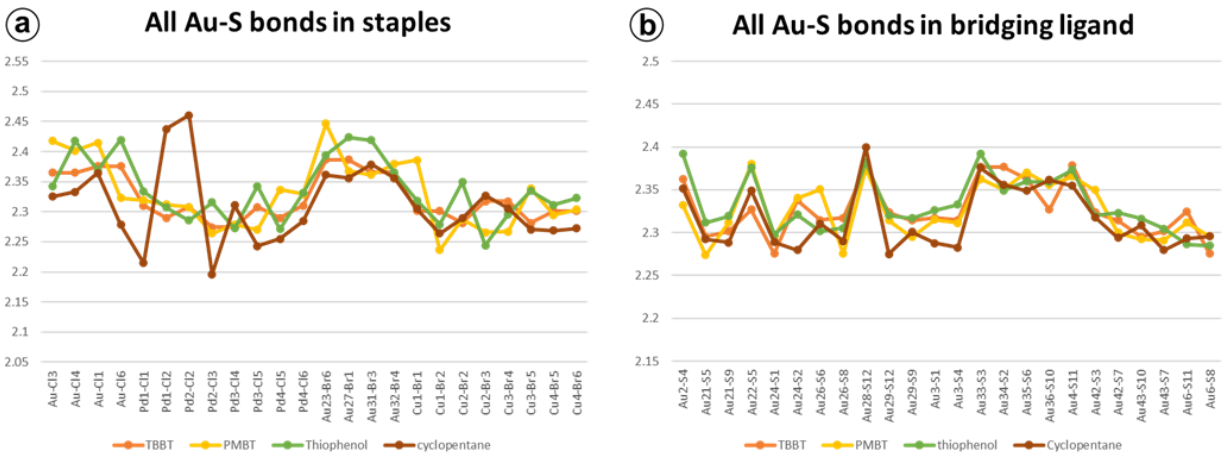

Figure S4.5. Au-S bond distance comparison of four $Au_{36}(SR)_{24}$ (SR= SPh-*t*Bu, SPh, SC_5H_9, and SPh-*p*CH_3) structure, bond distance deviations between individual positions. a) all Au-S bond distance in staples. b) all Au-S bond distances in bridging ligands.

APPENDIX D: SUPPLEMENTARY INFORMATION FOR CHAPTER 5

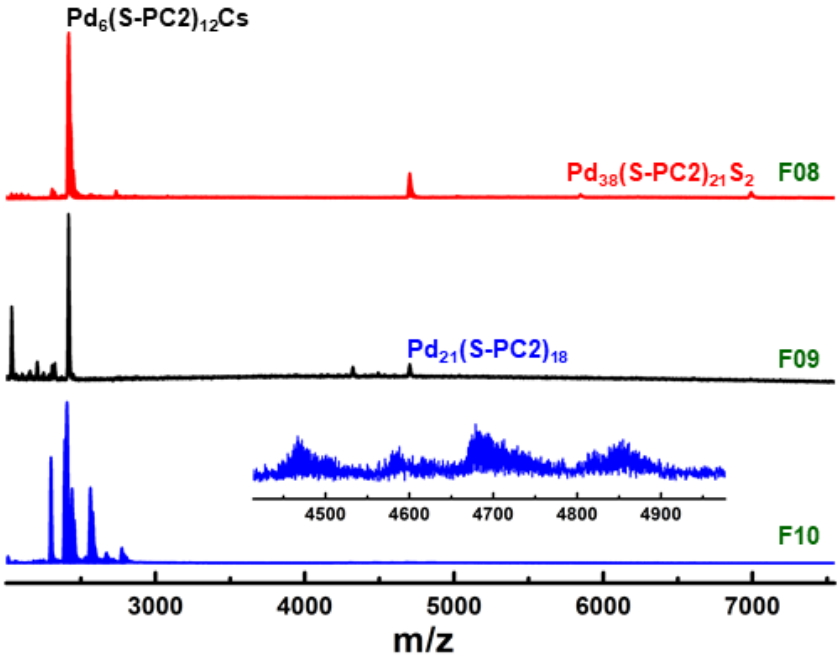

Figure S5.1. ESI-MS of Pd NCs comparing F08, F09 and F10.

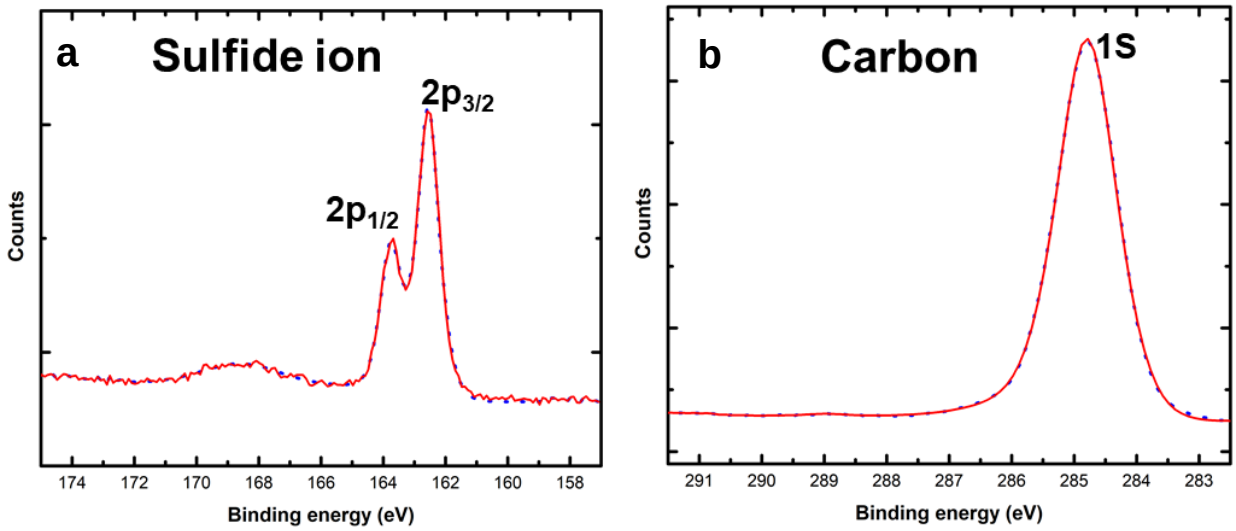

Figure S5.2. High resolution XPS spectrum focused on a) Sulfide and b) Carbon of SEC purified product of Pd nanoclusters protected by Phenyl ethane thiol.

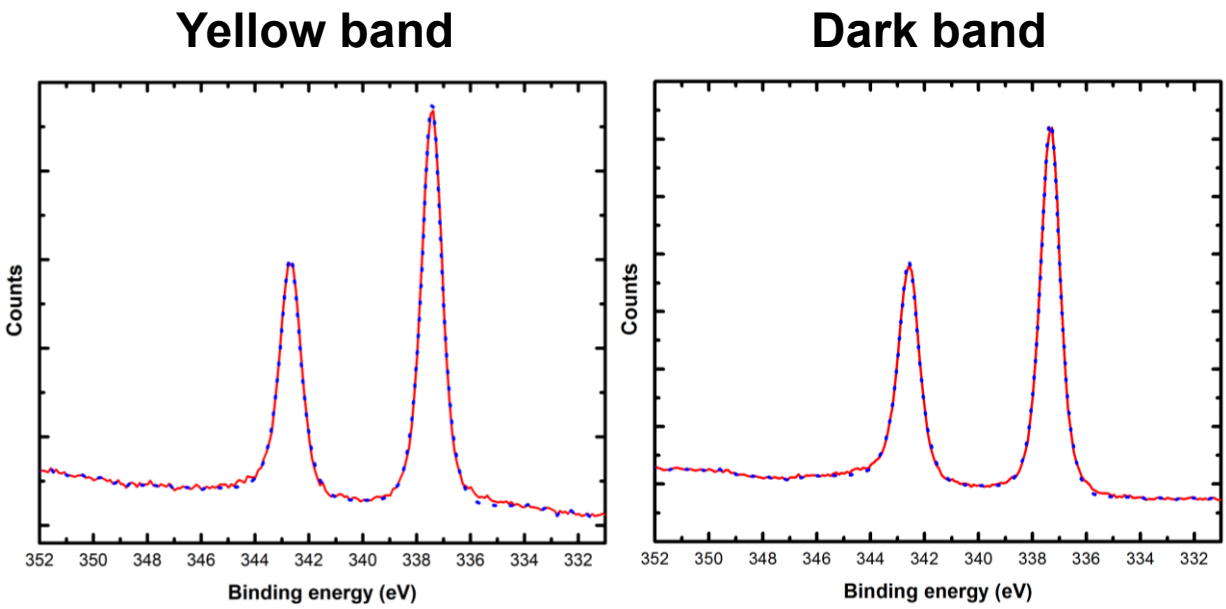

Figure S5.3. Pd $3d_{5/2}$ core level photoemission spectra comparison of yellow and dark bands.

APPENDIX C: SUPPLEMENTARY INFORMATION FOR CHAPTER 6

Figure S6.1. Time dependent photos of short SEC column during elution of etching product containing $Au_{30}(S\text{-}t\text{Bu})_{18}$ at 7514 Da, $Au_{46}(S\text{-}t\text{Bu})_{24}$ at 11200 Da and $Au_{65}(S\text{-}t\text{Bu})_{29}$ at 15389 Da.

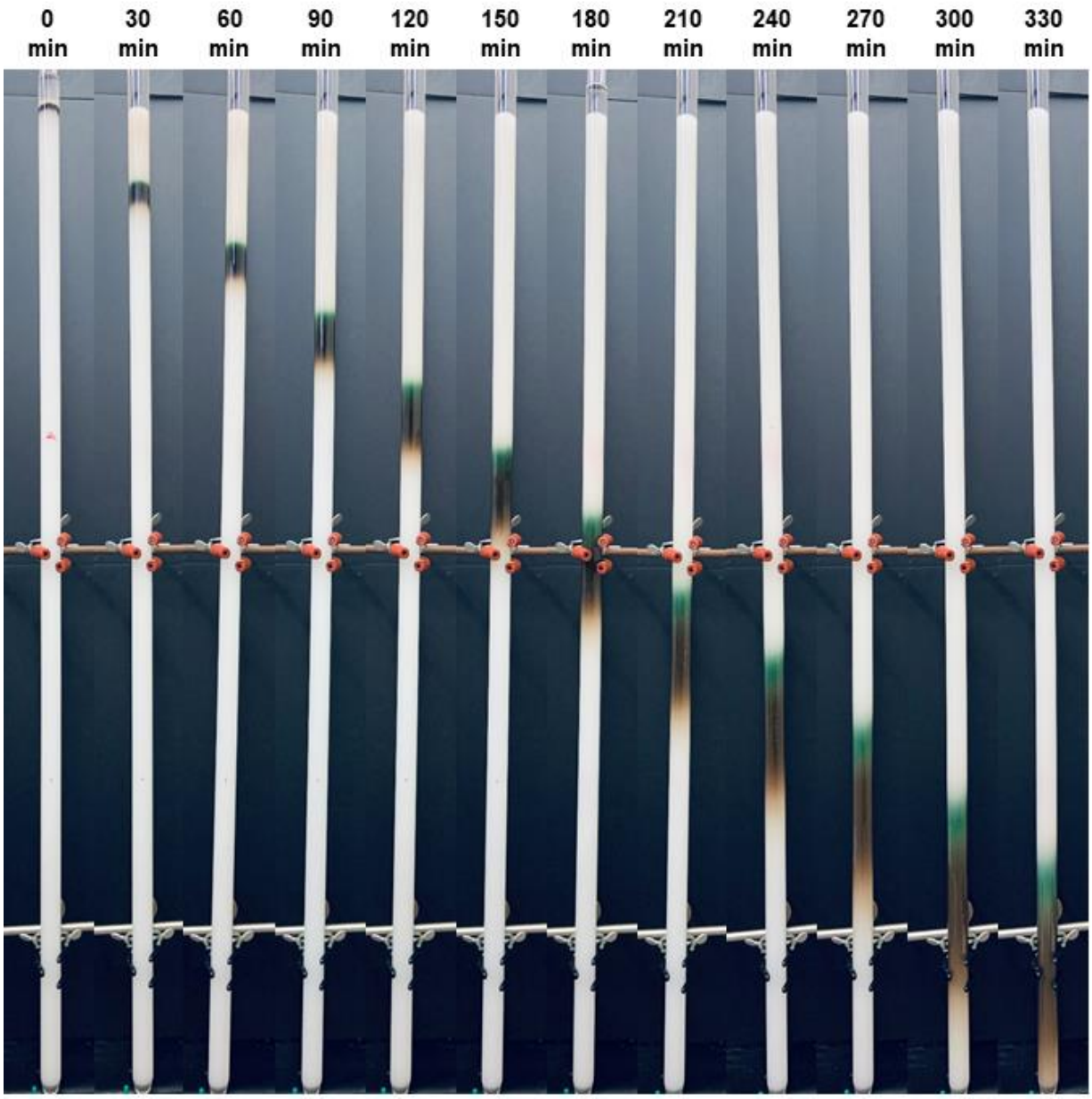

Figure S6.2. Time dependent photos of medium SEC column during elution of etching product containing $Au_{30}(S\text{-}t\text{Bu})_{18}$ at 7514 Da, $Au_{46}(S\text{-}t\text{Bu})_{24}$ at 11200 Da and $Au_{65}(S\text{-}t\text{Bu})_{29}$ at 15389 Da.

APPENDIX C: SUPPLEMENTARY INFORMATION FOR CHAPTER 7

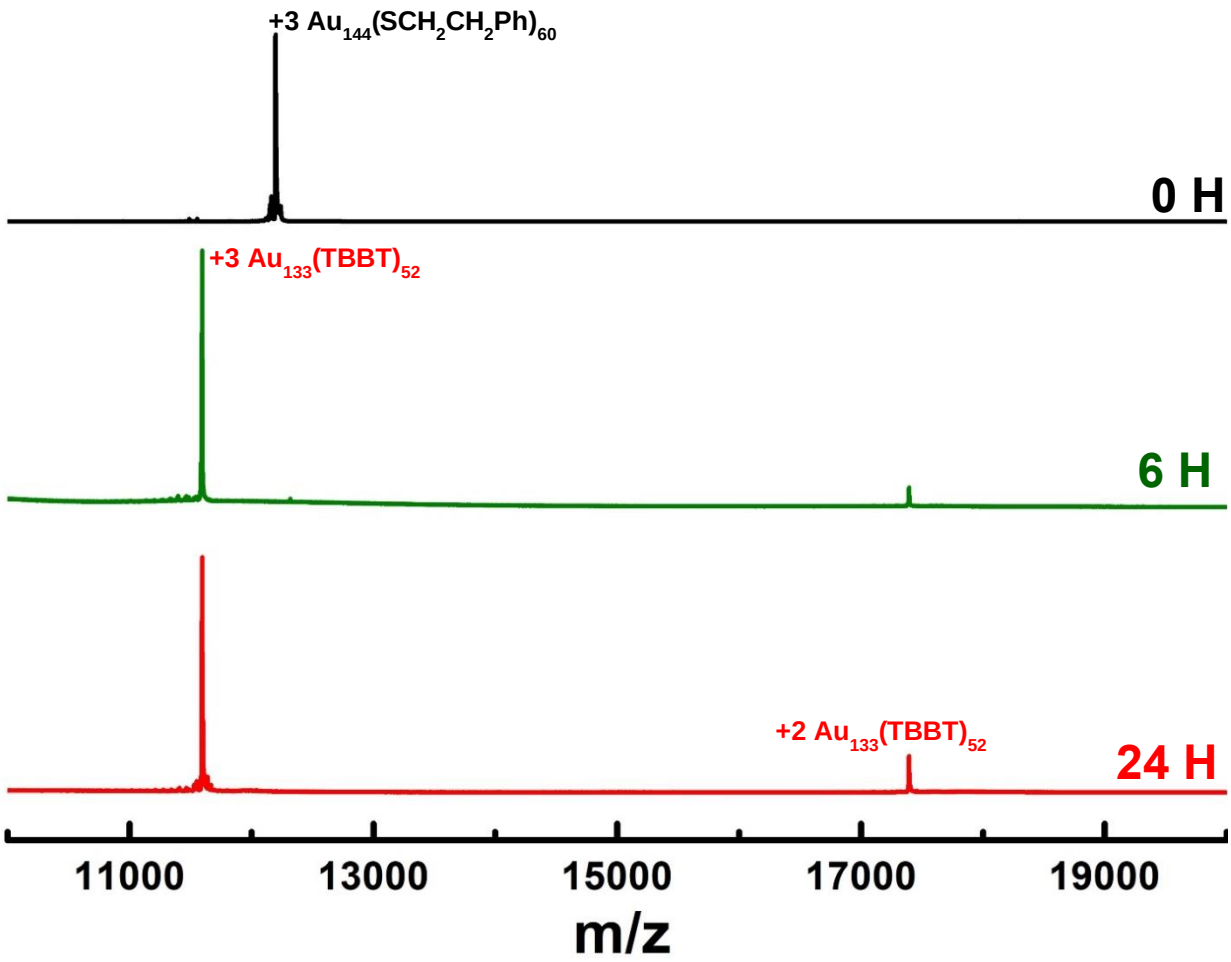

Figure S7.1. ESI-MS spectra of the starting $Au_{144}(SCH_2CH_2Ph)_{60}$ at 0 H, and its transformation to $Au_{133}(TBBT)_{52}$ upon reacting with TBBT at 80 ^{0}C.

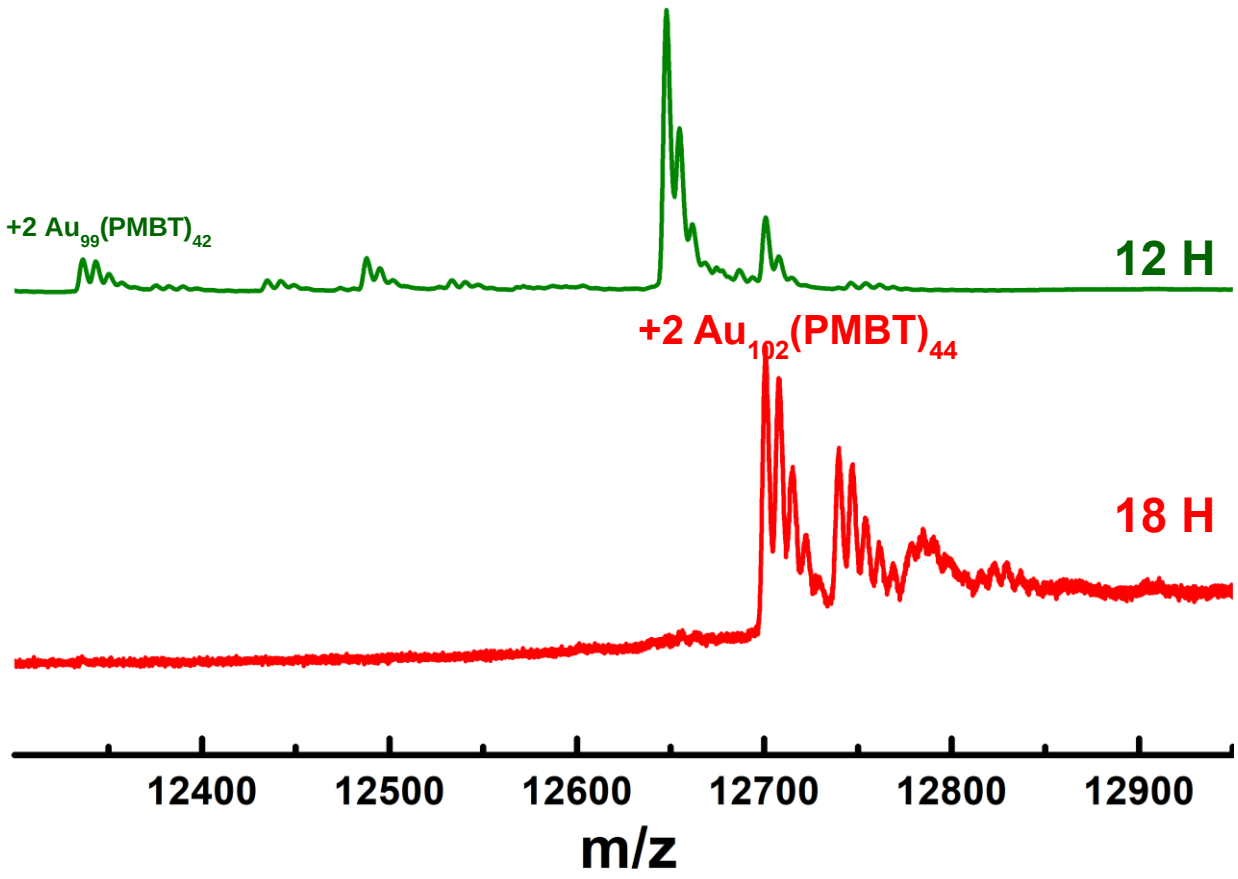

Figure S7.2. Expanded ESI-MS (12300 to 13000 Da) transformation spectra of $Au_{144}(SCH_2CH_2Ph)_{60}$ and its transformation to $Au_{99\text{-}102}(PMBT)_{42\text{-}44}$ and $Au_{130}(PMBT)_{150}$ upon reacting with PMBT ligand at 80 ^{0}C.

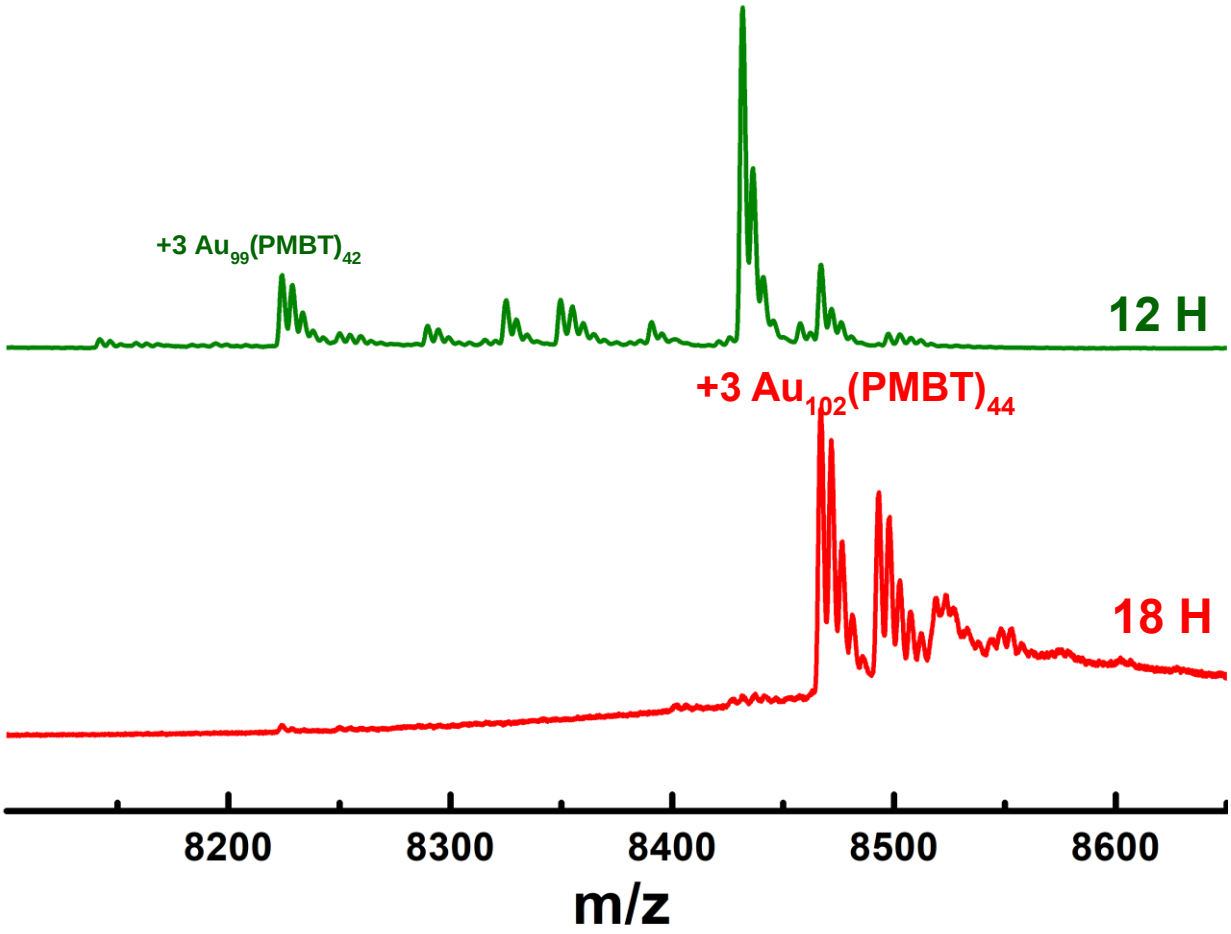

Figure S7.3. Expanded ESI-MS (8100 to 8650 Da) to 13000 Da) transformation spectra of $Au_{144}(SCH_2CH_2Ph)_{60}$ and its transformation to $Au_{99\text{-}102}(PMBT)_{42\text{-}44}$ and $Au_{130}(PMBT)_{150}$ upon reacting with PMBT ligand at 80 ^{0}C.

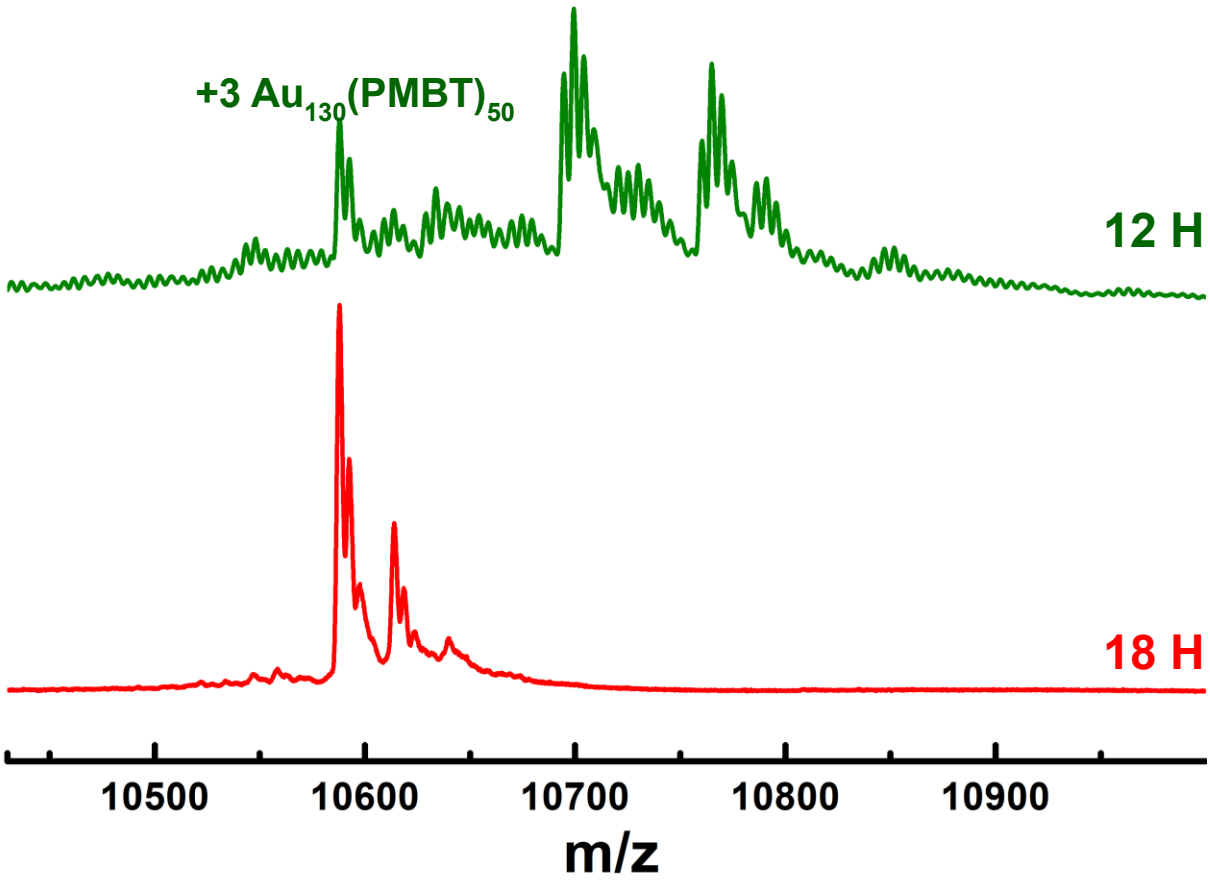

Figure S7.4. Expanded ESI-MS (10400 to 11000 Da) transformation spectra of $Au_{144}(SCH_2CH_2Ph)_{60}$ and its transformation to $Au_{99\text{-}102}(PMBT)_{42\text{-}44}$ and $Au_{130}(PMBT)_{150}$ upon reacting with PMBT ligand at 80 ^{0}C.

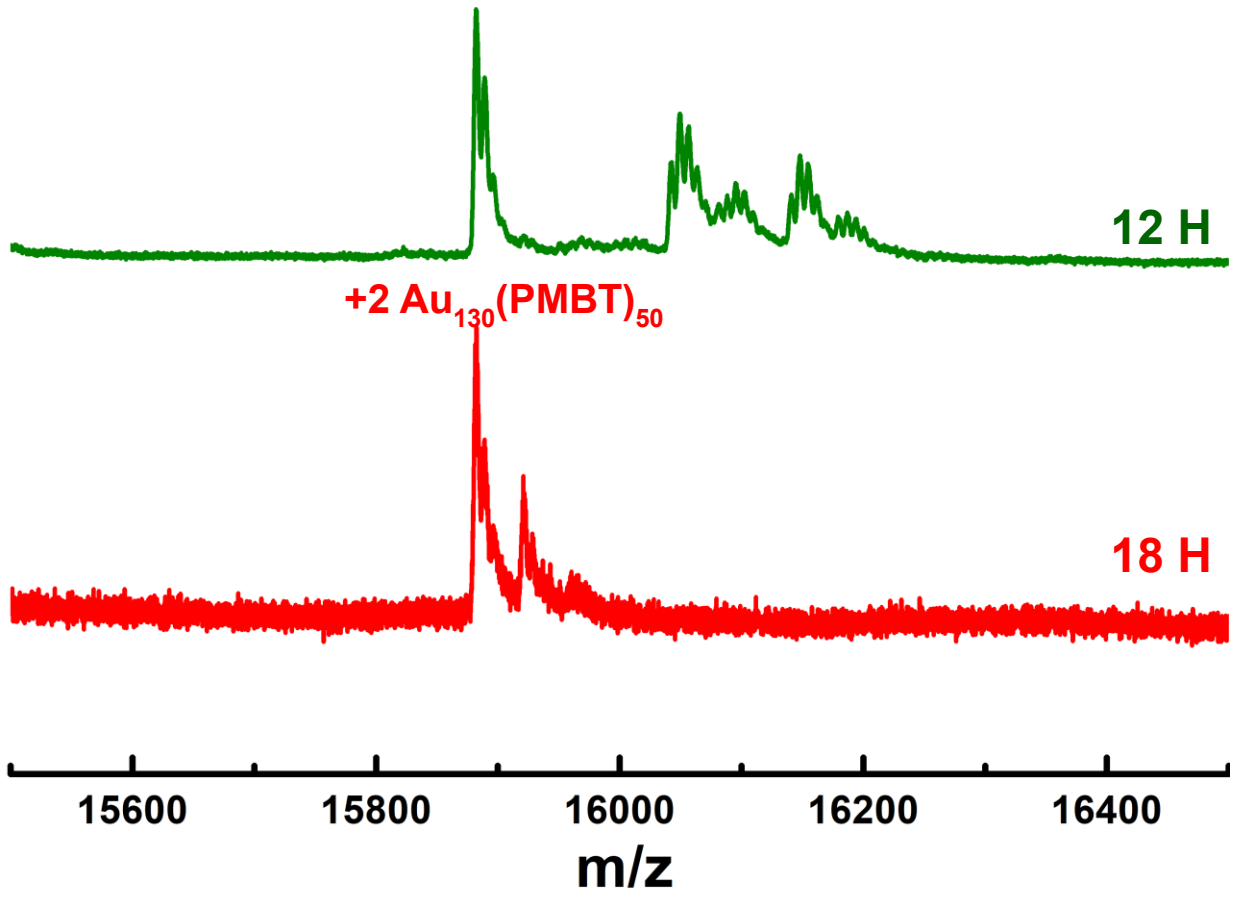

Figure S7.5. Expanded ESI-MS (12300 to 13000 Da) transformation spectra of $Au_{144}(SCH_2CH_2Ph)_{60}$ and its transformation to $Au_{99\text{-}102}(PMBT)_{42\text{-}44}$ and $Au_{130}(PMBT)_{150}$ upon reacting with PMBT ligand at 80 ^{0}C.

VITA

SENTHIL KUMAR ESWARAMOORTHY

Summary

- *Analytical chemist* and synthetic nanomaterials researcher with chemical and electrochemical engineering background having 3 years of industrial experience 4.5 years of research experience with a portfolio of 4 publications and 4 more in preparation.
- Developed best problem-solving skills through hands-on repairing of MALDI-MS instrument and working with various complex instruments daily.
- Excellent communicator with good team and time management skills in coordinating researchers, engineers, clients, and coworkers with diverse background.

Education

Ph. D., in Analytical Chemistry April 2022

University of Mississippi, MS.

B.Tech in Chemical and Electrochemical Engineering April 2014

CECRI, Anna University, India

Analytical instrument skills

ESI-TOF-MS including tandem-MS, triple quad, ion mobility ◆ MALDI-TOF-MS ◆ SEM ◆ TEM ◆ XPS ◆ UV-visible-NIR ◆ Single crystal XRD ◆ Size Exclusion Chromatography ◆ HPLC ◆ TLC

Technical skills

Method Development Quality Control Experiment Design Research & Development Troubleshooting Team Player Data Interpretation Problem-Solving Computer Skills Goal Oriented Professional Data Analysis Cost-Efficient All software's used in above mentioned analytical instruments, Microsoft office whole suite

Professional experience

Doctoral Researcher in Synthetic Nanomaterials and Analytical Chemistry

August 2017-present

University of Mississippi Oxford, MS.

- Designed and executed multiple projects on atomic precise thiolate protected gold nanoclusters along with platinum and palladium nanoclusters.
- Mastered in analytical techniques and its data analytics through day-to-day usage.

- Experienced in different chromatographic skills like Size Exclusion Chromatography (SEC), TLC, GC and HPLC.
- Developed a good team management and communication skill through collaborating with interdisciplinary professors and their students.
- Mentored 2 high school students and 4 undergraduate students in nanoclusters synthetic methods and characterization using various analytical instruments.

High Resolution Mass Spectrometry Analyst August 2018-July 2019 & August 2020-present

University of Mississippi Oxford, MS.

- Developing and validating methods on ESI-MS & MALDI-MS to attain publication quality data on international and ACS standards.
- Analyzed a wide range of molecules including small organic molecules, inorganic complexes, molecules for medicinal chemistry, natural products, polymers, and biomolecules including peptides and proteins.
- Characterized about 60 samples a month (*Waters Synapt XS*) having published in various peer reviewed journals.
- Rectified and repaired MALDI-MS (*Voyager DE & DE pro*) instrument by myself through phone support by identifying the fault and changing the parts which saved thousands of dollars for service visits.
- Trained undergraduate students and graduate students from various research groups to use the MALDI-MS.

Analytical Chemist Intern December 2021-January 2022

Unique Farmaceuticals Las Vegas, NV.

- Extracting kratom from the powdered plant leaves using ethanol extraction method.
- Analyzing the different alkaloids using HPLC and its concentration in the extracted product.
- HPLC method development using available standards.

Teaching Assistant: Quantitative Analysis & General Chemistry August 2017-July 2018 & August 2019- July 2020

University of Mississippi Oxford, MS.

- Taught about 48 students per semester and conducted the lab in accordance with the curriculum.
- Instructed the experimental chemistry through instructions and hands-on training.

Corrosion Engineer Specialized in Cathodic Protection (CP) May 2014 – April 2017

Abdulla Fouad Impalloy Co. Ltd., Dammam, Saudi Arabia and Corrtech international Pvt Ltd., Ahmedabad, India.

- Monitoring, maintenance & troubleshooting of all CP system including transformer rectifier units, solar panels, and soil corrosion probe for underground pipeline in area IV covering about 200 KM of east west pipelines having 800 KM of underground pipeline systems.

- Reviewing, evaluating, and approving the design, installation, and commissioning for CP upgradation project along with indirect inspection reports (CIPS/DCVG/ACVG).
- Site installation, monitoring, design modification based on site condition and commissioning of CP systems including both sacrificial anode & impressed current CP systems for U/G piping (190 Km), tank external bottom (106 Nos), and U/G buried vessel (48Nos) in J3 Project, Jamnagar Refinery, India.

Certification

- NACE certified cathodic protection technician (CP Level – II)
- Rigaku school for practical crystallography and advance topics

Professional trainings

- Health, safety and first aid training approved by Saudi Aramco.
- Chemical safety and radiation safety training for devices, University of Mississippi.

Publications

- **Eswaramoorthy, S. K.**; Sakthivel, N. A.; Dass, A., Core Size Conversion of $Au_{329}(SCH_2CH_2Ph)_{84}$ to $Au_{279}(SPh\text{-}tBu)_{84}$ Nanomolecules. *J. Phys. Chem. C* **2019**.
- Sakthivel, N. A.; Jupally, V. R.; **Eswaramoorthy, S. K**.; Wijesinghe, K. H.; Nimmala, P. R.; Kumara, C.; Rambukwella, M.; Jones, T.; Dass, A., Size Exclusion Chromatography: An Indispensable Tool for the Isolation of Monodisperse Gold Nanomolecules. Anal. Chem. **2021**.
- **Eswaramoorthy, S. K.;** Dass, A., Atomically Precise Palladium Nanoclusters with 21 and 38 Pd Atoms Protected by Phenylethanethiol. *J. Phys. Chem. C* **2021**.

- **<u>Eswaramoorthy, S. K.;</u>** Dass, A., Digestive ripening yields atomically precise Au nanomolecules. *New J. Chem.* **2021**.

Presentations.

- Presented a poster on "*Core-size conversion of plasmonic gold nanomolecules."* in 257th ACS National Meeting, Orlando, FL (March 2019).
- Presented a talk on "*Size Exclusion Chromatography."* in 2021 Southeastern Regional Meeting, Birmingham, AL (November 2021).
- Presented a paper in International Symposium on Advances in Electrochemical Science & Technology (iSAEST-10), Chennai, India (January 2013) on topic *"$LiNi_xCo_{1-x}VO_4$ (x=0.0, 0.2, 0.4, 0.5, 0.6, 0.8, 1.0) cathodes for lithium-ion batteries."*